

ABSTRACT

Title of Dissertation: THERMOPLASTIC MICROFLUIDIC PCR
TECHNOLOGIES FOR NEAR-PATIENT
DIAGNOSTICS

Alex John Sposito, Ph.D., 2017

Dissertation directed by: Professor Don L. DeVoe
Department of Mechanical Engineering

Microfluidic technologies have great potential to help create portable, scalable, and cost-effective devices for rapid polymerase chain reaction (PCR) diagnostics in near patient settings. Unfortunately, current PCR diagnostics have not reached ubiquitous use in such settings because of instrumentation requirements, operational complexity, and high cost. This dissertation demonstrates a novel platform that can provide reduced assay time, simple workflow, scalability, and integration in order to better meet these challenges.

First, a disposable microfluidic chip with integrated Au thin film heating and sensing elements is described herein. The system employs capillary pumping for automated loading of sample into the reaction chamber, combined with an integrated hydrophilic valve for precise self-metering of sample volumes into the device. With extensive multiphysics modeling and empirical testing we were able to optimize the

system and achieve cycle times of 14 seconds and completed 35 PCR cycles plus HRMA in a total of 15 minutes, for successful identification of a mutation in the G6PC gene indicative of von Gierke's disease.

Next, a scalable sample digitization method that exploits the controlled pinning of fluid at geometric discontinuities within an array of staggered microfluidic traps is described. A simple geometric model is developed to predict the impact of device geometry on sample filling and discretization, and validated experimentally using fabricated cyclic olefin polymer devices. Finally, a 768-element staggered trap array is demonstrated, with highly reliable passive loading and discretization achieved within 5 min.

Finally, a technique for reagent integration by pin spotting affords simplified workflow, and the ability to perform multiplexed PCR. Reagent printing formulations were optimized for stability and volume consistency during spotting. Paraffin wax was demonstrated as a protective layer to prevent rehydration and reagent cross contamination during sample loading. Deposition was accomplished by a custom pin spotting tool. A staggered trap array device with integrated reagents successfully amplified and validated a 2-plex assay, showing the potential of the platform for a multiplexed antibiotic resistance screening panel.

THERMOPLASTIC MICROFLUIDIC PCR TECHNOLOGIES FOR NEAR-
PATIENT DIAGNOSTICS

by

Alex John Sposito

Dissertation submitted to the Faculty of the Graduate School of the
University of Maryland, College Park, in partial fulfillment
of the requirements for the degree of
Doctor of Philosophy
2017

Advisory Committee:

Professor Don L. DeVoe, University of Maryland, College Park, Chair
Professor Sarah Bergbreiter, University of Maryland, College Park
Professor Ben Shapiro, University of Maryland, College Park
Professor Miao Yu, University of Maryland, College Park
Professor Ian M. White, University of Maryland, College Park (Dean's
Representative)

© Copyright by
Alex John Sposito
2017

Dedication

To my late grandfather and NASA engineer John Thomas Sposito. Grandpa, I would not have been an engineer if it weren't for your inspiring and fascinating stories about slide rules and designing spacecraft for the moon. I know you would be so proud to see what I have accomplished.

Acknowledgements

First, I would like to thank my loving wife Erin for her unwavering support throughout this journey. It was not easy to make the sacrifices we made so that I could indulge my intellectual curiosity, but you did so without disinclination, and I will always thank you for that.

I also want to thank my advisor Prof. Don DeVoe for his mentorship during my studies. Your hard work and infinite wisdom on everything engineering inspired me to accomplish more than I thought possible in my time here. You have always supported my decisions with enthusiasm, provided intelligent feedback, and most importantly gave me the opportunity to engage in fulfilling and impactful research that will serve as the foundation for my future endeavors.

I also want to thank my parents for their love and support. Mom and Dad, you shaped me into a hardworking and motivated young man with all the tools to succeed in college and beyond. You never forced me to do anything, and let me chart my own course in life, so you know better than anyone what this degree means to me. Max, thank you, for being a good brother and helping me maintain a good work life balance all along.

Thank you also to my committee members Ben Shapiro, Sarah Bergbreiter, Miao Yu, and Ian White for their guidance and input in this dissertation. I especially want to thank Ian White for his efforts on procuring funds from Canon Life Sciences every year to support this work. Speaking of Canon, thanks are due to Ivor Knight for providing the University of Maryland with project funding and believing in our research direction. Thank you Lori Mull for your endless knowledge on polymerase

chain reaction and all things molecular biology. And of course, Shulin Zeng for his coordination of the UMD-Canon collaboration and providing me all the resources I would need from our sponsor.

Finally, thanks are also due to the many amazing members of the Maryland MEMs and Microfluidics lab. Thank you Kunqiang Jiang you started all of this when you agreed to teach me what it means to do research back when I volunteered as an undergraduate student. Thank you Jikun Liu for taking notice in me while I was working in the lab and offering me my first post graduate appointment. Thank you Eric Kendell for offering great professional and personal advice when it was much needed. Thank you Michael Weideroder for managing the intermural soccer team that kept me fit and gave me something to look forward to every Tuesday evening for the last 3 years. Thanks to Renee Hood, Isaac Misri, Annie Liu, Imaly Nanayakkara, Supriya Padmanabhan, and Omid Rahmanian for being great lab mates and for all the help you provided over the years. And of course thank you to my good friends Mona Mirzaei, Prakruthi Hareesh, and Jung Yun Han you all were the best company to share last four years with!

Table of Contents

Dedication	ii
Acknowledgements	iii
Table of Contents	v
List of Tables	vii
List of Figures	viii
List of Abbreviations	xi
Chapter 1: Introduction	1
Chapter 2: Rapid PCR in Self-filling Thermoplastic Chip	21
2.1 Introduction	21
2.2 Materials and Methods	24
2.2.1 Fabrication of Microfluidic Device	24
2.2.2 Passive Capillary Valve Design	26
2.2.3 Numerical Model	27
2.2.4 PCR Assay and Operation	28
2.3 Results and Discussion	29
2.3.1 Device Fabrication and Calibration	29
2.3.2 Passive Sample Loading	32
2.3.3 Thermal Performance	34
2.3.4 Assay Validation	37
2.3.5 Device Cost and Power Consumption	40
2.4 Conclusion	41
Chapter 3: Hydrophilic Valve Trap Sample Discretization	42
3.1 Introduction	42
3.1.1 Hydrophilic Valve Trap	42
3.3.2 Manual Syringe Fluid Actuation	43
3.3.3 Thermopneumatic Pump Fluid Actuation	43
3.3.4 Capillary Pump Fluid Actuation	44
3.2 Materials and Methods	44
3.3 Results and Discussion	45
3.3.1 Manual Syringe Trap Device Operation	45
3.3.2 Thermopneumatic Pump Trap Device Operation	46
3.3.3 Manual Syringe Trap Device Operation	48
3.4 Conclusion	50
Chapter 4: Staggered Trap Arrays for Robust Microfluidic Sample Digitization	51
4.1 Introduction	51
4.2 Materials and Methods	55
4.2.1 Microfluidic Device Fabrication	55
4.2.2 Self-Loading and Digitization Operation	56
4.3 Results and Discussion	56
4.3.1 Trap Chip Design and Modeling	56
4.3.2 Single-Sided Trap Model	59
4.3.3 Double-Sided Trap Model	62
4.3.4 Staggered Trap Model	63

4.3.5 Model Validation	67
4.3.5 High Density Staggered Trap Array	70
4.4 Conclusion	71
Chapter 5: A self-loading microfluidic platform enabling multiplexed PCR with integrated reagents	73
5.1 Introduction	73
5.2 Materials and Methods	75
5.2.1 Pin Spotting	75
5.2.2 Chip Fabrication	76
5.2.3 Multiplexed Assay	77
5.2.4 Chip Operation	78
5.3 Results and Discussions	79
5.3.1 Chip Design and Fabrication	79
5.3.2 Pin Spotting	80
5.3.3 Pin Spotting Tool Optimization	83
5.3.4 Reagent Integration and Controlled Release	84
5.3.5 Loading Performance	85
5.3.6 Multiplex PCR	87
5.4 Conclusion	89
Chapter 6: Conclusion	91
6.1 Summary	91
6.2 Contributions to the Field	92
6.2.1 Rapid PCR in Low Conductivity Thermoplastics	92
6.2.2 Fabrication of High Quality Expansion Valves for Stop Flow with Low Surface Tension Fluids	93
6.2.3 Novel Staggered Trap Array for Robust Sample Discretization	94
6.2.4 Staggered Trap Array for Multiplexed PCR with Integrated Reagents	95
6.3 Future Work	96
Appendices	101
Appendix 1:	101
Appendix 2:	102
Appendix 3:	106
Appendix 4:	108
Appendix 5:	109
Appendix 6a:	114
Appendix 6b	116
Appendix 7:	119
Appendix 8:	121
Appendix 9	122
Appendix 10	125
Bibliography	126

List of Tables

Table 5.1: Summary of primer additive materials for reagent integration.....	80
Table 6.1: Summary of ASSURED criteria with target specifications for POC HIV diagnosis outlined by Wu et al. ¹ , and specifications reached by the platform presented in this work. Although, target specifications were specific to HIV diagnosis they are applicable to this platform at the system level.....	89

List of Figures

Figure 1.1: Diagram of the PCR reaction with explanations of each temperature step. Source: https://www.neb.com/applications/dna-amplification-and-pcr	3
Figure 2.1: (a) 3D Schematic of the microfluidic device. (b) Close up view of the heater and sensor intersection. (c) Schematic of the hydrophilic valve.....	24
Figure 2.2: (a) CNC mills channels in Aluminum mold. (b) Polyetherimide (PEI) mold is embossed with Al mold. (c) COP resin is molded onto PEI mold. (d) COP wafer is exposed to decalin solvent and bonding to COP thin film. (e) Negative liftoff resist is spun onto COP wafer and photolithographically patterned. (f) COP wafer is developed (g) Cr and Au is deposited on top of COP wafer. (h) Final COP with Cr/Au elements..	27
Figure 2.3: Image of the XChip device and system. (a) Image taken from the bottom of the device of the Au heating and sensing elements. (b) Image taken from the top of the XChip of the microfluidic features. (c) Image of the XChip benchtop system....	28
Figure 2.4: Plot of meniscus position (mm) versus time (s) for 3 different capillary loading and flow stop experiments. Images in the inset are not representative of actual data points but just shown for visual reference.....	30
Figure 2.5: Parametric evaluation of different device designs plotting total rise time for a complete PCR cycle. (a) The reaction chamber depth was kept constant at 200 μm while bottom thickness was varied from 50 - 400 μm . (b) The bottom thickness was kept constant at 50 μm while the reaction chamber depth was varied from 50 to 500 μm . (c) Temperature vs. cycle time plots for the system using both open-loop and closed-loop control. The time cycle for closed-loop control system is 18.5 seconds, while the time cycle for open-loop control system is 80 seconds.....	31
Figure 2.6: Plot of 14 second cycle time with thermocouple embedded into reaction chamber to verify sensor accuracy. From this data I applied a further calibration factor equation to our temperature conversion to compensate for thermal lag in the chamber versus sensor during denature and anneal steps.....	33
Figure 2.7: (a) Plot of PCR amplification curves at different concentrations and cycle times. (b) Plot of C_p versus concentration. C_p values for each test were calculated by taking the standard deviation (σ) of the background fluorescence during cycle's 3-15 for each data set. This σ was multiplied by a factor of 20 to determine a threshold value for each independent data set.....	34
Figure 2.8: The PCR product from three experiments were run under high sensitivity electrophoresis on an Agilent BioAnalyzer 2100. The correct G6PC product is 45 bp in length while the instrument measured XChip product to be 51, 52, and 51 bp for each respective chip sample.....	35

Figure 2.9: (a) Plot of melt curve data collected on chip after PCR amplification. Data is then fit with a spline to mitigate sensor noise that results in a non-smooth melt peak. (b) HRMA analysis is done by taking the negative derivative of the spline fit equation at each respective data point and plotting the curve. The maximum $-(d/dT)$ in fluorescence is identified as the amplicon melting temperature.....	36
Figure 3.1: (a) Close up view of the high- β capillary valve. (b) Overview diagram of the trap array.....	39
Figure 3.2: (a) 96-well array with a single filling channel and hydrophilic valves to control well volume during loading. (b) Well volumes across each row of the array (average 5.8 ± 0.5 nL).....	43
Figure 3.3: Thermopneumatic pump operation of a 96-trap array. Images are taken over 6 min to capture the progression of sample through the device.....	44
Figure 3.4: Images taken during capillary loading of 30 trap array showing each of the three phases of operation.....	46
Figure 4.1: Illustration of the self-discretization workflow for a staggered trap array device.....	54
Figure 4.2: Schematic diagrams showing the trap configurations for (a) single-sided, (b) double-sided, and (c) staggered trap arrays. (d) Summary of geometric parameters used for model development.....	56
Figure 4.3: (a) Geometry for a single-sided trap configuration. (b) Images of the loading process for single-sided trap array with an $FR = 1.3$ and $\theta_a = 90^\circ$. Modeled relationships between (c) FR and θ_a at constant $CR = 0.51$, and (d) FR and CR at constant $\theta_a = 90^\circ$	58
Figure 4.4: (a) Geometry for a double-sided trap configuration. (b) Images of the loading process for a double-sided trap array $FR = 1.3$ and $\theta_a = 90^\circ$. Modeled relationships between (c) FR and θ_a at constant $CR = 0.51$, and (d) FR and CR at constant $\theta_a = 90^\circ$	59
Figure 4.5: (a) Geometry for a staggered trap configuration. The p is different on each side of the main channel because on the staggered side the pinning offset will include a barrier wall. So the pinning offset in the staggered side $p^* = (w_t - p) + s$. (b) Images taken of the loading process for an experimental staggered SLD device with $w_t = 390$ μm , $w_c = 200$ μm , $\theta_a = 90^\circ$ and $POR = 0.55$. (c) FR dependence on θ_a . (d) FR dependence on CR for varying PRs	62
Figure 4.6: Loading % of the different trap configurations at different aspect ratios. Two data sets (light and dark) for each trap configuration represent a difference in heights between the main channel and the trap.....	63

Figure 4.7: (a) Single-sided, (b) Double-sided, (c) Staggered. The model trap aspect ratio threshold is denoted by a black dashed line with the area shaded in green representing the parametric combinations the model predicts will have a high loading percentage. Data points for each parametric combination are plotted and connected by a solid black line and its shadow is color coded for each respective parametric combination. The data points that lie beyond the model threshold are shaded with a darker color and correspondingly show a sharp drop-off in loading percentage while the more transparent shadow represents data that falls in the region of expected high loading percentage.....	65
Figure 4.8: (a) Image taken of high density array of 768 traps loaded with sample and backfilled with oil. (b) Histogram of volume distribution in loaded SLD device.....	67
Figure 5.1: Image of the self-loading and discretizing chip.....	76
Figure 5.0.1: Fabrication process for the SLD platform. Pin spotting and CNC milling can be done in parallel and each substrate is then bonded using alignment pins.....	77
Figure 5.3: Image sequence of PEG and fluorescein salt being rehydrated by sample self-loading in the SLD chip. Approximate dissolution time was calculated when the initial bright spot was dispersed and could no longer be distinguished in trap.....	78
Figure 5.4: (a) Image of a dried down PEG/primer spot. (b) Image of a PEG/primer spot covered by a paraffin wax capping layer. (c) Image of primer spots capped with paraffin in the device chip.....	80
Figure 5.5: Image sequence showing temperature controlled release of fluorescein salt mixed with primer and PEG printing solution. After loading sample solution the chip was heated up to 70 °C showing original fluorescent spots dispersing throughout the wells.....	83
Figure 5.6: (a) Experimental design of the two step multiplex assay that was tested on the platform. (b) Table of experimental results with pUC19 template and pBR322 template loaded chips.....	85

List of Abbreviations

PCR – polymerase chain reaction
CGE – capillary gel electrophoresis
HRMA – high resolution melt analysis
PID – proportional integral derivative
POC – point-of-care
DNA – deoxyribonucleic acid
dsDNA – double stranded deoxyribonucleic acid
hgDNA – human genomic deoxyribonucleic acid
bp – base pairs (in reference to DNA)
FRET – förster resonance energy transfer
IR – infrared light
LOC – lab-on-a-chip
HIV – human immunodeficiency virus
qPCR – real-time polymerase chain reaction
RT-PCR – reverse transcriptase polymerase chain reaction
LAMP – loop mediated isothermal polymerase chain reaction
RNA – ribonucleic acid
rRNA – ribosomal ribonucleic acid
cDNA – complementary DNA
mPCR – multiplex polymerase chain reaction (multiple targets single reaction)
MPCR – multiplexed polymerase chain reaction (multiple targets multiple reaction)
WHO – World Health Organization
ASSURED – affordable, sensitive, specific, user-friendly, rapid and robust, equipment-free, delivered
PDMS – polydimethylsiloxane
COP – cyclic olefin polymer
COC – cyclic olefin copolymer
PVDF – polyvinylidene fluoride
SLD – self-loading and digitizing
PEI – polyethylenimine
LED – light emitting diode
TCR – temperature coefficient of resistance
EWOD – electrowetting on dielectric
FR – filling ratio = (f/w_t)
CR – channel ratio = (w_c/w_t)
PR – pinning offset ratio = (p/w_t)

Chapter 1: Introduction

1.1 Background

1.1.1 Diagnostics Background

In the earliest days of medicine, healthcare was administered in a person's home by physician house visits.² As technology advanced throughout the 20th century healthcare transitioned to clinics and hospitals where it became cost effective to conduct medical diagnostics in centralized laboratories equipped with refrigeration, benchtop equipment, abundant electrical power, and trained personnel.³ However, this diagnostic model is now struggling to keep pace with today's advances in medicine and healthcare. For example, for some diseases such as breast cancer and tuberculosis early detection can significantly decrease patient mortality, and provide a better overall prognosis.^{4,5} Likewise, chronic diseases such as diabetes, HIV, and cancer all require regular physiological monitoring so that doctors have more insight into disease progression and therapy response.^{2,6} Furthermore, the recent rise of antibiotic resistant bacteria has given need for rapid and comprehensive characterization of the infectious agent so that effective therapy can be administered.^{7,8} As such, the centralized laboratory model is not suited to provide the rapid, convenient, and cost effective diagnostics that is required for today's modern day healthcare challenges.

Technological innovations spurred on by the success of the microelectronics industry coupled with microfluidic science have led to the development of diagnostic systems that are better suited to return healthcare to the

point-of-care (POC). POC diagnostics are intended to be simple and low cost systems that allow patients to be diagnosed in the physician's office, small clinic, or even the patient's own home. POC diagnostics can also expand access to medical diagnostics in developing countries that are battling health epidemics such as HIV, tuberculosis, and Ebola, where access to centralized healthcare infrastructure is limited or unavailable.

1.1.2 Microfluidics and Lab-on-a-Chip Technology

Microfluidics and lab-on-a-chip (LOC) technologies, first described by Manz et al. in 1990,⁹ is the multidisciplinary science and technology involved in the control and manipulation of fluids on the sub-millimeter length scale. The behavior of fluids at the microscale differ from macroscale due to scaling behaviors for physical properties such as surface tension, mass transfer, and fluidic dynamics, and microfluidics explores how these behaviors can be leveraged for new applications. Lab-on-a-chip technologies can utilize microfluidics to perform operations that have traditionally relied on larger bench-top diagnostic systems in centralized labs, and LOC technologies improve upon these conventional benchtop systems by reducing sample and reagent consumption, lowering cost per test, reducing sample-to-answer times, shrinking system footprint, simplifying system operation, and offering greater multiplexing.³ Despite these inherent advantages and significant attention from the research community, LOC devices are still struggling to adhere to POC setting design guidelines (discussed in Section 1.3), and have thus lagged in commercial development.¹⁰ The focus of this dissertation is the development of a family of LOC technologies for PCR-based nucleic acid

testing that are compatible with POC platform requirements, and the combination of these technologies into an integrated POC diagnostic platform.

1.1.3 Thermoplastic Microfluidics

Initially microfluidic devices were made using traditional microelectromechanical systems (MEMS) fabrication techniques on silicon or glass substrates.^{11,12} However, these materials have fallen out of favor because they are non-disposable, expensive and difficult to manufacture. Soft-lithography and the use of polydimethylsiloxane (PDMS) for microfluidics was first discovered by the Whiteside's group in 1998,¹³ and has been used in for the construction of microfluidic devices ever since. Yet, PDMS is permeable to gas, hydrophobic, and not economically viable for high throughput production. On the other hand, paper based devices that employ capillary driven flow across patterned channels are also a popular substrate due to the low cost and simple fabrication. However, paper based microfluidics suffer from poor detection sensitivity due to limited optical transparency, as well as low sample retention due to evaporation.¹⁴ Thermoplastics such as polymethylmethacrylate (PMMA), polycarbonate (PC), and cyclic olefin copolymers (COC) have also been used for microfluidic devices because they are inexpensive, robust, and scalable for industrial manufacturing by injection molding. COP in particular is an attractive substrate especially in PCR applications due to its low water absorption, biological inertness, and high optical transparency. Not to mention COP is compatible with a variety of high-throughput manufacturing process such as injection molding,¹⁵ embossing,¹⁶ and reel-to-reel lamination¹⁷. For these reasons COP was chosen as the substrate for the devices reported in this work.

1.1.4 Thermoplastic Bonding of Microfluidic Devices

Thermoplastics are highly attractive substrate materials for the development of low cost microfluidic systems. Along with low materials cost in comparison to silicon and glass, thermoplastic substrates are also relatively simple to bond for the construction of microfluidic devices. One major advantage of thermoplastic bonding is the flexibility in control over parameters such as bond strength, which can be important for certain applications. For example, microfluidic applications such as liquid chromatography chips operate at high back pressures requiring interfacial bond energies on par with the cohesive strength of the bulk substrate material.¹⁸ On the other hand, microfluidic burst valves benefit from having controllable and relatively weak bonding.¹⁹ Another consideration is that most bonding processes require solvation of the polymer matrix, or the application of high temperature and pressures, all of which can affect the final size and shape microfluidic features.²⁰ Thus, the selection of the appropriate bonding technique for a given material will depend on the geometric tolerance required to maintain functionality. There are three general approaches to thermoplastic bonding: adhesive, thermal, and solvent bonding.

Adhesive bonding is simply the adhesion of two substrates through the use of glue. The main challenges associated with adhesive bonding are ensuring that the adhesive layer does not clog the microchannel features when the two substrates are mated. Several techniques have been reported to address this challenge by applying adhesive through contact printing,²¹ or through an intentional interstitial gap between substrates that can be filled with a UV curable resin²². Laminate films

sandwiched between two substrates and sealed with a laminator is another common technique for adhesion bonding.^{23,24} Commercial laminators are inexpensive, compatible with many different materials, and can be adopted into high throughput roll-to-roll manufacturing,¹⁷ making laminate sealing well suited for mass production of thermoplastic microfluidics.

Thermal bonding involves heating two substrates to near their glass transition temperature while applying pressure. The high temperature generates sufficient flow in the polymer and pressure insures interdiffusion of the polymer chains between substrate surfaces, leading to a strong bond. While thermal bonding can produce bond strength close to the cohesive force of the materials, temperature induced deformation is a major challenge, especially for devices with sub-100 μm features. Temperature and pressure optimization during bonding though the use of a controllable hot presses instrument is one strategy to mitigate feature deformation.²⁵ Another successful strategy has been apply UV ozone surface treatment to the substrates to lower the bonding temperature required.²⁶

Solvent bonding involves solvating the bonding surface of the substrate by applying the solvent in liquid phase,²⁰ or vapor phase²⁷. Solvent causes the polymer chains to become mobile, and thus can readily diffuse between the two substrates, leading to extensive polymer chain entanglement across the interface, and a strong bond. The Hildebrandt parameter (δ) is used to determine the appropriate solvent for a particular polymer. While strong bonding occurs when the solvent δ and polymer δ are roughly equal,²⁸ equal Hildebrandt parameters can also cause feature deformation with excessive solvent uptake. As such, bonding parameters such as

solvent concentration, solvent phase, exposure time, and temperature, must be optimized for each system to achieve strong bond with minimal deformation. In addition, it has been reported that using a glass substrate to stamp a controlled dose of solvent can mitigate channel deformation.²⁹ Furthermore, the use of sacrificial materials such as wax,³⁰ or water,³¹ has also been explored as a highly robust solution for preventing channel collapse even after extended solvent exposure. Optimized solvent bonding protocols yield strong bonding, minimal channel deformation, and require low processing temperatures, which were all important factors in the construction of microfluidic devices for PCR. As such, an optimized protocol based off a process developed by Wallow et al.,²⁰ was used for bonding the devices described throughout this thesis.

1.2 Polymerase Chain Reaction

1.2.1 Benchtop PCR

Since its introduction in 1986,³² PCR has become an indispensable tool in many biomedical research laboratories for expression profiling of genes,^{33,34} genotyping,^{35,36} epigenetics,³⁷ forensic analysis,^{38,39} and clinical diagnostics of viral and bacterial pathogens.^{40,41} Using a DNA-polymerase enzyme, the PCR process involves controlled thermal cycling between three discrete temperatures to denature, anneal, and elongate specific nucleic acid sequences, resulting in exponential amplification of the targeted sequences (Figure 1.1). Currently, PCR is commonly run on benchtop systems that employ large resistive or thermoelectric heating elements for temperature control, resulting in high power requirements and

slow amplification times due to the large thermal masses involved.⁴² Additionally, such systems require a high degree of sample and reaction consumables to drive macroscale reaction volumes. Together with high costs associated with benchtop PCR platforms, these limitations have constrained the wider use of PCR in point-of-care settings.

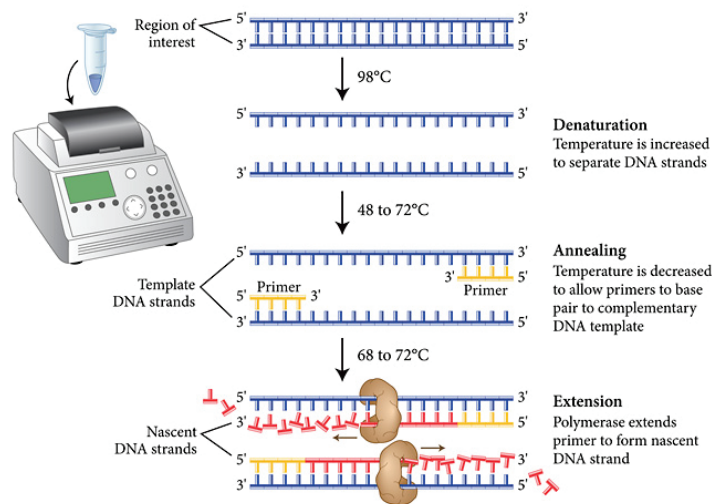


Figure 1.1: Diagram of the PCR reaction with explanations of each temperature step. Source: <https://www.neb.com/applications/dna-amplification-and-pcr>

1.2.2 Post-PCR Analysis

In order to validate amplification products (amplicons) so as not to draw the wrong conclusion from amplification signal (false positive in context of diagnostics), amplicon characterization is a practical necessity in PCR-based diagnostic platforms. Electrokinetic separation methods are commonly employed in laboratory testing because of their high-throughput, and separation efficiency. Capillary gel electrophoresis (CGE) is the gold standard in post-PCR analysis and its working principle involves the separation of nucleic acids by applying an electric field to move negatively charged molecules through a gel matrix. Shorter molecules

move faster through the gel pores and thus migrate farther. A DNA stain is added to reveal clusters of DNA based on their fragment size throughout the gel. While CGE is a robust characterization method, operational requirements including; gel forming, high power, slow migration times, and resolving power over a small dynamic range of base pair (bp) sizes make CGE adverse to the POC domain. Alternative methods for amplicon analysis like sequencing and mass spectrometry allow broader-scale product characterization, but are costly, impose significant infrastructure demands, and lacking in throughput.⁴³ Probe-based amplicon characterization is another common approach where a specific nucleotide sequence complementary to the intended target with a FRET reporter is introduced. If the correct product is present the probe will fully hybridize causing proximity dependent transfer of energy resulting in a fluorescent signal. If a different product from the intended target is present the transfer of energy will not occur and no signal is produced. One limitation of probe-based validation is that only a finite number of targets can be characterized at the same time, prohibiting its use in multiplexed devices. High resolution melt analysis (HRMA), a subset of probe-based characterization, instead uses a common probe that will intercalate within dsDNA products created during amplification. The amplicon is subsequently heated and when melted it denatures and the intercalating probe is released quenching its proximity-dependent fluorescence. HRMA offers several advantages in the context of POC diagnostics including, simplicity, integration, and ability to distinguish single nucleotide polymorphisms, all critical requirements in POC PCR-based diagnostics.

1.2.3 Evolution of PCR for Diagnostics

Since its introduction PCR has undergone some important evolutions to improve utility and versatility for the next generation of diagnostics. Real-time quantitative PCR (qPCR) is the combination of amplification with detection using intercalating dyes, allowing for continuous monitoring of fluorescence signal during amplification and quantitative evaluation of the initial nucleic acid concentration. The basic concept of qPCR is that these intercalating dyes will only fluoresce when hybridized within a dsDNA segment. Fluorescent intensity readings are taken at the same temperature (usually 72 °C) for each cycle when only dsDNA representing your target is intact and smaller non-specific products are denatured. Over the course of the reaction dsDNA products are increasing exponentially leading to a commensurate increase in fluorescent intensity. Tracking the number of cycles it takes for fluorescence to reach a certain threshold provides insight on PCR efficiency, and can be used to determine the initial concentration of pathogen using a standards curve. As compared with conventional PCR, qPCR offers reduced sample-to-answer time, and mitigates risk of DNA contamination by eliminating the post-PCR validation step. As such, qPCR has been demonstrated as an effective technique for bacterial strain identification and antibiotic resistance screening in a number of diagnostics applications.⁴⁴ The utility offered by real-time detection and quantification plus compatibility with HRMA made it a focus of the platform described within this work.

Another evolution has been to develop nucleic acid amplification techniques that do not require thermocycling (isothermal), shedding supporting

equipment and reducing system complexity. Isothermal amplification typically exploits strand-displacement activity of the DNA polymerase enzyme to cyclically amplify a target at constant temperature and decrease overall assay time. There are several isothermal amplification schemes, but one of the more common techniques is loop-mediated isothermal amplification (LAMP). Loop-mediated isothermal amplification (LAMP) uses 4-6 primers recognizing 6-8 distinct regions of target DNA. A DNA polymerase with strand displacement activity initiates synthesis and the primers form loop structures to facilitate subsequent rounds of amplification. The addition of two “loop primers” that anneal to the amplicon loop structure was shown to accelerate the reaction rate and improve specificity.⁴⁵ The LAMP technique has been applied to detection of various pathogens including viruses^{46–48} and bacteria^{49,50} in microfluidic diagnostics. Besides eliminating the need for thermocycling hardware, another advantage of LAMP is that the reaction can be monitored without sophisticated optical hardware. In fact, the byproduct of the amplification reaction, magnesium pyrophosphate, is so prolific that it can be observed by eye in real-time,⁵¹ making LAMP well-suited for field diagnostics. However, one of the main drawbacks of LAMP compared to conventional PCR is inhibition in the presence of clinical samples,⁵² as well as the inability to validate reaction products in vitro⁵³. Furthermore, primer design constraints also complicate the routine application of LAMP for clinical diagnostic applications.

A further advantage of PCR is the ability to target both DNA and RNA from clinical samples. RNA based targets are prevalent in both viruses and bacteria.⁵⁴ For example, ribosomal RNA (rRNA) is a universal constituent of bacterial

ribosomes and is present in high copy numbers,⁵⁵ while genomic RNA is the appropriate target for Hepatitis C. To analyze RNA using PCR, the RNA template is first converted into a complementary DNA (cDNA) using the reverse transcriptase enzyme. The cDNA is then used as a template for amplification. This process is called reverse transcriptase-PCR (RT-PCR). RT-PCR also has the advantage of being able to discriminate between dead and viable cells since mRNA does not persist long in dead cells, while DNA persists in both indefinitely.⁵⁵ RT-PCR is an essential tool for the diagnosis of RNA based pathogens and its discovery represented an important shift in combating several global healthcare crises such as, influenza and HIV. While RT-PCR is not explicitly explored in this work, the technologies described here are fully compatible with this approach to RNA analysis.

PCR as a diagnostic tool is expensive in terms of consumables, and can take up to 2 hours for results. Furthermore, multi-target tests are especially needed for identification of the particular infectious agent causing a clinical symptom that may have multiple causative agents. Failure to do so in a timely manner could have serious implications on patient prognosis.⁵⁶ A new PCR-based method to increase the diagnostic output per test, lower cost, and provide important clinical information was needed. First described in 1988 by Chamerlain et al.,⁵⁷ multiplex PCR (mPCR) is the simultaneous amplification of multiple targets in one reaction. The conventional method for performing multiplex PCR (mPCR) is to load multiple primers for the amplification of multiple target templates in one reaction. However, complexity of primer design and validation for mPCR remains a

significant limitation for new assay development. More fundamentally, primer competition and spectral overlap of fluorescent probes used in real-time PCR (qPCR) limits the number of multiplexing, with 5-plex assays representing the nominal maximum that may be detected in a single reaction.⁵⁸ To overcome these constraints, multiplexing may be achieved by performing multiple individual PCR reactions simultaneously in spatially-isolated reaction wells. While a number of commercially available benchtop platforms supporting well plate based mPCR have been developed,^{59–61} they are burdened by automation equipment, costly consumables, and slow assay times, prohibiting their use in point of care settings.

An alternative to mPCR is to perform multiple single-target PCR reactions in parallel to achieve spatial multiplexing. Several microfluidic technologies have been explored that have the potential to advance multiplexed PCR reactions through the automation of sample segregation. For instance, droplet microfluidics has been used to generate huge arrays of individual droplet PCR reactors isolated by an immiscible phase.^{62–65} Furthermore, recent demonstrations in automated combination of sample with different reagents through droplet merging functions,^{66–68} validates its application to multiplexed PCR. Yet, this approach is still fundamentally tied to flow control hardware that is needed to form and manipulate droplets, and therefore does not serve to reduce the complexity and instrumentation requirements found in existing benchtop systems. On the other hand, passive means of segregating individually addressable reaction volumes by discontinuous dewetting,^{69,70} or geometry induced fluid shearing,^{71–73} simplifies automation and reduces equipment burdens. Passive approaches are particularly

suited for multiplexed PCR as reaction volumes are spatially defined allowing for simple recombination with spatially defined reagents. Ideally, the process of segregating sample volumes and recombining with different integrated reagents should be equipment free so as to reduce platform footprint and cost.

1.3 Point-of-Care ASSURED Criteria and Current Limitations

1.3.1 POC Diagnostics Criteria

The World Health Organization (WHO) has developed a criteria for judging POC diagnostic tests: the “ASSURED” criteria, as Affordable, Sensitive, Specific, User-friendly, Rapid and Robust, Equipment-free, Delivered. Developing a POC system that scores highly along the lines of the ASSURED criteria will serve as a proof of concept for a new paradigm in diagnostic systems and healthcare. The use of PCR for diagnostics in near-patient or point-of-care settings demands technology compatible with the World Health Organization’s guidelines for the ideal POC test: “ASSURED” - Affordable, Sensitive, Specific, User-friendly, Rapid and Robust, Equipment-free, Delivered.⁷⁴

1.3.2 Affordability Challenges

The affordability metric in the ASSURED criteria continues to pose a challenge for microfluidic PCR development. To have successful PCR on-chip it is imperative to have robust thermal control so that the three temperature steps of the reaction (denature, anneal, extension) are met accurately. Moreover, with the inclusion of HRMA, temperature precision is paramount in identifying single nucleotide polymorphisms where melt temperature deviations can be as small as

0.1 °C between normal genes and mutations. Consequently, many microfluidic PCR devices employ silicon or glass substrates for their desirable thermal properties. This is especially true for systems that intend to achieve ultrafast PCR.⁷⁵ Yet, both glass and silicon are very expensive from a raw material and manufacturing standpoint compared to alternative materials, and consequently are designed to be reused. In a POC setting, it is difficult to see the utility of expensive and non-disposable devices for ubiquitous diagnostic testing even considering their high thermal performance. In contrast to these materials, thermoplastics offer significant advantages for the development of low-cost consumable microsystems.⁷⁶ For example, thermoplastics may be patterned using exceptionally low-cost replication techniques,¹⁵ and a variety of rapid large-area bonding methods^{18,77} are available for sealing the resulting microchannels. While a number of thermoplastic PCR chips have been reported,^{78–83} the high heat capacity and low thermal conductivity associated with engineering thermoplastics have resulted in thermal response times that prohibit rapid PCR. Several techniques based on non-contact heating have been explored to address the thermal limitations of thermoplastics, enabling their effective use as microfluidic substrates for rapid nucleic acid amplification. For example, Muddu et al. reported 10 min PCR in a thermoplastic substrate using microscale convection to control the local surface temperature.⁸⁴ Similarly, Son et al. employed non-contact plasmonic photothermal heating of a gold thin film to thermocycle poly-methyl methacrylate microwells, with amplification achieved in 5 min.⁸⁵

1.3.3 User-Friendly Challenges

The ideal POC system would allow a minimally trained operator to run the test without intervention or oversight, making the system user-friendly. However, even today many microfluidic systems fail to consider the importance of usability and automation, requiring trained lab technicians, expensive supporting instruments to function. For example, flow through PCR systems, whereby the sample is moved through different regions of the device that are individually preheated to PCR specific temperatures, have been reported for enhancing reaction speed in POC PCR devices.^{86,87} Here, reaction time is only limited by the flow rate and heat transfer between the sample and sidewall. The major disadvantage of flow through systems is the requirement of flow control apparatus and complex chip interfacing, which in most cases require trained technicians to operate. In the same way, droplet microfluidics can drastically decrease the thermal inertia of PCR cycling, while enabling high throughput amplification, and enhanced sensitivity.^{88,89} Nonetheless, these features again come at the cost of usability - requiring complex pumping/interfacing equipment and chip initialization procedures not suited for point-of-care use. On the other hand, stationary reaction chamber design affords simplicity as sample introduction is usually done statically via capillary action,⁸³ pneumatics,⁹⁰ or centrifugal force.⁹¹ While throughput and rapid PCR are challenges in stationary reaction chamber design, addressing these challenges is not insurmountable and will be covered extensively in the following chapters of this proposal.

1.3.4 Rapid Results Challenges

Successful implementation of POC diagnostics call for systems that can provide patient results in < 30 minutes.⁵⁶ Ultrafast microfluidic PCR has proven capable of achieving analysis times on the order of minutes,⁸⁷ yet few have accomplished it conforming to ASSURED criteria. In one example, Neuzil and co. patterned heaters and thermistors on a PCR device to achieve sample analysis in 35 min, and at the same time reduced the supporting system hardware to a handheld format.⁹² Although, the system consumes one glass chip per test which is not economical for preventative screening assays, or disease progression monitoring. Giordano et al. demonstrated a cycle time of less than 4 minutes by using non-contact IR mediated heating of a polycarbonate microdevice.⁹³ Jung et al. developed a rotary system for rapid PCR that consumed a disposable polymer device and achieved PCR amplification in 25 minutes.⁹⁴ In both these examples, on-chip temperature control is not achieved so off-chip verification equipment for CGE are required following amplification, nullifying time saved during PCR. Attaining rapid PCR without sacrificing affordability while reducing supporting hardware requirements necessitates high performance heater/sensor integration on a low cost platform, which so far has been explored on a limited basis in prior art apart from the work presented herein.

1.3.5 Equipment-Free Challenges

For diagnostics to move from centralized lab facilities to the point-of-care, systems must not require peripheral instrumentation to operate. ASSURED criteria considers this in its equipment free metric. The microscale integration afforded

by microfluidics offers POC systems the ability to provide the functionality without add-on equipment. For instance, capillary action, as a fluid actuation mechanism, is by far the most simple and equipment free technique and accordingly is core to some of the most successful diagnostics tests to date - glucose monitoring,⁹⁵ and pregnancy tests.⁹⁶ While thermal integration^{75,11,12,97,98} has been studied extensively throughout literature, demonstrations of fluid actuation integration for PCR applications is limited. In one example, Zhu et. al. showed a capillary flow driven PCR system for digitized loop-mediated amplification (LAMP) which primes the chip with a combination of capillary action and vacuum.⁹⁹ This systems however requires vacuum pretreated PDMS substrates with limited shelf-life and poor manufacturability. The TaqMan Array card (Life Technologies Corporation, Foster City, CA, USA) is another example of capillary driven microfluidic PCR but suffers from the requirement that centrifugal force is still required to complete priming of reaction chambers.⁶⁰ An effective capillary flow driven device for PCR should incorporate sample transport and metering into single or multiple reaction chambers for high-throughput PCR analysis without peripheral equipment or unnecessary workflow.

1.4 Dissertation Approach and Organization

The goal of the research presented in this dissertation is to demonstrate a point-of-care diagnostic platform with the following capabilities:

- Composed of disposable and low cost materials
- Rapid and automated PCR operation/analysis

- Integrated functional components (i.e heaters, reagents, flow control)
- Simple instrument free operation
- Multiplexed capability

This work will provide new knowledge to the field in the performance of thermoplastic materials for rapid and accurate PCR and HRMA. Several techniques for sample discretization will be explored that are all compatible with PCR based diagnostics. This work will present a novel and simple discretization technique along with an analytical model that will establish important geometric relationships, and provide a predictive tool for performance across a wide design space. This discretization technique should be applicable across a broad spectrum of microfluidic applications. Furthermore, this work will present a new technique for reagent deposition along with methodologies for reagent protection during operation so as to enable unmatched simplicity in diagnostic workflow and highly scalable multiplexed PCR. All investigated technologies will utilize practical fabrication methods that are scalable for high-throughput manufacturing, drastically reduce system level instrument requirements, and operate with off-the-shelf low cost electronics and optics. Collectively, the advances reported herein will provide a complete platform capable of rapid multiplexed PCR and HRMA in a low cost and disposable format that is simple and user-friendly.

This dissertation is organized into six chapters to summarize the work completed. Chapter 2 is titled “Rapid PCR in Self-filling Thermoplastic Chip” and consists of the work that was published in *Lab on a Chip*.¹⁰⁰ In this chapter, a self-filling thermoplastic device with integrated heater and sensor electrodes capable of

ultrafast (sub-10 minute amplification) PCR is demonstrated. In contrast to more thermally conductive glass and silicon substrates commonly used for ultrafast PCR, this study shows that lower cost and easier to manufacture thermoplastics can achieve similar performance in terms of total assay time and HRMA resolution. This platform will serve as the foundation and establish practical constraints for the multiplexing and reagent integration technologies presented in the Chapters 3, 4, and 5.

Chapter 3 is titled “Hydrophilic Valve Trap Sample Discretization” and covers unpublished work on strategies for simple, robust and equipment-free sample discretization. The concept takes the hydrophilic valve developed in Chapter 2 and utilizes them as an automated mechanism for the segregating of sample into many aliquots. Three fluid actuation mechanisms were explored for sample loading; manual syringe, thermopneumatic pumping, and capillary flow. Each of these fluid actuation mechanisms would require minimal supporting equipment and user intervention. Important insights on loading reliability and system design were gained leading to the development of a simpler and more effective sample discretization trap described in the next chapter.

Chapter 4 is titled “Staggered Trap Arrays for Robust Microfluidic Sample Discretization” and consists of work that has been submitted for publication to *Lab on a Chip*. This work describes a passive sample digitization method that exploits the controlled pinning of fluid at geometric discontinuities within an array of staggered microfluidic traps. The staggered trap design enables reliable sample filling within high aspect ratio microwells using a completely novel design. A

simple geometric model is developed to predict the impact of device geometry on sample filling and discretization, and validated experimentally. In addition, a 768-element staggered trap array is demonstrated, with highly reliable loading and discretization achieved within 5 min. The resulting discretization platform offers simplified workflow and equipment free operation using a low-cost thermoplastic substrates.

Finally, Chapter 5 is titled “A self-loading microfluidic platform enabling multiplexed PCR with integrated reagents” and contains work that will be submitted to *Lab on a Chip*. This work expands upon on the platform described in the previous chapter by adding integrated reagents and demonstrating multiplexed PCR. Reagents are integrated by spotting sequence-specific PCR primers in a paraffin wax matrix preventing reagent dispersion during sample loading. An array of 16 traps with integrated reagents was loaded via capillary action in under 1 minute, and a 2-plex PCR assay was conducted on the platform to demonstrate its utility for PCR applications. The staggered trap array platform proved the capability of multiplexed PCR in a reliable, equipment-free, and low cost format.

Chapter 2: Rapid PCR in Self-filling Thermoplastic Chip

2.1 Introduction

Since its introduction in 1986,³² PCR has become an indispensable tool for diverse applications in molecular biology, biomedicine, pathogen detection, forensics, and beyond. Using a DNA-polymerase enzyme, the PCR process involves controlled thermal cycling between three discrete temperatures to denature, anneal, and elongate specific nucleic acid sequences, resulting in exponential amplification of the targeted sequences. Benchtop PCR systems commonly employ large resistive or thermoelectric heating elements for temperature control, resulting in high power requirements and long amplification times due to the large thermal masses involved.⁴² Together with high costs associated with benchtop PCR platforms, these limitations have constrained the wider use of PCR in point-of-care settings. For use as a near-patient diagnostic tool the ideal PCR system should support rapid sample-answer times using individual clinical samples, while offering simple operation in a small footprint. The system should also employ inexpensive and disposable PCR elements to minimize cost and infrastructure requirements, issues of particular concern for applications in global healthcare and resource-limited environments.

Microfluidic technology offers significant potential for overcoming these constraints and advancing PCR technology for point-of-care applications.^{42,101–103} The earliest PCR microsystems consisted of bulk-etched silicon reaction chambers with integrated thin film polysilicon heaters,^{11,12} where inherently low thermal mass

and high surface area in these systems enabled rapid cycle times around 2 min. A range of microfluidic PCR systems have since been reported that employ integrated thin film heaters patterned on silicon or glass substrates containing sealed microchannels within which amplification occurs.^{75,97,98,104–110} While these microscale platforms have been shown to enable PCR cycle times as low as 4.5 s,⁸⁷ the fabrication costs associated with bulk micromachining and sealing of both silicon and glass substrates can be prohibitive for many applications. In contrast to these materials, thermoplastics offer significant advantages for the development of low-cost consumable microsystems.⁷⁶ In particular, thermoplastics may be patterned using exceptionally low-cost replication techniques,¹⁵ and a variety of rapid large-area bonding methods^{18,77} are available for sealing the resulting microchannels. While a number of thermoplastic PCR chips have been reported,^{78–83} the high heat capacity and low thermal conductivity associated with engineering thermoplastics have resulted in thermal response times that prohibit rapid PCR. Several techniques based on non-contact heating have been explored to address the thermal limitations of thermoplastics, enabling their effective use as microfluidic substrates for rapid nucleic acid amplification. For example, Muddu et al. reported 10 min PCR in a thermoplastic substrate using microscale convection to control the local surface temperature.⁸⁴ Giordano et al. demonstrated a cycle time of less than 4 min by using non-contact infrared heating of a polyimide microdevice.⁹³ Similarly, Son et al. employed non-contact plasmonic photothermal heating of a gold thin film to thermocycle poly-methyl methacrylate microwells, with amplification achieved in 5 min.⁸⁵ While relatively rapid PCR cycle times were

achieved in each of these examples, non-contact heating imposes additional constraints on temperature control and thus generally lack functionality for on-chip HRMA.

In this chapter, we report a disposable thermoplastic microfluidic device that enables rapid PCR together with HRMA of the resulting PCR product in a single integrated platform. In addition to performing rapid PCR and HRMA in a low-cost format, the thermoplastic chips are designed to address several system-level issues which constrain established microfluidic PCR platforms. The devices are fabricated using a two-step embossing process compatible with high throughput replication-based manufacturing processes, with cyclic olefin polymer (COP) used as a thermoplastic with low autofluorescence. Significantly, sealing of the COP microchannels is performed using a 50 μm thick COP film layer, thereby minimizing thermal resistance and mass of the PCR chips. Thermal control is achieved by patterning thin film metal electrodes directly onto the sealing layer for combined temperature sensing and thermal actuation in a low-power format. Simple operation is provided through self-loading of reaction volumes using an integrated passive capillary valve, requiring minimum operator intervention and eliminating the need for fluidic interfacing, pumping, or metering during chip loading. To operate the microfluidic device, a fully self-contained system was developed using a microcontroller to implement all assay steps including thermocycling using a closed-loop proportional-integral-derivative (PID) control scheme and fluorescence detection for assay readout. Thermal performance of the device was optimized through parametric multiphysics modeling, enabling a

thermal cycle time of 14 s. Validation of the microfluidic system is performed through an assay for detecting a single mutation in the human G6PC gene associated with type I glycogen storage disease (von Gierke's disease), a metabolic disorder resulting in the accumulation of glycogen and fat in body tissues and low blood glucose levels. The resulting disposable PCR device successfully combines simple operation, rapid PCR, precise temperature control for accurate HRMA, and low cost in a compact format.

2.2 Materials and Methods

2.2.1 Fabrication of Microfluidic Device

A master mold was prepared from 15 cm square plate of 6061 aluminum. The aluminum was planarized using a chemical-mechanical polishing tool (METPREP 4, Allied High Tech Products Inc., Rancho Dominguez, CA) with 1500 diamond grit sandpaper at 2 psi for 10 min followed by the PLAN-B polishing cloth and 6 μm colloidal silica slurry on for an additional 2 psi for 10 min. Final polishing was performing using Final P polishing cloth with 1 μm colloidal silica slurry at 2 psi for 10 min to achieve a mirror finish. After polishing features were milled into the Aluminum mold using a computer numerical controlled 3-axis CNC machine (MDX-650, Roland DGA, Irvine, CA). Inverse features from the aluminum mold were transferred to a secondary mold consisting of polyetherimide (Ultem PEI 1000) by embossing at 230 °C and 250 psi for 30 min using a hot press (AutoFour/15, Carver, Inc., Wabash, IN).

The microfluidic substrate was constructed of COP (Zeonex 1420R, Zeon Chemicals, Louisville, KY). Approximately 15 mL of resin pellets were placed on the PEI secondary mold and heated to 190 °C for 30 min in the hot press. Once heated, the pressure applied to the stack was increased in 50 psi increments every 10 min, and held at a final pressure of 250 psi for an additional 10 min. The resulting COP plaque had a thickness of approximately 550 μm . The imprinted reaction chamber was 200 μm deep, while hydrophilic expansion valve regions were 30 μm deep. Input ports were manually drilled using a drill press. The microfluidic substrate was sealed by a 50 μm thick COP film (Zeonex 1420R, obtained as samples from Zeon Chemicals) using a solvent bonding technique modified from a previously developed procedure.²⁰ The channel side was exposed to 35% decahydronaphthalene in ethanol (w/w) for 7 min, rinsed with 100% ethanol, and blown dry with N₂. The multilayer substrate was then pressed at 200 psi and 50 °C for 10 min in a hot press to complete the bonding. Thin film gold electrodes for temperature control were fabricated using a liftoff resist process. Negative liftoff photoresist (NR9-3000PY, Futurrex Inc., Franklin, NJ) was spun to a thickness of 3.7 μm on the exposed surface of the 50 μm COP layer and patterned by contact photolithography. Alignment marks pre-molded into the COP microchannel layer were used to position the mask to precisely align the electrodes under the reaction chamber (Figure 2.1a). After developing the photoresist (RD6 developer, Futurrex Inc., Franklin, NJ), a 15 nm chromium adhesion layer and 75 nm gold layer were sequentially deposited by e-beam evaporation (Denton Vacuum Explorer, Moorestown, NJ), and photoresist was removed by immersing the wafer in an

acetone bath under light agitation. The metallized COP wafer was cleaned with methanol, isopropanol, and deionized water, and individual chips (six to a wafer) were separated by CNC milling.

2.2.2 Passive Capillary Valve Design

The intention to keep the system low cost and simple to use directed us towards a passive option for controlling sample flow. Passive stop flow valves fall into two categories; capillary valve,¹¹¹ and hydrophobic valve.¹¹² The basic idea is that a geometric change in the channel wall results in a change of its wetting properties. When the wetting force of the valve is less than the driving fluid force, the valve bursts. For capillary flow this geometric change must be an expansion as it needs the positive delta in Laplace pressure (enlarged meniscus at the neck) to counteract the capillary force acting on the sidewalls. For hydrophobic valves, the geometric change must be a narrowing of the channel.

In our particular case, the PCR solution has a relatively low surface tension with the COP, which will be made even lower due to increased temperature when thermocycling. These operational requirements necessitated careful design of the expansion valve to provide appropriately high burst pressure. Burst pressure was optimized through the principle radii of curvature, aspect ratio of the region preceding the expansion, and the β -angle parameter (diverging angle with respect to the neck of the straight channel). The pressure difference across the meniscus is governed by the Young-Laplace equation (Equation 1).

$$\Delta P = -2\sigma \cos \theta \left(\frac{1}{w} + \frac{1}{h} \right) \quad (1)$$

In this equation, w and h are the radii of curvature, θ is the contact angle in the channel, and σ is the surface tension. From this basic relationship it is clear that minimizing the radii of curvature will produce a larger pressure difference when θ and σ are fixed. Looking deeper, Thio et al. developed and validated a burst pressure model proving the smaller aspect ratios lead to higher burst pressures.¹¹³ With this in mind we sought to minimize the height, width, and the aspect ratio and we achieved dimensions of $w = 60 \mu\text{m}$, $h = 30 \mu\text{m}$, and aspect ratio of 0.5 (Figure

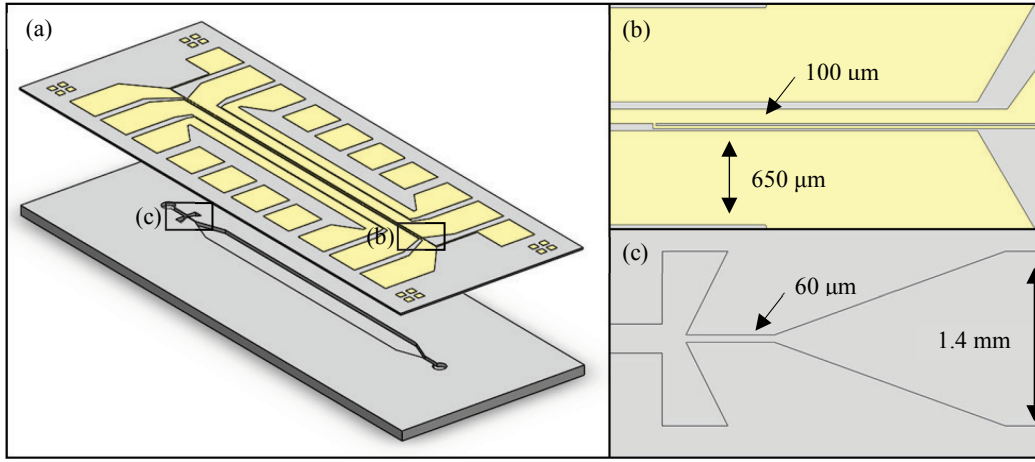


Figure 2.1: (a) 3D Schematic of the microfluidic device. (b) Close up view of the heater and sensor intersection. (c) Schematic of the hydrophilic valve

2.1c). The β -angle was also maximized to 120° based on the repeatability and quality of the valve after fabrication.

2.2.3 Numerical Model

A 3D COMSOL model (Version 4.5, COMSOL, Burlington, MA) incorporating PID control was developed to study thermal performance during each step of the PCR cycle. The PID algorithm used step-specific parameters to maximize speed and control authority at each step. The input voltage was clipped to a constant voltage of 2.5 V (100% duty cycle) in the model to mimic the experimental conditions. The modulation of that input voltage was determined

using feedback from a temperature sensor element built into the model. Dimensions of the bottom COP film thickness and reaction chamber depth were varied over ranges that were selected based on material and fabrication process constraints. Forced air convection was incorporated to represent high CFM fans blowing on the chip during operation, with convective heat flux parameters for the denature, anneal, and extension steps given by 40, 80, and 40 $\text{Wm}^{-2}\text{K}^{-1}$ respectively. Rise time, defined as the time the response to rise from 10% to 90% of the steady state value, was determined using the model at each thermocycle step for each geometric variation. The model was also used to compare cycle times under open-loop and closed-loop control. For closed-loop control, the input voltage was modulated using a PID control algorithm and temperature feedback from the sensor element. Proportional, integral, and derivative controller constants were varied to optimize cycling speed and control authority at each step. Total cycle times for both open loop and closed loop control included hold times at the denature, anneal, and extension steps of 2, 2, and 4 s respectively.

2.2.4 PCR Assay and Operation

A G6PC assay (G6PC c.79delC Novallele Genotyping Assay, Canon US Life Sciences, Rockville, MD), comprising forward and reverse primers together with commercial master mix including DNA-intercalating dye, was used to evaluate the microfluidic PCR platform. The assay was chosen for its clinical relevance in the diagnosis of von Gierke's disease.¹¹⁴ Samples of hgDNA (id# NA11254) were purchased from Coriell Institute for Medical Research (Camden, NJ). The G6PC primer set, mastermix, and hgDNA template were added in equal

volumes of 2 μL to make a stock solution. From that stock 3.25 μL was used as the reaction volume for each experiment. The hgDNA template concentration in the stock reaction solution was 20 ng/ μL which was diluted in Tris-EDTA to 4 and 2 ng/ μL concentrations, resulting in approximately 10^4 , 2×10^3 , and 10^3 copies respectively (152 copies/ng). LCGreen dye (Idaho Technology, Salt Lake City, UT) was included in the mastermix because of its HRMA performance. The G6PC amplicon is 46 bp in size and has a characterized melt temperature of 75.6 $^{\circ}\text{C}$.

2.3 Results and Discussion

2.3.1 Device Fabrication and Calibration

The microfluidic system was fabricated from COP due to its high transparency, low autofluorescence, low water absorption, and low gas permeability. To ensure compatibility with the high temperatures encountered in PCR, a grade of COP (Zeonex 1420R) with a glass transition temperature (T_g) of 135 $^{\circ}\text{C}$ was selected for this work. The two step embossing process (Figure 2.2) provided high resolution patterning of the COP substrate. Because channel features were milled directly into the initial aluminum mold, the aluminum surface could be easily polished to ensure excellent optical quality in the final COP device. The secondary mold was embossed from PEI for its high strength and high T_g . The PEI mold proved to be very durable over tens of embossing cycles, and can be easily reproduced from the aluminum master as PEI mold tolerance degrades.

The solvent bonding process developed in this work was very robust, allowing permanent sealing of the microchannels without any observable deformation of the 50 μm thick COP sealing film. This stands in contrast to thermal bonding methods, where channel deformation is commonly observed even when using significantly thicker and stiffer substrates.¹⁸ Metallization of the sealing film employed a 15 nm Cr layer, which was found to improve adhesion of Au to COP. The Au layer thickness of 75 nm was chosen to achieve a desired nominal resistance

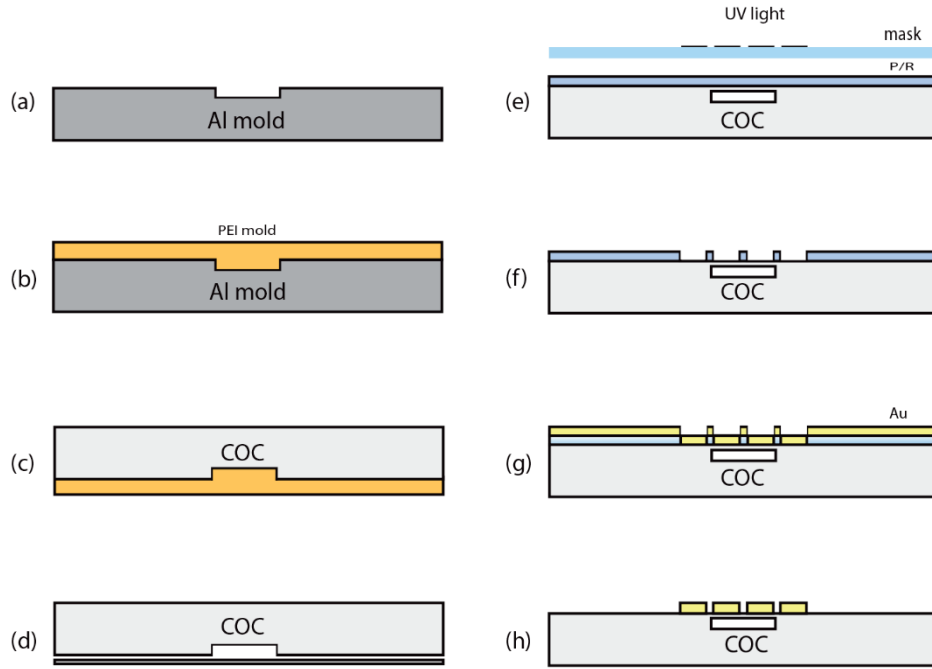


Figure 2.2: (a) CNC mills channels in Aluminum mold. (b) Polyetherimide (PEI) mold is embossed with Al mold. (c) COP resin is molded onto PEI mold. (d) COP wafer is exposed to decalin solvent and bonding to COP thin film. (e) Negative lift-off resist is spun onto COP wafer and photolithographically patterned. (f) COP wafer is developed (g) Cr and Au is deposited on top of COP wafer. (h) Final COP with Cr/Au elements

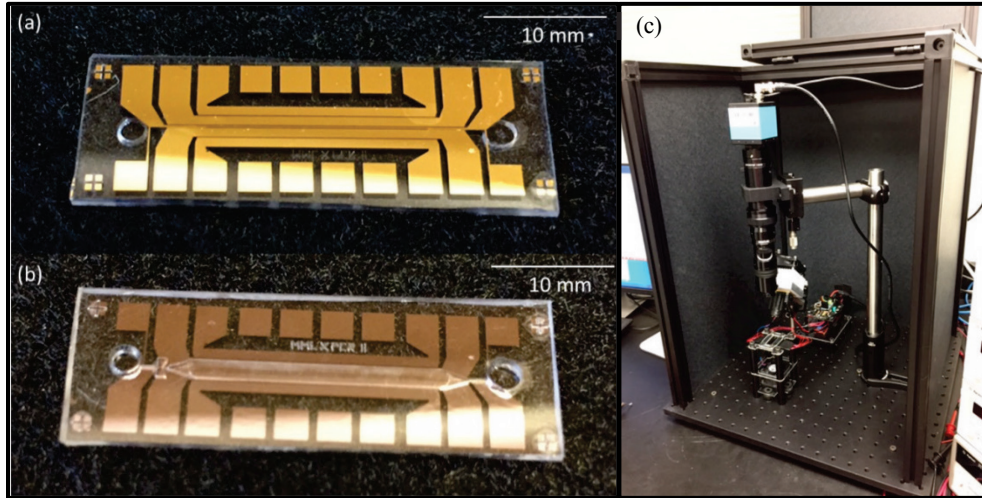


Figure 2.3: Image of the XChip device and system. (a) Image taken from the bottom of the device of the Au heating and sensing elements. (b) Image taken from the top of the XChip of the microfluidic features. (c) Image of the XChip benchtop system.

of $125\ \Omega$ for the heating electrodes and $75\ \Omega$ for the sensor electrode. Images of a fabricated device are shown in Figure 2.3.

Burn-in of the electrodes was found to be critical for achieving accurate temperature measurements and high sensing resolution. Prior to burn-in, significant hysteresis was observed for the sensors, with up to 1.5% variation in sensor resistance at $60\ ^\circ\text{C}$ (see Appendix 1). After 3 burn-in cycles, hysteretic variations were reduced to less than 0.5% within the full PCR temperature range. The temperature coefficient of resistance (TCR) of each sensor was determined after burn-in for each individual chip. This calibration procedure (Appendix 10) was necessary due to large chip-to-chip variability. Even within a single COP wafer containing 6 individual devices, nominal resistance values were found to vary with relative standard deviations up to 4%. Burn-in is a standard process step in the manufacture of many temperature sensors such as discrete thermistors, and can be implemented in a highly parallel process for low cost fabrication.

2.3.2 *Passive Sample Loading*

Sample loading was performed by pipetting a defined reaction mixture volume into the inlet well of the device. As the mixture is deposited into the well, capillary action pulls the liquid into the microchannel, resulting in automated filling of the PCR chamber. While COP is a weakly hydrophobic surface with a sessile water contact angle of approximately 95° ,⁷⁷ surfactant within the master mix solution lowers the surface tension sufficiently to generate moderate capillary flow within the microfluidic device. As sample fills the chamber, the liquid reaches a passive hydrophilic expansion valve incorporated into the device at the terminal end of the PCR chamber. The expansion valve consists of a sudden increase in the channel width, resulting in a Laplace pressure as curvature of the liquid/air interface is forced to increase while exiting the valve. At a sufficiently high Laplace pressure, the system reaches equilibrium and fluid flow is halted. While hydrophilic capillary expansion valves have been investigated by several groups,^{111,115–117} their use in thermoplastic PCR chips places significant demands on the valve design due to the low surface energy of the COP surface, the low nominal surface tension of the PCR reaction mixture, and the further reduction of surface tension that occurs by heating of the mixture during amplification. Burst pressure for a hydrophilic expansion valve is determined by the channel dimensions and the expansion angle between the surface normals within the channel and immediately past the exit,¹¹³ with smaller channel dimensions and larger expansion angles resulting in higher burst pressures. To enhance burst pressure within our devices, the width and depth of the valve region were reduced to 60 μm and 30 μm , respectively, while the expansion

angle was set at 120° . Expansion angles beyond this value could not be consistently realized due to limitations on machining precision during milling of the Al master mold.

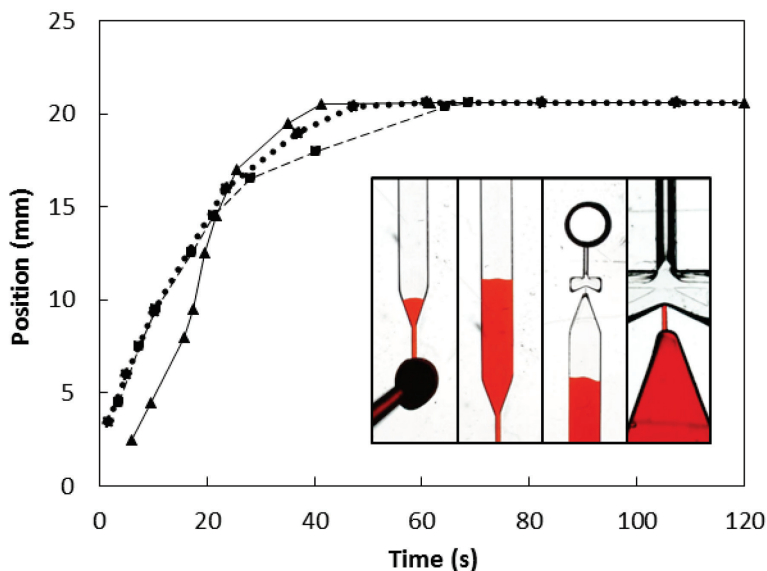


Figure 2.4: Plot of meniscus position (mm) versus time (s) for 3 different capillary loading and flow stop experiments. Images in the inset are not representative of actual data points but just shown for visual reference.

During loading, capillary pumping of the reaction mixture resulted in consistent filling of the chamber, with fluid reaching the expansion valve within approximately 50 s. Once reaching the valve, the capillary filling process halted and no further motion of the fluid was observed. Figure 2.4 shows the measured positions of the fluid front within the chamber for 3 independent filling steps, together with images of the process including the final valving stage. Performance of the valve was evaluated over the course of 50 thermocycles, with no bursting of the valve observed. Compared to previous reports of large expansion angle valve designs,¹¹⁶ the demonstrated ability to maintain a long-term passive seal using low surface tension fluids is unique. This simple and robust passive loading method

serves to reduce operational error while eliminating the need for complex fluidic interfacing or pumps during the loading process.

2.3.3 Thermal Performance

While there is not a precise definition for “ultrafast PCR”, a term commonly used to refer to systems capable of exceptionally rapid amplification, one interpretation is that an ultrafast PCR assay should provide amplification times below 10 min, supporting routine use in point-of-care settings where assay results can be quickly communicated to the patient. For a typical assay requiring 30 cycles for complete amplification, this implies a required cycle time on the order of 20 s.

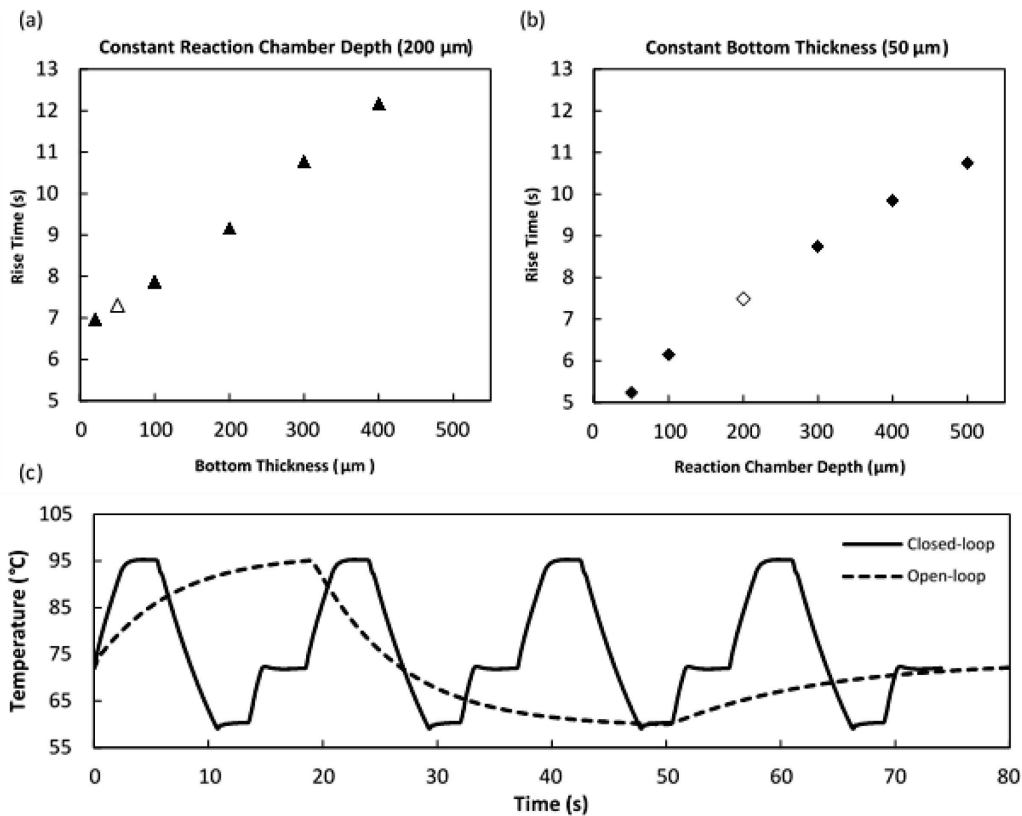


Figure 2.5: Parametric evaluation of different device designs plotting total rise time for a complete PCR cycle. (a) The reaction chamber depth was kept constant at 200 μm while bottom thickness was varied from 50 - 400 μm. (b) The bottom thickness was kept constant at 50 μm while the reaction chamber depth was varied from 50 to 500 μm. (c) Temperature vs. cycle time plots for the system using both open-loop and closed-loop control. The time cycle for closed-loop control system is 18.5 seconds, while the time cycle for open-loop control system is 80 seconds.

To evaluate the potential for our thermoplastic PCR device to reach this target, numerical simulations were used to evaluate the impact of chip dimensions on thermal response of the system using realistic values for forced convective cooling of the chip surface and current density limits for the heater electrodes. Rise times were extracted from models for various device designs over a range of thicknesses for the COP sealing film as well as a range of reaction chamber depths in the microfluidic substrate (Figure 2.5 a,b). From these results, a direct correlation between each geometric parameter and the thermal rise time is observed, suggesting that smaller sealing layer thickness and chamber depth are desired. Devices were fabricated using a sealing layer thickness of 50 μm since the impact of this parameter on thermal response for lower thickness values was minimal. Furthermore, while devices with thinner layers were attempted, fabrication of chips with sealing films below 50 μm proved challenging due to film deformation during bonding. For the reaction chamber, a depth of 200 μm was selected as a tradeoff between rapid thermal response and high optical pathlength for sensitive fluorescence measurements. In practice, fluorescence intensity was not found to be a limiting factor for the system, indicating that future designs could further enhance thermal response times through the use of shallower reaction chambers.

The data in Figure 2.5 a,b is presented for open loop control of the system. To further enhance thermal response, a closed loop strategy using PID control was implemented in the numerical environment to dictate the input voltage applied to the heaters based on feedback from the sensor temperature built into the model. The PID parameters were optimized manually, with the maximum input voltage limited

to account for the physical constraints of the actual heating elements, applied to a model based on the fabricated chip dimensions. Using this approach, closed loop performance could be significantly improved over open loop control (Fig. 2.5c). To confirm the closed loop numerical model, thermal performance was characterized in a fabricated device containing both thin film temperature sensors and a thermocouple embedded in the reaction chamber during device sealing, with identical PID parameters used for the software-defined control scheme executed by the microcontroller. A comparison of model results with data from both sensors is presented in Figure 2.6. It is evident that the initial part of both the denature and anneal steps exhibit a dynamic offset between the thin film sensor and the reaction chamber thermocouple measurements. This offset was compensated for during the software temperature conversion step to improve sensor accuracy and control performance. Using this offset to infer actual chamber temperature, a cycle time of

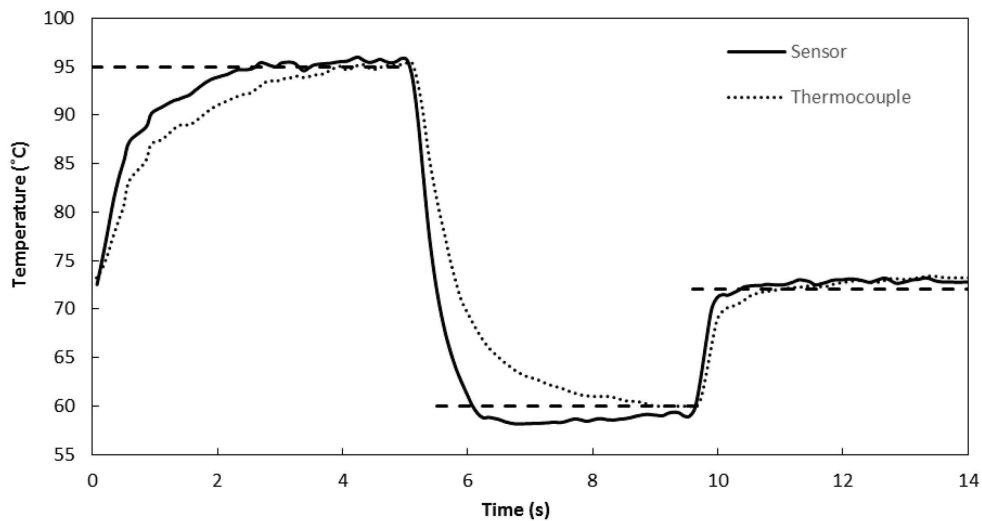


Figure 2.6: Plot of 14 second cycle time with thermocouple embedded into reaction chamber to verify sensor accuracy. From this data I applied a further calibration factor equation to our temperature conversion to compensate for thermal lag in the chamber versus sensor during denature and anneal steps.

14 s was achieved, slightly faster than a modeled cycle time of 19 s when employing identical dwell times at each temperature set point, and well within our targeted time of 20 s per cycle.

2.3.4 Assay Validation

Microfluidic devices were fabricated based on the optimized design informed by the numerical model, and used to validate performance of the microfluidic system using a commercial G6PC assay for diagnosis of type I glycogen storage disease. Devices were run on a custom built benchtop system using off-the-shelf electronic and optical components for automated temperature control and data analysis (Appendix 9). The software-defined PCR routine (Appendix 2) implemented by the microcontroller consisted of a 30 s hot start at 95

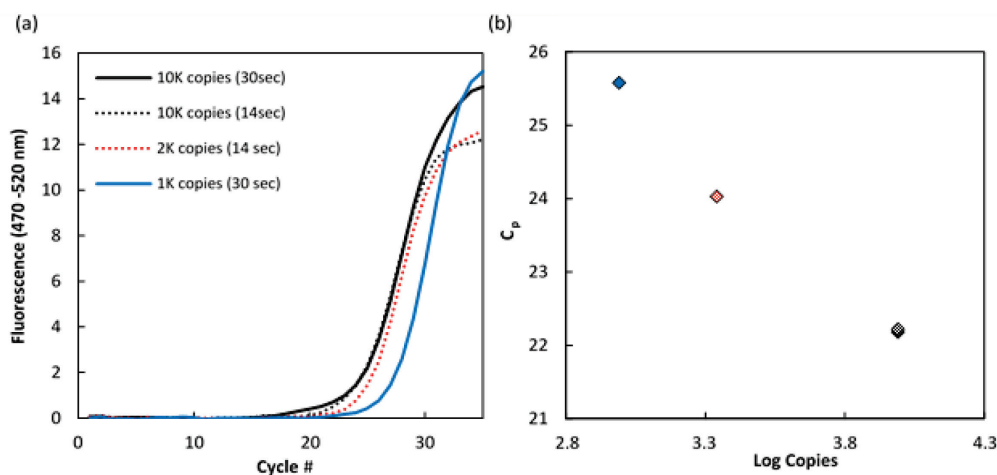


Figure 2.7: (a) Plot of PCR amplification curves at different concentrations and cycle times. (b) Plot of C_p versus concentration. C_p values for each test were calculated by taking the standard deviation (σ) of the background fluorescence during cycle's 3-15 for each data set. This σ was multiplied by a factor of 20 to determine a threshold value for each independent data set.

$^{\circ}\text{C}$, followed by 35 cycles of 95 $^{\circ}\text{C}$ for 5 s, 66 $^{\circ}\text{C}$ for 4.5 s, and 72 $^{\circ}\text{C}$ for 4.5 s. A final extension step at 72 $^{\circ}\text{C}$ for 30 s was performed on cycle 35. The total PCR run time was approximately 8.5 min. Separate chips were used to run the assay with

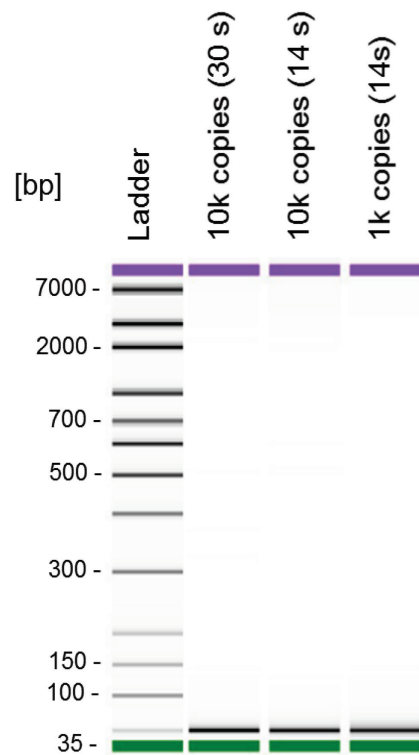


Figure 2.8: The PCR product from three experiments were run under high sensitivity electrophoresis on an Agilent BioAnalyzer 2100. The correct G6PC product is 45 bp in length while the instrument measured XChip product to be 51, 52, and 51 bp for each respective chip sample.

10^3 , 2×10^3 , and 10^4 copies of initial template. Identical dilutions at 10^4 copies were run at both 30 s and 14 s cycle times to evaluate the impact of dwell times on amplification. The resulting amplification curves for each case are presented in Fig. 2.7a, and extracted C_p values are shown in Fig. 2.7b. No statistically significant difference in C_p was observed for the case of 10^4 copies at 14 s and 30 s, indicating that the shorter cycle time is sufficient to achieve efficient on-chip amplification for the G6PC assay. The resulting plot of C_t vs. target copy number reveals a log-linear relationship suitable for quantitative analysis over the 1-log dynamic range shown in Fig. 2.7b.

Following PCR amplification, on-chip HRMA analysis was performed using a software defined routine (Appendix 3). In HRMA, controlled denaturing of amplicons with high temperature resolution enables sequence-specific DNA melting temperatures to be evaluated,¹¹⁸ providing additional information about the PCR product without the need for an additional instrumentation or use of a post-PCR assay. Using the integrated microfluidic chips, HRMA analysis was completed in 6 min. A typical melt curve resulting from on-chip HRMA of the

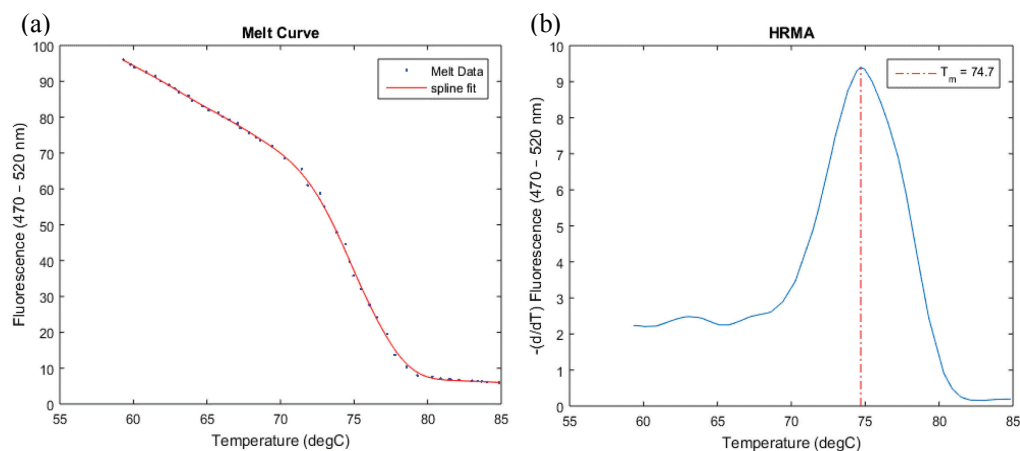


Figure 2.9: (a) Plot of melt curve data collected on chip after PCR amplification. Data is then fit with a spline to mitigate sensor noise that results in a non-smooth melt peak. (b) HRMA analysis is done by taking the negative derivative of the spline fit equation at each respective data point and plotting the curve (Appendix 4). The maximum $-(d/dT)$ in fluorescence is identified as the amplicon melting temperature.

G6PC product immediately following PCR is shown in Fig. 2.9a, and the final HRMA plot consisting of the negative derivative of the melt curve data is presented in Fig. 2.9b. The average melting temperature determined for all tested devices was 75.1 ± 0.5 °C, which compares very well against the known melt temperature range of 75.0 - 75.6 °C for homozygous wild type. In addition, capillary gel electrophoresis was performed on post-PCR solution extracted from 3 of the devices. This analysis revealed 51 bp fragments from the microfluidic devices,

which compares well with a theoretical G6PC amplicon length of 46 bp (Fig. 2.9), further validating the reaction product consistent with the previous HRMA analysis.

2.3.5 Device Cost and Power Consumption

It is notable that the total power consumption required for chip operation is quite low. The average power required during the assay for thermal control using the integrated thin film heating and sensing electrodes was only 42 mW, while the average power for the electronics including microcontroller, LED, and camera was 390 mW. The largest power demand was imposed by the cooling fan used to define the convective cooling boundary condition on the backside of the chip, which required 6 W of power under continuous operation. The overall power requirements may be significantly reduced by operating the fan only during the cooling stage of each thermal cycle, employing a more efficient thermoelectric cooling element, or eliminating active cooling and relying on natural convection alone, with a commensurate increase in total assay time.

Finally, we note that chip fabrication costs are low due to the reliance on thermoplastics as the substrate material and the use of common fabrication techniques borrowed from the microelectronics industry, making the resulting technology appropriate for single-use disposable assays. The estimated fabrication cost for low volume production, including all materials, microchannel molding steps, capping film formation, chip bonding, photolithography, Cr/Au metallization, and lift-off processing, is estimated at approximately \$4 per chip. Future improvements in fabrication throughput, for example through the use of roll-

to-roll imprinting and lithography techniques, could substantially reduce these costs for high volume manufacture.

2.4 Conclusion

This work demonstrates a disposable microfluidic PCR chip with integrated thin film heating and sensing elements that takes advantage of a thin thermoplastic sealing layer to achieve extremely rapid PCR, together with integrated hydrophilic valves to achieve highly repeatable and automated loading of sample into the PCR reaction chamber. Multiphysics modeling enabled parametric evaluation of chip design parameters and optimization of the system to realize cycle times of 14 s and full PCR in 8.5 min. Amplification of a mutant G6PC gene sequence from hgDNA indicative of Von Gierke's disease was successfully performed under a variety of PCR conditions, with on-chip HRMA proving to be robust for identifying PCR product melting temperature within 0.6% of the known value for G6PC. Using the disposable chips, real-time quantitative PCR was successfully performed over a 1-log dynamic range. Because the microfluidic technology is compatible with a simple, small footprint, and low cost benchtop system for temperature control and optical readout, while also supporting automated sample loading without the need for external pumps or volume control, the system has significant potential as a point-of-care platform for PCR diagnostics.

Chapter 3: Hydrophilic Valve Trap Sample Discretization

3.1 Introduction

In order to enhance the capability of the low cost disposable device for rapid PCR and HRMA proposed in the Chapter 2, different strategies for simple and automated multiplexing were explored to incorporate into the platform. An important requirement of these multiplexing strategies would be compatibility in point-of-care settings, and thus, should not require any non-standard equipment for operation.

3.1.1 Hydrophilic Valve Trap

Building off the prior work with the hydrophilic valve (Figure 3.1a), a technique utilizing a stop valve to discretize sample into individual traps with equal

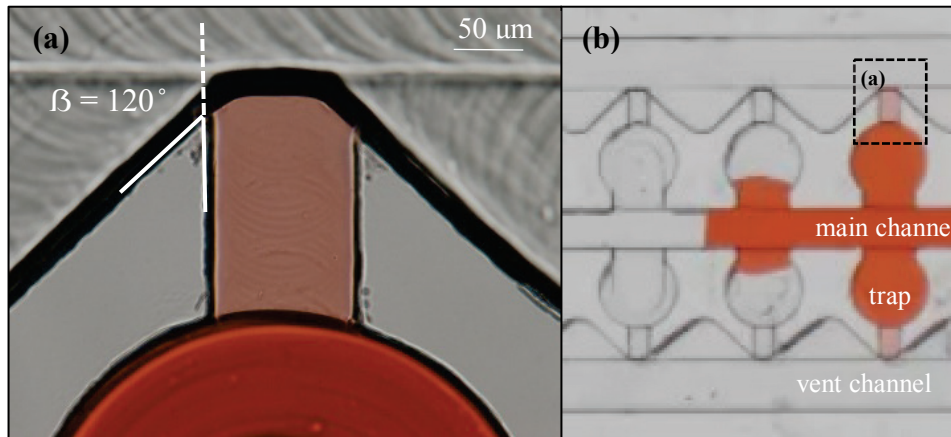


Figure 3.1: (a) Close up view of the high- β capillary valve. (b) Overview diagram of the trap array.

volumes was developed (trap-array). As seen in Figure 3.1b, each trap is fluidically coupled to the filling channel at its entrance, with a passive hydrophilic valve fabricated on the opposite side. The array filling process is depicted in Figure 3.2 for the case of a 20-element array. As sample flows through the filling channel,

fluid is sequestered within each reaction well, with the hydrophilic valves allowing air to be fully removed while preventing fluid flow out of the traps. As the sample plug traverses the full array, each trap element is filled with no leakage. After each trap is primed the main channel is purged so that excess sample is removed and the main and vent channels are left completely open to atmosphere for oil backfill. The oil backfills purpose is twofold; to completely isolate each reaction chamber to prevent the migration of primer contaminants to other wells; and to prevent evaporative losses that occur with small volumes under thermocycling conditions.

3.3.2 Manual Syringe Fluid Actuation

Several different approaches were considered to achieve on-chip fluid actuation with minimal or no manual intervention required. An important constraint on the fluid actuation method would be the balance of actuation force and the hydrophilic valve burst pressure. Fluid actuation by manual syringe pumping is one method explored for trap array operation. In this technique a syringe is interfaced with the outlet of the chip such that when the plunger is retraced manually the sample resting in the inlet is pulled through the main channel by the resulting negative pressure gradient. The sample primes each well and is then fully evacuated from the chip into the syringe connect at the outlet.

3.3.3 Thermopneumatic Pump Fluid Actuation

Another technique that was explored for trap array operation was fluid actuation by thermopneumatic pumping. A closed chamber is fabricated downstream of the trap array which has heating elements built underneath. The chamber is then heated while sample is loaded at the inlet. The chamber is

subsequently cooled causing the expanded gas within the chip to cool and condense causing a slight vacuum that pulls the sample through the main channel priming the traps along the way. The ΔT of the chamber dictates the loading speed and efficiency. Since this platform already integrates heaters for thermocycling this functionality can be easily incorporated.

3.3.4 Capillary Pump Fluid Actuation

While both syringe pull and thermopneumatics show simple and relatively automated loading operation, employing capillary force for the trap array shows far more potential for practical point of care systems because it does not require any extra systems or equipment. Capillary loading of the trap array is accomplished with the addition of surfactant to PCR reaction solutions such that the sample is drawn through the main channel via capillary force. Upon complete priming of the main channel and traps the advancing meniscus is then routed to a hydrophilically modified PVDF membrane that immediately absorbs any remaining volume completely purging the device and leaving it open for oil backfill.

3.2 Materials and Methods

The microfluidic substrate was constructed of COP (Zeonex 1420R, Zeon Chemicals, Louisville, KY). Approximately 15 mL of resin pellets were placed on the PEI secondary mold and heated to 190 °C for 30 min in the hot press. Once heated, the pressure applied to the stack was increased in 50 psi increments every 10 min, and held at a final pressure of 250 psi for an additional 10 min. The resulting COP plaque had a thickness of approximately 550 μm . Main channel sections and

trap were 100 μm deep while hydrophilic expansion valve regions were 30 μm deep. Input ports were manually drilled using a drill press. The microfluidic substrate was sealed by a 50 μm thick COP film (Zeonex 1420R, obtained as samples from Zeon Chemicals) using a solvent bonding technique modified from a previously developed procedure.²⁰ The channel side was exposed to 35% decahydronaphthalene in ethanol (w/w) for 7 min, rinsed with 100% ethanol, and blown dry with N_2 . The multilayer substrate was then pressed at 200 psi and 50 $^\circ\text{C}$ for 10 min in a hot press to complete the bonding.

3.3 Results and Discussion

Three separate strategies for fluid actuation were tested for trap array operation and characterized based on the following criteria: repeatability, loading speed, and integration.

3.3.1 Manual Syringe Trap Device Operation

Fluidic actuation by manual syringe pull was the first trap array loading technique explored for this platform. Sample loading was performed by pipetting a defined reaction mixture volume into the inlet of the device. Once the sample sealed the only open outlet the syringe plunger was lightly pulled to create a small negative pressure gradient. The negative pressure gradient pulled the sample through the device where it diverted flow into each trap as it flowed through the main channel. The use of 10 mL syringes provided the most repeatable loading as opposed to large volume syringes due to the smaller negative pressure gradient created when manually pulled. Sample was pulled completely through the device until it was

cleared of sample and open for oil backfill. Complete sample loading and purge

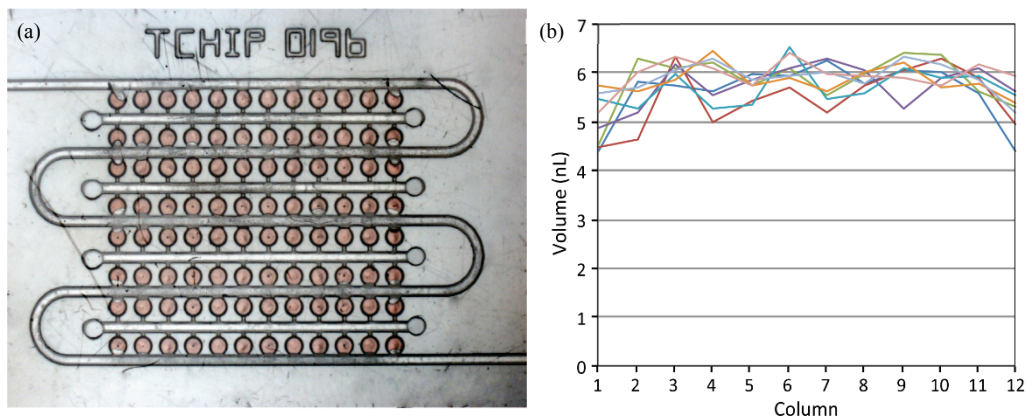


Figure 3.2: (a) 96-well array with a single filling channel and hydrophilic valves to control well volume during loading. (b) Well volumes across each row of the array (average 5.8 ± 0.5 nL).

was accomplished on the order of seconds for the 96-trap array chip shown in Figure 3.2a. Trap volumes can exhibit relative standard deviations of around 10%, with bias toward lower fill volumes for the outermost elements for each row (Figure 3.2b). The best results using this technique were achieved with sample surface tensions \geq water (72 (dyne/cm)), which presents a challenge since most off-the-shelf PCR solutions are prepared with small concentrations of surfactant. However, the use of $> 90^\circ$ expansion angles for the valves was not explored for this method and could conceivably enable the use of lower surface tension solutions.

3.3.2 Thermopneumatic Pump Trap Device Operation

Fluidic actuation using a thermopneumatic pump was another technique that would allow for trap array loading without requiring supporting hardware during operation. First the pump chamber was heated to 85°C to expand the gas within the chip while the inlet was left open to equalize pressure with atmosphere. When the chamber was sufficiently heated sample was loaded by pipetting a defined volume of reaction mixture into the inlet of the device creating a closed

system. The heated chamber was then cooled down to 23 °C causing the expanded gas to contract and create a negative pressure gradient drawing the sample through the chip towards the downstream pump chamber. The chamber was designed to be sufficiently large such that there would be a large enough Δ Volume to draw the sample completely through the trap array section. A maximum ΔT of 60 °C was used to actuate the sample, using temperatures > 85 °C would result in sample evaporation that would condense in the vent channels during cooling. If condensation formed near the valve ending the burst pressure would be

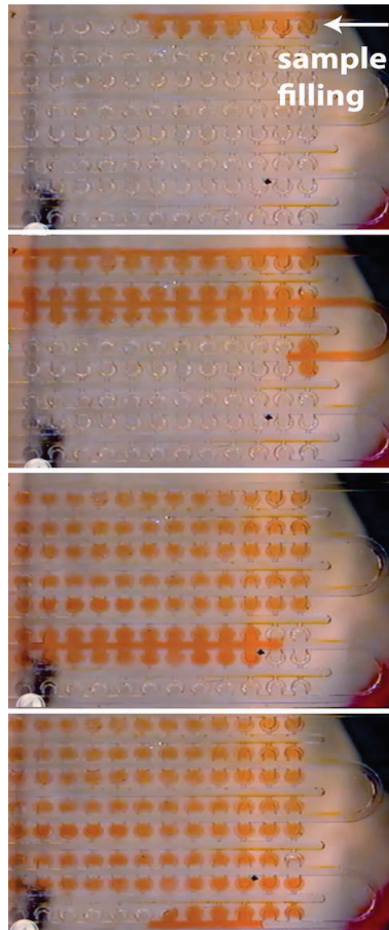


Figure 3.3: Thermopneumatic pump operation of a 96-trap array. Images are taken over 6 min to capture the progression of sample through the device.

significantly reduced because of the increase wettability. Sample loading was accomplished in approximately 6 min for the 96-trap array chip shown in Figure 3.3. The rate of sample flow is dependent on the rate of temperature change of the pump chamber, which is constrained by the thermal mass of the Peltier element and poor thermal conductivity of the substrate. Integration of thermopneumatic pumping would involve patterning thin film metal elements under the pumping chamber and while it was not attempted explicitly, it would be very straight forward to implement using the metallization process outlined in Chapter 2.

3.3.3 Manual Syringe Trap Device Operation

Capillary action was the final fluid actuation method explored for trap chip operation. Sample loading by capillary action was performed by introducing a sample solution into the inlet that would be drawn through the device by the fluid interaction with the microchannels. The sample solution would then be purged from the main channel using a PVDF absorbent membrane acting as a capillary pump downstream of the trap array region. Sample solution surface tension and trap geometry dictated the trap array loading speed and repeatability. Thus, Tween20 surfactant and TritonX-100 surfactant were added to off-the-shelf PCR solutions at concentrations of 0.1-0.5% (w/w) and 0.04-0.2% (w/w) respectively for optimization. The highest repeatability of trap array loading was achieved using 0.04% (w/w) TritonX-100 with a loading plus purge time of approximately 45 seconds. Additionally, it was found that the use of lower surface tension samples required an improved valve design that increased the expansion angle (β) from 90° to 120°. Figure 3.4 shows time stamped images taken during loading purge and oil

backfill of a 120° expansion valve trap array design. In order to prevent unwanted fluid pinning of the receding front, a sample volume greater than combined volume of main channel and trap array was required so that the advancing meniscus front could make contact with the capillary pump before the receding front entered the main channel. Otherwise the advancing and receding fronts would equilibrate inside the channel and could not be effectively purged. Additionally, it was found that the absorbent membrane must protrude into the main channel so that it could make contact with the entire advancing front interface and not just where comes

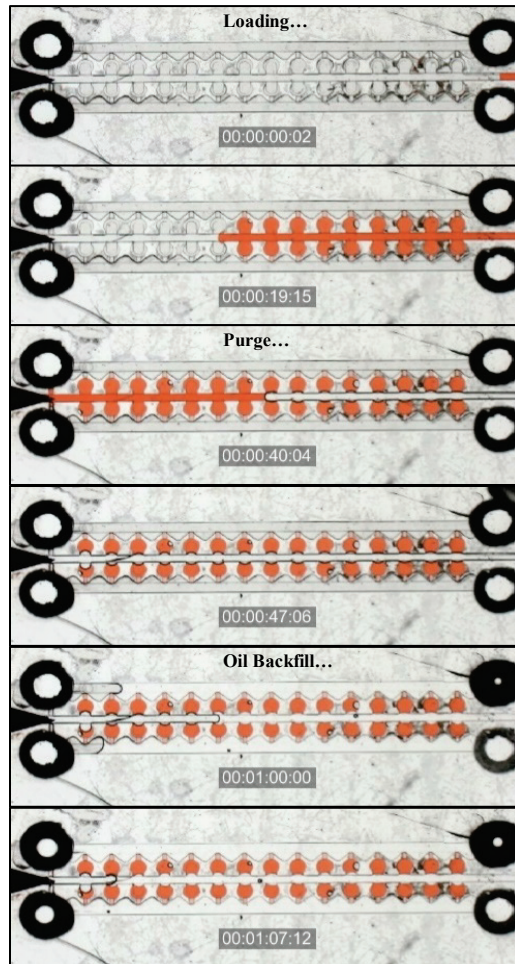


Figure 3.4: Images taken during capillary loading of 30 trap array showing each of the three phases of operation.

into contact along the channel walls. Therefore a wedge shaped opening to the membrane was used so that during insertion the point of the wedge could be automatically guided into the main channel. Capillary loading also has the advantage that it can be kept open to atmosphere during operation, meaning that vent chamber valving required in the two previous strategies is not required in this case.

3.4 Conclusion

In summary a new microfluidic technique for automatic discretization of microliter-scale volumes of fluid using only passive chip elements has been presented. Trap array fabrication was optimized to achieve high quality expansion valves for robust operation. Three loading strategies were explored and characterized based on repeatability, loading speed and integration. Capillary action showed the most potential in this regard and through optimization of surfactant concentration achieved loading times on the order of 1 min. Sample and oil introduction could be accomplished using only a pipette with no dependence on volume control as the system passively purges any leftover sample. Trap array densities of 30 and 96 were also demonstrated. Additionally, a custom tool for primer spotting was tested and showed excellent spatial control such that uniform 65 μm diameter primer spots could be aligned to the center of each trap. Alignment was kept intact through the bonding process using a custom alignment jig.

Chapter 4: Staggered Trap Arrays for Robust Microfluidic

Sample Digitization

4.1 Introduction

Sample digitization, in which an initial sample is discretized into multiple smaller volumes, is an important operation required in many applications such as genomics, clinical diagnostics, and drug discovery. The conventional approach to forming an array of discrete fluid volumes from an initial sample solution has been to rely on robotic fluidic handling.¹¹⁹ However, this approach requires cumbersome and costly equipment, suffers from unfavorable scaling in multistep assays,¹²⁰ and is generally restricted to discretized sample volumes in the microliter range. Moreover, the need for an open substrate such as a microwell plate for deposition increases the risk of external contamination, introduces the need to limit sample evaporation, and constrains the types of assay operations that may be performed on the discretized volumes.

A variety of microfluidic technologies have been developed to enable automated sample digitization within enclosed flow systems. One of the most common and powerful approaches to microfluidic digitization is droplet generation,¹²¹ an active digitization process wherein a sample volume is dispersed within an immiscible phase to create small uniform reactors defined by individual droplets. Microfluidic droplet generators allow the flow rates of the continuous and dispersed phases to be adjusted for control over the volume and production rate of the digitized sample volumes, and can be readily used for the formation of high

density arrays. However, droplet generation is an active digitization method requiring continuous and precise flow control for monodispersed droplet formation, necessitating the use of fluidic interfacing and flow control hardware, thereby increasing the complexity and cost of the final device. Furthermore, because of the active nature of the droplet generation process, the resulting droplets typically require additional mechanisms downstream for manipulation and assay analysis. While a range of methods for downstream control via droplet trapping and release using hydrodynamic,^{122–124} optical,¹²⁵ or acoustic,¹²⁶ manipulation have been explored, these added operations can degrade the potential for simplicity, affordability, and integration offered by microfluidics. Electrowetting-on-dielectric (EWOD) represents an alternative active digitization technique that enables on-demand formation of discrete sample volumes together with controlled manipulation of individual droplets for subsequent assay operations.^{127,128} In the EWOD technology, differential capillary forces are generated across a droplet by controlling the surface contact angle between the droplet and an underlying substrate through application of an external electric potential, allowing sample packets to be segregated and transported by direct voltage control.¹²⁹ Despite this unique functionality, EWOD devices can present challenges in scalability related to electrode addressing, demand high voltages for operation, and require relatively complex fabrication methods to define both the dielectric and electrode layers needed for reliable device operation.

Driven by the need for simpler and more robust methods of sample discretization, a number of passive digitization methods have been developed.

Passive sample digitization takes advantage of processes that do not require precise control over fluid flow or the use of active control elements, such that discrete volumes are created on-chip automatically within spatially indexed locations. A central advantage of these passive methods over active digitization is that the instrumentation required for compartmentalization is greatly reduced or eliminated, making these techniques very well suited for use in devices where low cost and simple operation are important considerations. The passive sample digitization concept has been successfully applied to various open fluidic platforms in which sample is discretized within arrays of patterned microwells by sequential well priming and selective dewetting of the surrounding field while leaving individual fluid volumes anchored within the wells.¹³⁰ Similarly, selective patterning of hydrophilic regions,¹³¹ or porous absorbent materials,¹³² within wells on a hydrophobic surface has been employed to initiate wetting in specific locations while allowing excess sample to be easily removed. A related method has been applied to sealed microfluidic systems, allowing the passive discretization of sample in enclosed microchannels. While various device geometries have been explored, they share a similar approach in which sample is introduced through a microchannel by pressure driven flow,^{89,133–136} vacuum,^{99,137,138} or centrifugal,^{72,73,91} actuation to prime a series of wells fluidically connected to one of the microchannel walls, followed by the introduction of an immiscible oil phase to remove residual sample from the microchannel. The oil flow serves to shear off sample from the filled wells, leaving digitized aqueous fluid volumes behind. The oil phase used to backfill the chip also serves to fully isolate the sample volumes

and prevent evaporation. In these devices, polydimethylsiloxane (PDMS) is commonly chosen as a substrate material due to its high gas permeability, enabling dead-end filling of the wells without trapping air bubbles during priming.¹³³ However, PDMS is less than ideal for many applications. In addition to the relatively high material and manufacturing costs associated with silicone elastomers, PDMS devices typically require that the microwells be filled with an oil phase prior to sample introduction, thereby enhancing filling of aqueous sample into the hydrophobic PDMS wells and improving sample retention during the final oil backfill step.¹³⁴ While thermoplastics present an attractive alternative to PDMS due to exceptionally low material costs and amenability to rapid replication-based fabrication, thermoplastics are not gas permeable and are generally low surface energy materials, making the reliable filling of closed on-chip chambers or wells challenging.

This paper describes a new approach to sample digitization that exploits the controlled pinning of fluid at geometric discontinuities within a microchannel. The technique employs two periodic arrays of microwells (sample traps) positioned on opposite sides of a microchannel, with the opposing arrays offset from one another along the channel length. Through proper design of the traps, sample is sequentially pinned at each trap entrance or exit during filling, enabling reliable and complete filling of the following trap before removal of fluid from the main channel by a downstream passive capillary pump. While the technique may be applied to devices fabricated from either hydrophilic or hydrophobic substrates, a unique aspect of the method explored here is the use of a weakly hydrophobic surface that allows the

discretization process to proceed without the need for any external flow control or actuation. An analytic model is developed for predicting the maximum ratio of trap depth to opening width at which complete trap filling will occur, and the model is validated through an experimental evaluation of the filling process using a set of devices fabricated with parametrically-varying trap geometries. Finally, the model is used as a predictive tool for the design and fabrication of a high aspect ratio 768-element staggered trap array, allowing the reliability of the filling process to be evaluated in a high density thermoplastic device that takes advantage of the polymer's moderate surface energy to achieve fully passive self-discretization without the need for any external pumps or other flow control elements.

4.2 Materials and Methods

4.2.1 Microfluidic Device Fabrication

Each self-loading and digitizing device was fabricated by milling channel and microwell features in a 2 mm thick COP plaque (Zeonor 1020, Zeon Chemicals, Louisville, KY) using a 3-axis computer numerical controlled (CNC) milling machine (MDX-650, Roland DGA, Irvine, CA). A hydrophilically-modified 125 μm thick polyvinylidene fluoride (PVDF) absorbent membrane (SVL04700, EMD Millipore, New Bedford, MA) with 5 μm pore size and was cut to a desired size using an automated craft cutter (Cameo Digital Craft Cutting Tool, Silhouette America, Orem, UT). The milled COP plaque was immersed in a solution of 35% decahydronaphthalene (Thermo Fisher Scientific, Rockford, IL) in ethanol (w/w) for 1.5 min, rinsed with ethanol, and blown dry with N₂. The absorbent membrane

was then manually aligned to a premilled chamber ($h = 130\ \mu\text{m}$, $l = 13.5\ \text{mm}$, $w = 1.4\ \text{mm}$) in the COP plaque before the multilayer device was pressed at 200 psi for 10 min at room temperature in a hot press (AutoFour/15, Carver Inc., Wabash, IN) to seal the device by solvent bonding.

4.2.2 Self-Loading and Digitization Operation

Loading experiments for all devices were conducted by using a pipette to manually load 2 μL of DI water containing 0.06% Triton X-100 (Sigma Aldrich), 5% glycerol (Sigma Aldrich), and blue food coloring for visualization. The glycerol and surfactant were added to lower the surface tension and assist in self-loading operations. Once the sample primed the device and the absorbent membrane removed excess sample the chip was imaged under a microscope to evaluate the self-digitization process. To quantify the loading efficiency, any trapping of small air bubbles or incomplete loading of a well was considered an unsuccessful discretization event. Self-loading was accomplished in approximately 30 s for devices with 30 or fewer traps, while higher density devices were primed and purged within approximately 5 min.

4.3 Results and Discussion

4.3.1 Trap Chip Design and Modeling

Sample digitization platforms relying on PDMS microfluidics commonly initialize the discretization process with an oil phase containing surfactant to overcome the hydrophobic substrate properties, and inhibit sample/substrate interaction that would otherwise prevent efficient sample loading. As a result,

pressure-driven flow is required for both oil and sample loading in these devices. On the other hand, eliminating the oil initialization step would allow the native surface energy of the substrate to be harnessed for self-loading of sample by capillary action, eliminating unnecessary workflow and enabling passive device operation without the need for external instrumentation. The staggered trap array concept achieves this goal while leveraging surface interactions to greatly improve digitization efficiency in thermoplastic microfluidic chips. The basic design of a staggered trap chip is depicted in Figure 4.1. The staggered trap chips were fabricated from COP, a weakly hydrophobic polymer, and loaded with an aqueous

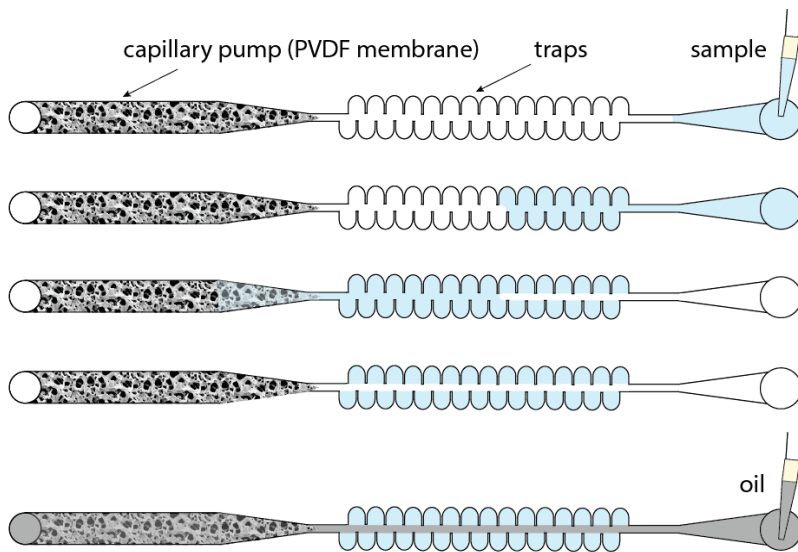


Figure 4.1: Illustration of the self-discretization workflow for a staggered trap array device.

solution to characterize discretization performance. To enhance self-loading a small amount of surfactant was added to the sample solution producing a measured sessile contact angle of 78° , and an advancing contact angle between 85° and 90° . After passive filling, excess sample was purged from the main channel by a passive capillary pump consisting of a hydrophilically modified PVDF absorbent

membrane integrated into the distal end of the microchannel. After sample discretization, the capillary pump further allowed the device to be backfilled with oil to encapsulate each digitized volume with an immiscible barrier to inhibit unwanted sample contamination and prevent evaporation. The traps, were chosen to reside on the side of the main channel as opposed to the top or bottom¹³⁴ as this provides the greatest flexibility in the fabrication of various trap geometries.

To explore the self-digitization process, three distinct trap chip designs were modeled and experimentally evaluated. As depicted in Figure 4.2a-c, the designs consisted of either a single row of traps, a symmetric double row of traps, or a staggered double row with a fixed offset between each row in the design. A parametric study was performed to assess the impact of trap geometry on sample discretization. The trap geometry used for this study is shown in Figure 2d, which defines the channel width (w_c), trap width (w_t), trap length (L), maximum length of filling into the trap (f), trap pinning offset (p), trap wall spacing (s) and advancing sample contact angle (θ_a). For each trap configuration, the relationship between the filling ratio (the ratio of filling length to trap width: $FR = f/w_t$) and the channel width ratio (the ratio of channel width to trap width: $CR = w_c/w_t$) was evaluated. The filling ratio provides a measure of the maximum length of a given trap that can be completely filled during sample introduction, while the channel width ratio serves as a useful design parameter defined by the relative channel and trap widths. The parameters defined in Figure 4.2d are applicable to all– designs, noting the single-sided and double-sided designs are degenerate cases with $p = \infty$ and $p = 0$, respectively. For each trap configuration, a geometric model was used to derive a

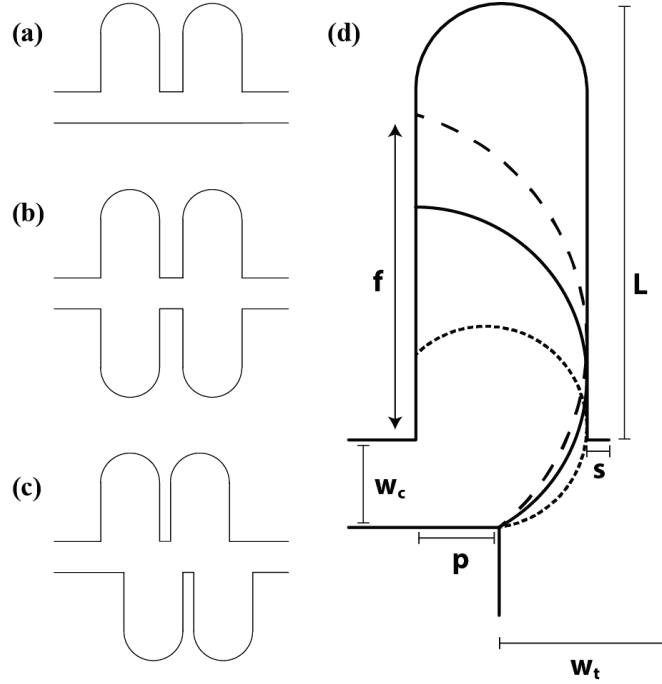


Figure 4.2: Schematic diagrams showing the trap configurations for (a) single-sided, (b) double-sided, and (c) staggered trap arrays. (d) Summary of geometric parameters used for model development.

numerical solution using a set of equations and constraints to solve for each point where the interface makes contact with the trap wall.

4.3.2 Single-Sided Trap Model

The single-sided design (Figure 4.2a) consists of a single row of traps branching off from one side of the main channel. As sample is pumped or wicked by capillary action to the entrance of a trap, the fluid becomes pinned at the trap entrance due to the geometric discontinuity, while surface tension forces continue to drive the advancing front along the main channel wall opposite the trap. As the front continues to advance, the effective contact angle between the fluid and inner wall of the trap increases until the initial energy barrier presented by the pinning point is overcome and fluid begins to spread into the trap. Surface tension stabilizes

the interface so that the contact angle of the advancing front is equal on both sides of the interface, with uniform curvature along the fluid/air interface. The advancing front eventually contacts the wall on the opposite side of the trap, at which point the filling process halts. If the filling length (f) is less than the trap length (L), a pocket of air remains sealed in the trap and filling is incomplete. However, if $f \geq L$ then no air becomes trapped and filling is successful. Note that because all trap designs employ a semicircular terminus, once the advancing fluid reaches the curved wall region the constant contact angle constraint ensures that the fluid interface will progress to the opposite wall and complete the trap filling process.

A geometric description of the filling process for a single-sided trap is shown in Figure 4.3a , while Figure 4.3b presents a sequence of images from a filling experiment using a fabricated COP device with dimensions of $w_t = 390 \mu\text{m}$ and $w_c = 200 \mu\text{m}$, and a measured filling length of $f \approx L/2$. As expected, incomplete filling is observed, with enclosed air remaining within the traps. From the given device geometry, an analytic model was obtained using a set of geometric relationships and constraints that allowed for each point where the interface makes contact with the wall to be determined numerically (Appendix 5). When considering the impact of contact angle on trap filling, a lower limit of 45° was imposed since smaller values would violate an assumption of positive interface curvature in the model. The resulting model was applied to a device design with dimensions identical to the experimental system, with results shown in Figure 4.3c,d. In Figure 4.3c the relationship between FR and θ_a is presented for a CR of 0.51, while in Figure 4.3d the relationship between FR and CR is presented at an

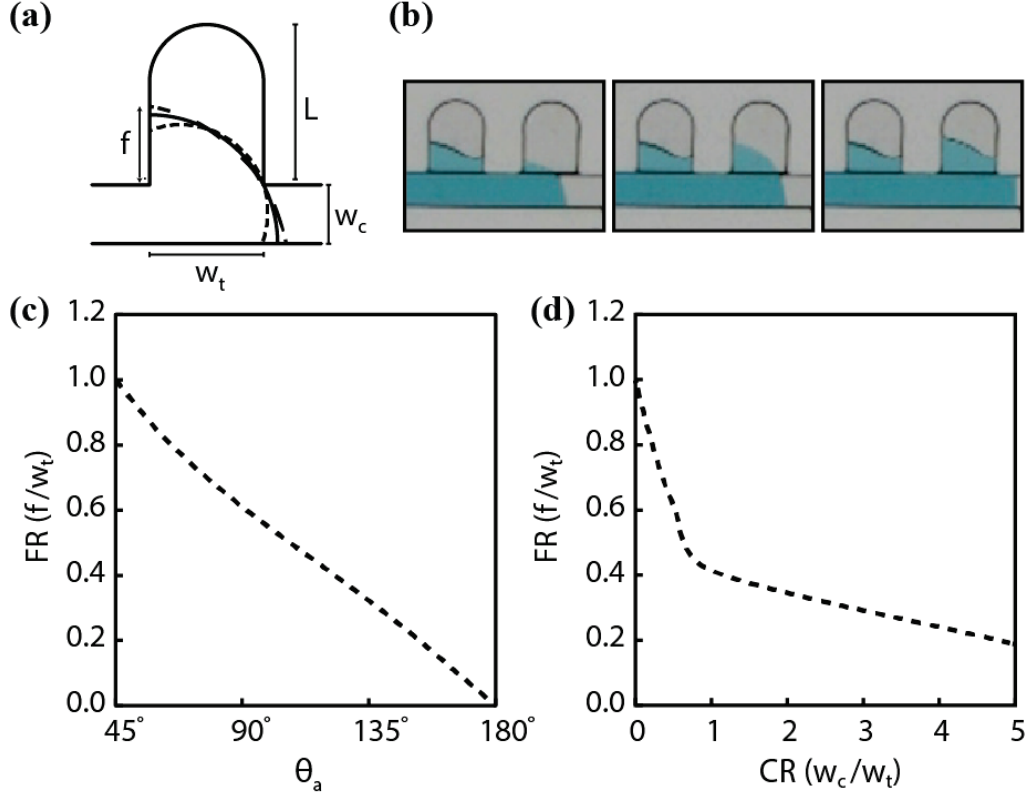


Figure 4.3: (a) Geometry for a single-sided trap configuration. (b) Images of the loading process for single-sided trap array with an $FR = 1.3$ and $\theta_a = 90^\circ$. Modeled relationships between (c) FR and θ_a at constant $CR = 0.51$, and (d) FR and CR at constant $\theta_a = 90^\circ$.

advancing contact angle of 90° . The fixed values of CR and θ_a in each case were selected to match the experimental conditions employed for experimental validation. For the given channel width ratio, a maximum achievable FR of 1 is predicted as θ_a approaches 45° , while no trap filling ($FR = 0$) is predicted as the contact angle approaches a superhydrophobic state with $\theta_a = 180^\circ$. Similarly, when $\theta_a = 90^\circ$ a maximum FR of unity is predicted when the CR approaches zero, while FR asymptotically approaches zero with increasing channel width ratio. Thus, for physically realizable trap array designs, the simple geometric model predicts that complete filling of single-sided traps may only be achieved when the trap aspect ratio (L/w_t) is well below unity.

4.3.3 Double-Sided Trap Model

The geometry of a double-sided trap is depicted in Figure 4.4a. In this design, the advancing fluid becomes pinned at both sides of the bifurcation into the traps until the effective contact angle with the inner trap walls grows large enough allow the front to proceed into both traps symmetrically. In practice, small disturbances, variations in surface properties, or variations in channel dimensions can result in asymmetric trap filling behaviors, as evident in the experimental images presented in Figure 4.4b for a double-sided trap chip with the same geometric parameters as the single-sided device described previously ($w_t = 390 \mu\text{m}$, $w_c = 200 \mu\text{m}$). Using the same modeling approach described for the single-sided

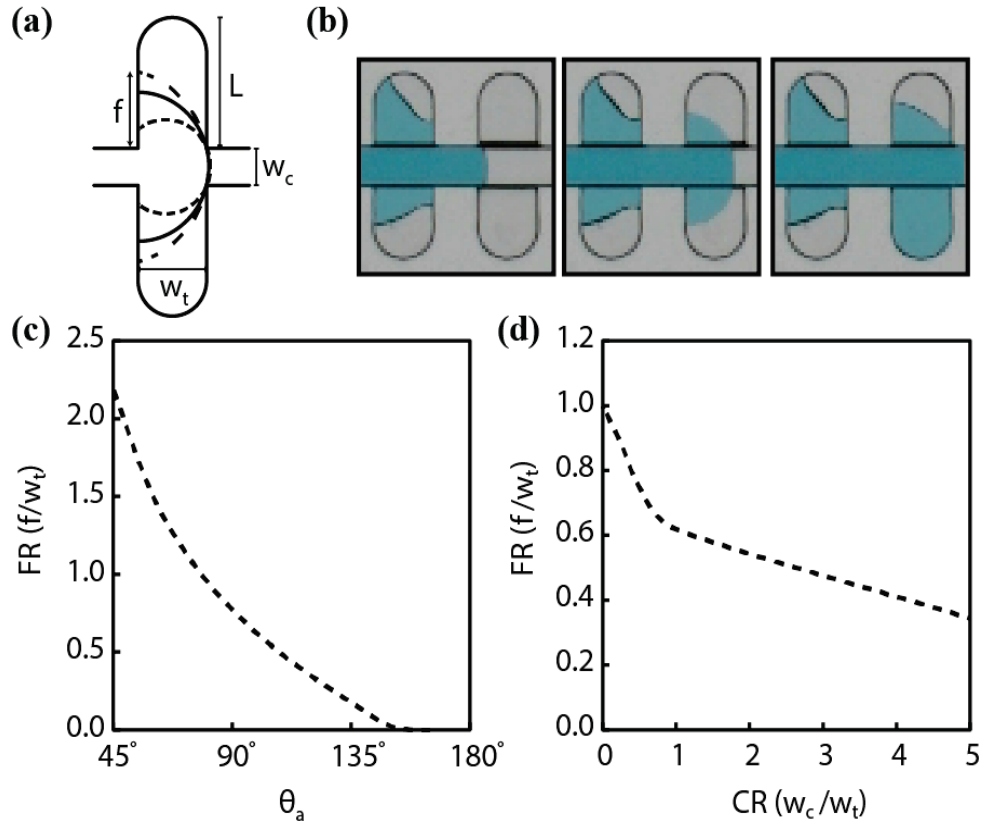


Figure 4.4: (a) Geometry for a double-sided trap configuration. (b) Images of the loading process for a double-sided trap array $FR = 1.3$ and $\theta_a = 90^\circ$. Modeled relationships between (c) FR and θ_a at constant $CR = 0.51$, and (d) FR and CR at constant $\theta_a = 90^\circ$.

traps (see Appendix 5), the influence of contact angle and channel width ratio on filling ratio was explored for the double-sided case (Figure 3.4c,d). For the selected device design, higher FR values above 2 can be achieved at low contact angles, while maintaining the contact angle at 90° and allowing CR to change yields only moderate improvement in FR compared to the single-sided traps. Similar to the single-sided case, the double-sided traps also yield a maximum FR of unity when $\theta_a = 90^\circ$, with FR approaching zero as CR is increased.

4.3.4 Staggered Trap Model

The staggered trap configuration (Figure 4.5a) was investigated as a novel approach to sample discretization capable of overcoming the limitations of single and double-sided trap designs, in which the maximum filling ratio is limited by coupled geometric and surface tension constraints of the microfluidic system. By taking advantage of asymmetric pinning in a staggered trap array, it becomes possible to manipulate the advancing front such that complete filling of high aspect ratio traps can be achieved using purely passive means. The trap loading process is shown for a fabricated device in Figure 4.5b. As seen in this figure, fluid begins to enter the lower trap with the fluid interface pinned at the discontinuity presented by the entrance to an offset trap on the opposite side of the main filling channel. The interface remains pinned as fluid traverses the wall of the lower trap. As with the single and double-sided designs, the conformation of the interface when it touches the opposite wall determines the distance the fluid is able to travel into the trap, and thus the maximum trap length for which complete filling can be achieved. For the

channel and trap dimensions in the present experiment, complete filling of the traps was achieved.

The range of filling length that can be achieved as a function of θ_a and FR was evaluated using a geometric model for the staggered trap design (see Appendix 5). In addition, the impact of pinning offset ratio (PR) on trap performance was also considered, where the PR is defined as the ratio of the pinning offset length to trap width (p/w_t). The dependence of FR on θ_a is presented in Figure 4.5c, using the same channel and trap dimensions as the single and double-sided configurations and with a fixed PR of 0.55. At a low contact angle of $\theta_a = 45^\circ$, the filling ratio is significantly larger than observed for the single and double sided cases at $FR = 3.7$, while a more moderate contact angle of 90° results in $FR = 1.4$. As with the single-sided design, FR decays to zero as θ_a approaches 180° .

The dependence of FR on CR when $\theta_a = 90^\circ$ is presented in Figure 4.5d, together with model results for the single and double-sided trap designs for comparison. In this figure, a family of curves reflecting varying pinning offset ratios is presented. When p/w_t approaches unity FR converges to the single-sided result. This is expected, since when $p \geq w_t$ for the case of $\theta_a = 90^\circ$ the advancing fluid front will touch the opposite trap wall before it can reach the pinning point, resulting in behavior identical to the single-sided case. However, when p/w_t approaches zero, FR does not converge to the double-sided case as might be expected given that the double-sided geometry is identical to a staggered design with $p = 0$, but instead continues to increase. This apparent discrepancy is due to the fact that the filling of the double-sided traps depends on simultaneous loss of

pinning at each of the opposing trap corners. In contrast, staggered traps require that the trailing trap corners provide ideal pinning as the leading traps begins to fill. In practice, neither assumption is entirely valid due to variations in surface finish and corner sharpness, as well as the influence of the upper and lower channel surfaces on the fluid interface, which is not considered in our geometric models. Additionally, the asymmetry of the staggered design means that the PR for traps on one side (PR) of the channel are not equal to the PR of the traps on the opposite side (PR*). The relationship between the PRs of each side is defined as $PR=1-PR^*$.

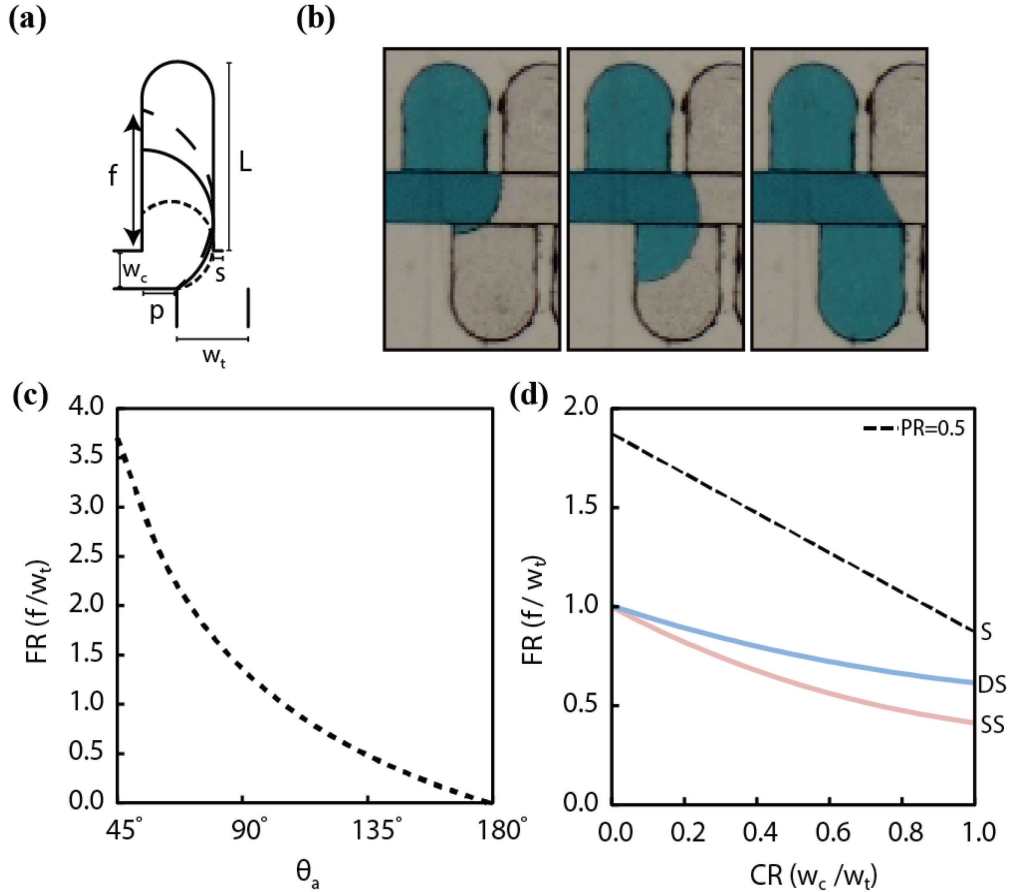


Figure 4.5: (a) Geometry for a staggered trap configuration. The p is different on each side of the main channel because on the staggered side the pinning offset will include a barrier wall. So the pinning offset in the staggered side $p^* = (w_t - p) + s$. (b) Images taken of the loading process for an experimental staggered SLD device with $w_t = 390 \mu\text{m}$, $w_c = 200 \mu\text{m}$, $\theta_a = 90^\circ$ and $PR = 0.55$. (c) FR dependence on θ_a . (d) FR dependence on CR for varying PRs.

As a result of these factors, optimal loading performance of the device is achieved at $PR=0.5$.

We note that the preceding analyses of filling ratio as a function of channel width ratio are limited to the case of $\theta_a = 90^\circ$. Trap filling performance for strongly hydrophilic or hydrophobic surfaces can vary significantly from the presented results. However, the observations derived from each model have wide applicability for typical thermoplastics used in microfluidic applications, which tend to have moderate surface energies and exhibit contact angles near 90° . For this important class of materials, the staggered trap model predicts significant improvement in achievable filling ratios compared to both the single-sided and

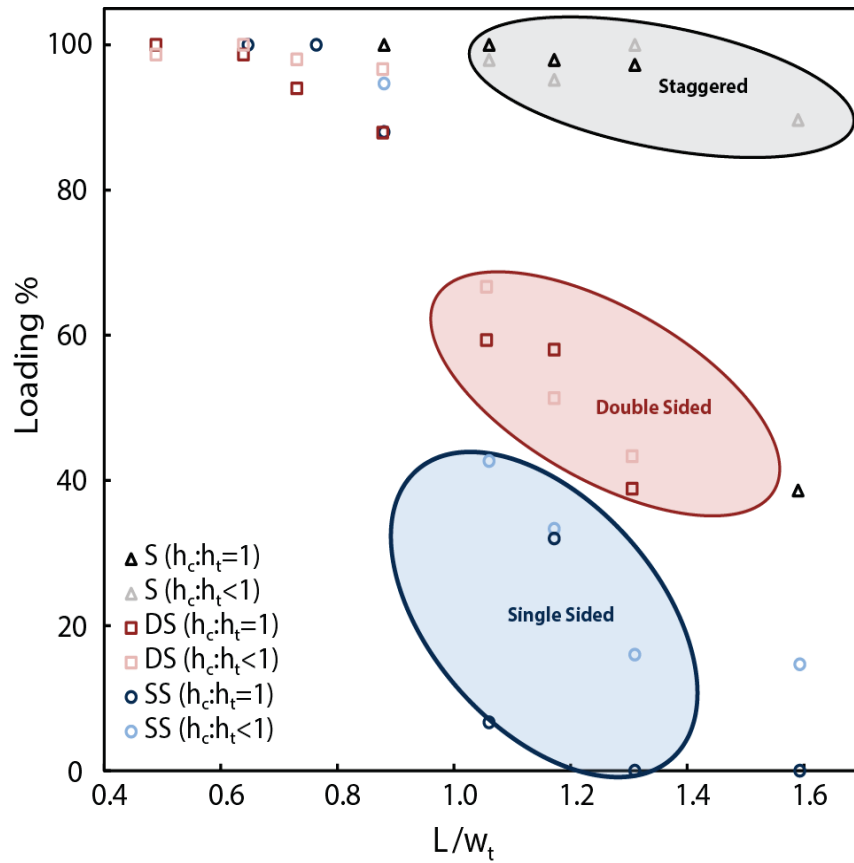


Figure 4.6: Loading % of the different trap configurations at different aspect ratios. Two data sets (light and dark) for each trap configuration represent a difference in heights between the main channel and the trap.

double-sided designs, with filling ratios approach $FR = 2$ readily achieved with the staggered design. From another perspective, the use of staggered traps can enhance the filling reliability for lower aspect ratio devices, enabling highly reliable filling for large numbers of traps.

4.3.5 Model Validation

To validate the model for each trap configuration, 35 different devices with varying trap configurations, channel width ratios, and pinning offset ratios were fabricated and characterized to evaluate trap filling reliability. For each trial a test solution of DI water, glycerol, blue food coloring, and a small concentration of surfactant was used, resulting in a measured advancing contact angle between 85° and 90° . For all devices, a constant channel width of $w_c = 200 \mu\text{m}$ and trap width of $w_t = 390 \mu\text{m}$ were employed. Additionally, the main channel height (h_c) to trap depth (h_t) were varied to investigate whether these parameters impact filling for the various designs. The number of trap elements per chip was between 15 and 30, allowing filling reliability to be quantified for each experiment. Each chip was loaded with $2 \mu\text{L}$ of test solution and the examined under a microscope to determine the fraction of traps that were completely filled with sample. Results were recorded for 5 trials per device, providing at least 75 individual trapping events used to calculate the average result for each design. The experimental results (Appendix 6a) for each configuration and aspect ratio are presented in Figure 4.6. Trap filling performance for the single-sided and double-sided designs follows the predicted trend, with reliable filling occurring only at low trap aspect ratios. For comparison,

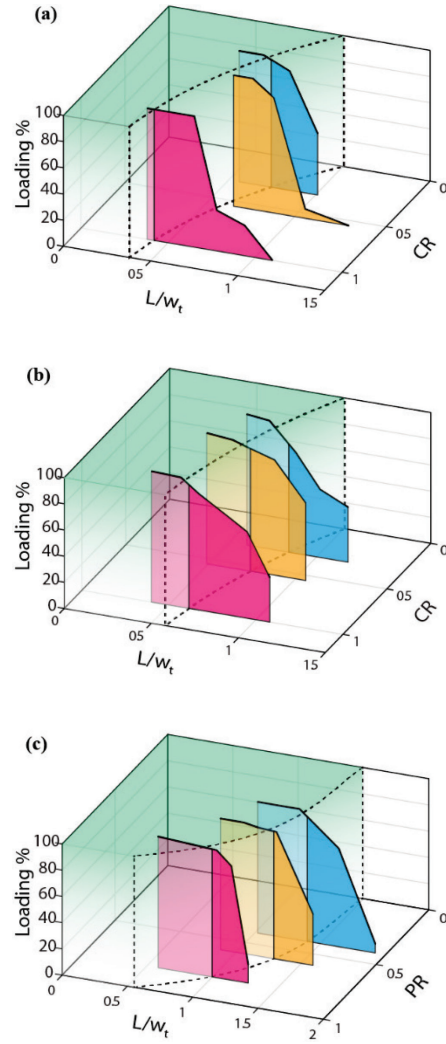


Figure 4.7: (a) Single-sided, (b) Double-sided, (c) Staggered. The model trap aspect ratio threshold is denoted by a black dashed line with the area shaded in green representing the parametric combinations the model predicts will have a high loading percentage. Data points for each parametric combination are plotted and connected by a solid black line and its shadow is color coded for each respective parametric combination. The data points that lie beyond the model threshold are shaded with a darker color and correspondingly show a sharp drop-off in loading percentage while the more transparent shadow represents data that falls in the region of expected high loading percentage.

the models predict complete filling to occur only below L/w_t thresholds of 0.60 and 0.75 for single-sided and double-sided designs, respectively. In contrast, the staggered trap model predicts complete filling for trap aspect ratios up to a threshold value of 1.3 for the given device design ($FR=0.51$, $PR=0.59$). Ideal filling (97% of traps completely filled) is observed in the experimental data up to an aspect ratio of 1.31 confirming this model prediction.

An additional study was performed using 15 devices each of the single-sided, double-sided, and staggered trap designs to assess loading reliability over a wider range of design parameters (Appendix 6b). As shown in Figures 4.7a and 4.7b, the channel width ratio and trap aspect ratio were varied by increasing both the w_c and w_t for both single-sided and double-sided models. Similarly, Figure 4.7c presents measured loading reliability for the staggered trap design, but with a fixed channel width ratio of 0.51 and varying pinning offset ratio. The dotted lines in each figure represent the model results, with 100% reliability predicted for trap aspect ratios below a critical threshold determined from the model, and 0% reliability at higher trap aspect ratios. The experimental results show excellent agreement with the geometric models, with reliable filling at L/w_t values below the predicted thresholds. Rapidly degradation of filling reliability is observed as the trap aspect ratio increases beyond this threshold for all designs. Significantly, the staggered configuration maintains high loading percentages at trap aspect ratios well above unity as the pinning offset ratio is increased.

4.3.5 High Density Staggered Trap Array

To demonstrate scalability of the staggered trap concept, a device containing an array of 768 traps was fabricated with 6 parallel rows of loading channels each connected to 128 independent traps (Figure 4.8a). The device was fabricated with a CR = 1.1 and was designed to hold 11 nL of sample within each trap, or approximately 14 μL for the full array. To load the device, 2.1 μL of sample solution was introduced into each channel inlet by pipette, automatically loading all 128 traps in approximately 1.5 min. In each row, one additional trap was

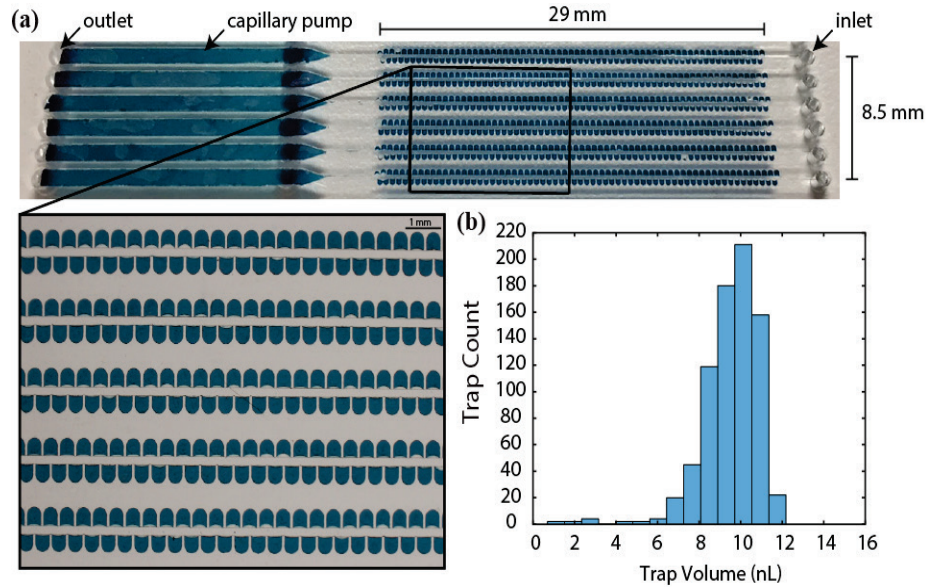


Figure 4.8: (a) Image taken of high density array of 768 traps loaded with sample and backfilled with oil. (b) Histogram of volume distribution in loaded SLD device.

included as a sacrificial element to define a pinning point for the last trap in the array. For sample filling, a downstream hydrophilic membrane capillary pump integrated into the chip served to pull fluid through the system to remove sample from the main channels. Following sample introduction, oil was next applied to each inlet to backfill the channels by capillary action, thereby isolating each trap volume and preventing evaporation of the aqueous fluid. Filling of the trap array

was found to be highly repeatable, with an average of 99.6% filling achieved. An image showing a magnified view of the filled array is presented in Figure 8b. To quantify variance in the final filling volume, a MATLAB script (see Appendix 7) was written to automatically acquire fluid area measurements from each trap based on pixel count. Using this script, a histogram of trap volume distribution was constructed (Figure 4.8c) and used to calculate a standard deviation of 1.36 nL, or 12% RSD, for the final trap volume.

4.4 Conclusion

Using a geometric model describing fluid filling in an array of staggered microfluidic traps, selective pinning of the advancing fluid front by sequential trap elements was shown to enable efficient discretization of sample into traps with length:width aspect ratios above unity. The impact of contact angle and trap geometry on filling length was explored analytically, and reliability of the filling process was investigated experimentally using 46 different design variations selected to demonstrate the value of the model as a predictive tool across a broad design space. Passive self-loading and discretization was successfully demonstrated in a thermoplastic microfluidic device, and scaled up to a high density trap array capable of highly repeatable sample loading and digitization. By taking advantage of surface tension during sample discretization, the need for oil initialization prior to sample introduction was eliminated, and chip operation without the need for pressure-driven flow or other external actuation was enabled. Because the discretization platform offers a simplified workflow, flexible trap design, reliable discretization, and repeatable operation using low-cost

thermoplastic substrates, the technology may be of particular interest for use in disposable point-of-care diagnostic applications.

Chapter 5: A self-loading microfluidic platform enabling multiplexed PCR with integrated reagents

5.1 Introduction

PCR is a sensitive diagnostic tool for nucleic acid detection and has been widely employed for genetic expression profiling of genes,^{33,34} genotyping,^{35,36} epigenetics,³⁷ forensic analysis,^{38,39} and clinical diagnostics of viral and bacterial pathogens.^{40,41} Recently, there has been a demand for conducting many PCR reactions simultaneously using one clinical sample to provide the high degree of multiplexing required for antibiotic resistance profiling, and comprehensive diagnostic panels.¹³⁹

The conventional method for performing multiplex PCR (mPCR) is to load multiple primers for the amplification of multiple target templates in one reaction. However, complexity of primer design and validation for mPCR remains a significant limitation for new assay development. More fundamentally, primer competition and spectral overlap of fluorescent probes used in real-time PCR (qPCR) limits the number of multiplexing, with 5-plex assays representing the nominal maximum that may be detected in a single reaction.⁵⁸ To overcome these constraints, multiplexing may be achieved by performing multiple individual PCR reactions simultaneously in spatially-isolated reaction wells. While a number of commercially available benchtop platforms supporting well plate based mPCR have been developed,^{59–61} they are burdened by automation equipment, costly consumables, and slow assay times, prohibiting their use in point of care settings.

Several microfluidic technologies have been explored for simplifying the automation of sample segregation so as to make mPCR practical in point of care diagnostics. For instance, droplet microfluidics has been used to generate huge arrays of individual droplet PCR reactors isolated by an immiscible phase.^{62–65} Furthermore, recent demonstrations in automated combination of sample with different reagents through droplet merging functions,^{66–68} validates its application to mPCR. Yet, this approach is still fundamentally tied to flow control hardware that is needed to form and manipulate droplets, and therefore does not serve to reduce the complexity and instrumentation requirements found in existing benchtop systems. On the other hand, passive means of segregating individually addressable reaction volumes by discontinuous dewetting,^{69,70} or geometry induced fluid shearing,^{71–73,91} simplifies automation and reduces equipment burdens. Passive approaches are particularly suited for mPCR as reaction volumes are spatially defined allowing for simple recombination with spatially defined reagents. Ideally, the process of segregating sample volumes and recombining with different integrated reagents should be equipment free so as to reduce platform footprint and cost. Along these lines, the SlipChip device recombined isolated primer sets on one substrate into individual reaction chambers on the other with a manual slipping motion to perform multiplex PCR.¹⁴⁰

Here we report a low cost microfluidic platform designed to perform highly scalable multiplexed PCR with minimal manual input. Each thermoplastic chip contains an array of interconnected microwells that serve to isolate discrete sample volumes, while PCR reagents integrated into the chip during fabrication allow for

different reactions to be performed within each discretized volume. Reagents are integrated by spotting sequence-specific PCR primers in a paraffin wax matrix, ensuring that the primers remain encapsulated during sample introduction while enabling temperature-controlled release prior to thermocycling. The sample itself is manually deposited by pipette into an inlet reservoir, with passive filling and discretization of the entire microwell array achieved by capillary pumping. Effective self-filling of the thermoplastic reaction chambers is achieved through the use of a staggered array design that employs geometric fluid pinning to promote highly repeatable filling of the high aspect ratio microwells. To explore the potential of the microfluidic platform for multiplexed PCR reactions without unwanted crosstalk between different microwells, a 2-plex assay is demonstrated in a chip containing 16 microwells using pUC19 and pBR322 plasmids presenting the selected target sequences.

5.2 Materials and Methods

5.2.1 Pin Spotting

A custom pin spotting tool was developed for the controlled deposition of PCR reagents onto COP films (Appendix 8). The tool consisted of three linear actuators (MX45S, Parker Hannifin Corp., Cleveland, OH) attached to stepper motors (LV141-02-10, Parker Hannifin Corp., Cleveland, OH) for X,Y, and Z axis control. Photoelectric sensors with 30 μm repeatability (PMY44P, Parker Hannifin Corp., Cleveland, OH) were used to calibrate the origin and provide limit stops to protect the actuators from damage. The motors were driven by a motor driver (ED-

Drive, Parker Hannifin Corp., Cleveland, OH) enabling positioning resolution of 1 μm , and controlled using an Arduino Uno microcontroller (Adafruit, New York, NY) and GRBL open source software for the graphical interface. The Z-axis actuator controlled the height of various sized pins (Xtend Microarray Pin, LabNext, Inc., West New York, NJ) that deposited nanoliter scale volumes through contact printing. The spotting stage was equipped with mechanical alignment pins for gross positioning of the channel layer to the spotter. The stage was also equipped with a two Peltier heaters; one positioned under the spotting film, and one in a peripheral location to heat the wax bath.

5.2.2 Chip Fabrication

The channel layer of the self-loading and digitizing (SLD) chip was fabricated by milling channel and microwell features in a 2 mm thick COP plaque (Zeonor 1020, Zeon Chemicals, Louisville, KY) to a depth of 250 μm using a 3-axis computer numerical controlled (CNC) machine (MDX-650, Roland DGA, Irvine, CA). A 125 μm thick hydrophilically modified polyvinylidene fluoride (PVDF) membrane with 5 μm pore size (SVLP04700, EMD Millipore, New Bedford, MA) was patterned using an automated craft cutter (Cameo Digital Craft Cutting Tool, Silhouette America, Orem, UT).

The capping layer of the SLD chip was patterned from a 50 μm thick COC film (Zeonex 1420, Zeon Chemicals). The COC film was affixed to the pin spotting stage with tape to prevent movement. Polyethylene glycol (PEG) 20kDa (81300, Sigma-Aldrich, St. Louis, MO) was added at 20% (w/w) concentration to a solution of water and primer and loaded into the pin using capillary action. Coordinates for

each trap position were programmed and upon pin contact with COP film a spot of PEG/primer solution was deposited. After deposition the PEG/primer spots were left to completely dry at 45 °C for 15 min before a protective layer of soft paraffin wax (Vaseline, Unilever, USA) was deposited over top of the dried PEG spots at a temperature 42 °C.

The microchannel substrate was next exposed to 35% (w/w) decalin (ThermoFisher Scientific, Rockford, IL) in ethanol for 1.5 min, rinsed with 100% ethanol, and blown dry with N₂. Two identically patterned PVDF membranes were stacked for a total thickness of 250 µm and inserted into a mating chamber in the COP substrate. The decalin-solvated channel substrate and capping layer were then aligned using pins built into an alignment stage and mated to seal the channels and microwells. The chip assembly was then placed in a hot press (AutoFour/15, Carver Inc., Wabash, IN) at 200 psi and 23 °C for 10 min to complete the bonding.

5.2.3 Multiplexed Assay

p19 forward primer (5'-GACCTACACCGAACTGAGATACC-3') and reverse primer (5'-TCCGACCCTGCCGCTTAC-3') as well as p322 forward primer (5'-TGCTCAACGGCCTCAACCTA-3') and reverse primer (5'-AGTCATAAGTGCGGCGACGA-3') were designed using Primer3Plus software and ordered from Invitrogen (Carlsbad, CA). The primer printing solution contained 10X 5 mM primer stock, 2X buffer (Novella Oligo Dilution Buffer, Canon US Life Sciences, Rockville, MD) and 3X 50% PEG solution, to achieve a final primer concentration of 500 µM in each trap reaction volume.

pUC19 and pBR322 plasmids were purchased from New England BioLabs (Ipswich, MA) and diluted to 30 ng/ μ L in water. Each template dilution was mixed with equal volumes of commercial master mix (Novallele Genotyping Assay, Canon US Life Sciences, Rockville, MD) and EDTA buffer (Sigma-Aldrich, St. Louis, MO) to form the sample solution with a final concentration of 10 ng/ μ L, or approximately 1.0 ng per trap reaction.

5.2.4 Chip Operation

Chip loading was performed by pipetting 3.75 μ L of sample solution in the inlet of the device. Excess samples was removed by the integrated PVDF membrane downstream and then 5 μ L silicone oil (AR20, Sigma-Aldrich, St. Louis, MO) with 0.5% (w/w) ABIL EM90 surfactant (ABIL EM90, Evonik Industries) was loaded into the device fully isolate each reaction chamber. Once loaded, a single piece of PCR-compatible adhesive tape (LC480 Sealing Foil, Roche Diagnostics Corp., Indianapolis, IN) was used to seal the top side of the chip. The chip was then placed on a custom thermocycler comprising of a Peltier element controlled by an Arduino microcontroller. The software-defined PCR routine implemented by the microcontroller consisted of a 120 s hot start at 95 °C, followed by 20 cycles of 95 °C for 15 s, 60 °C and 72 °C for 30 s. The microcontroller actuated the 452 nm LED light source and collecting fluorescence output during the extension step (72°C) with a CCD camera placed directly above the chip.

5.3 Results and Discussions

5.3.1 Chip Design and Fabrication

The basic self-loading and digitizing device (Figure 1) consists of a channel connecting an inlet to a capillary pump at the outlet with staggered traps in between. Microwell dimensions of 900 μm square and 250 μm deep were chosen to accommodate the paraffin wax covered reagents and provide sufficient reaction volume for effective PCR from dilute samples.

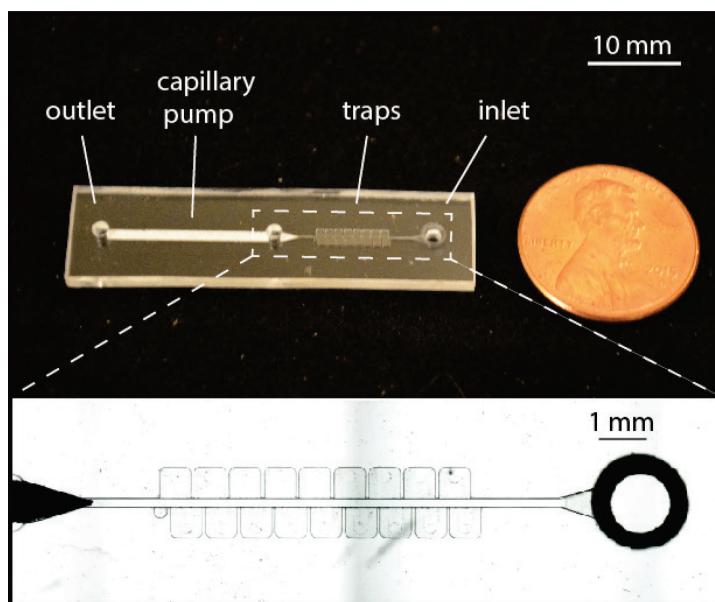


Figure 5.1: Image of the self-loading and digitizing chip.

The self-loading and digitizing device was fabricated from COP due to its high transparency, low autofluorescence, low water absorption, and low gas permeability. Channel features were milled directly in the substrate by CNC milling. The channel layer was also milled with alignment holes in each corner so that it could be aligned to protruding pins on the pin spotting stage that would keep it aligned with the same origin on the pin spotter each time. Two PVDF membranes were patterned using a craft cutter and were then inserted into a pre-milled chamber

on the channel layer. It was found that cutting a pointed shape at the front of membrane provided the best performance in terms of purging excess sample from the main channel. The milled substrate was then mated to the thin film COP with deposited reagents face down on the spotting stage. The entire fabrication process is summarized in Figure 5.2.

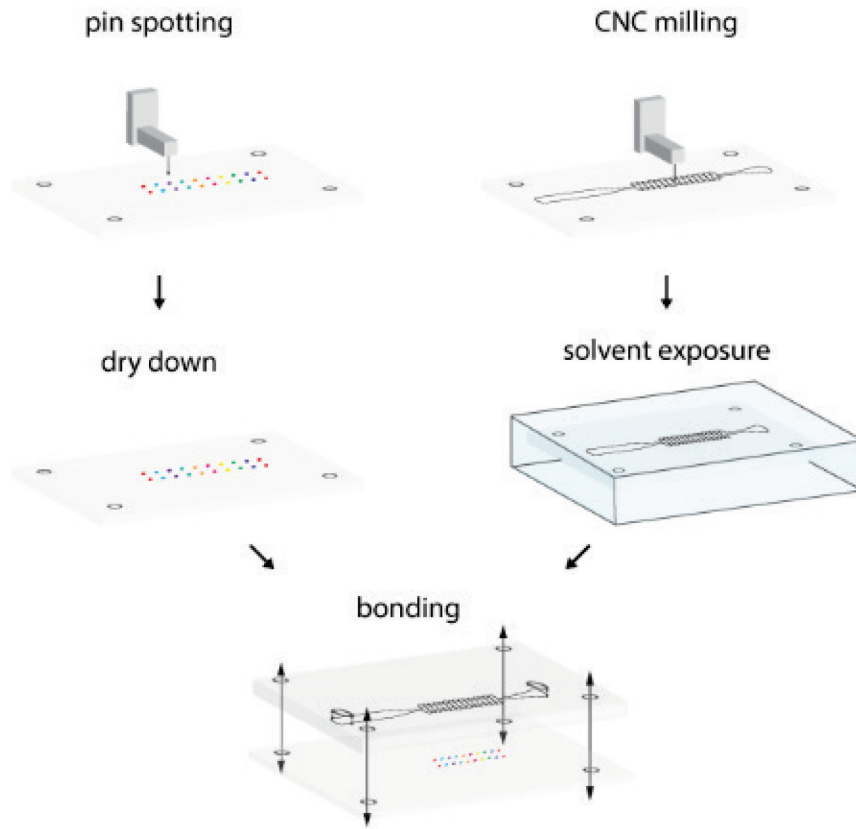


Figure 5.2: Fabrication process for the SLD platform. Pin spotting and CNC milling can be done in parallel and each substrate is then bonded using alignment pins.

5.3.2 Pin Spotting

Preventing the rehydration of integrated primers during sample introduction is essential to the proper functioning of the SLD platform. Without slowing rehydration primers will be carried by the fluid front and transported downstream

cross contaminating subsequent traps. Polysaccharides have commonly been used as matrices for controlled drug release, as well as controlled release of dried reagents in porous microfluidic devices¹⁴¹, and therefore were selected for a dissolution retarding matrix for the integrated primers.

Sucrose, dextran, and polyethylene glycol were selected for their solubility in water, and general biocompatibility with polymerase chain reaction. Each was dissolved at concentrations ranging 10-40% (w/w) and mixed with fluorescein salt. A concentration of 20% (w/w) for each polymer was found to successfully balance viscosity appropriate for deposition and dissolution time. The different mixtures were spotted on the COP substrate and dried down. A droplet of water with a comparatively large volume was added to the spot and fluorescence was recorded over time. In this way the approximate dissolution time (diffusion limited) for each additive was determined. Likewise sucrose, dextran, and PEG spots were

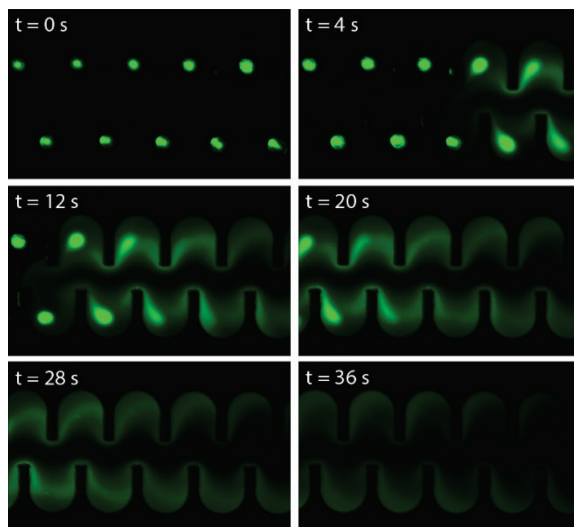


Figure 5.3: Image sequence of PEG and fluorescein salt being rehydrated by sample self-loading in the SLD chip. Approximate dissolution time was calculated when the initial bright spot was dispersed and could no longer be distinguished in trap.

incorporated into an SLD device and then self-loaded with sample solution to confirm the effect of advective flow in the traps. Fluorescence in the traps was recorded over time to determine the approximate dissolution time with the addition of advection. Figure 3 shows fluorescence over time from PEG 20% (w/w) and fluorescein salt spots as solution is self-loading through the device. While increasing polymer chain length did show improvement it was not to an acceptable level for retaining a sufficient amount of primer without contaminating downstream wells in the time it would take to load the chip. In another approach gelatin was tested to retain primers to the trap during loading. Gelatin improved diffusion limited transport and could fully expel the incorporated dye when heated above its melting point, however during device testing once the gel was hydrated advection would dominate dissolution and disperse the fluorescein salt at a similar time scale to sucrose and PEG. To mitigate the effects of advection, paraffin wax, a hydrophobic material containing hydrocarbons of the general formula C_nH_{2n+2} , was explored. Paraffin wax has been shown to be both compatible with PCR and able to protect dried reagents against flow,¹⁴² however controlled deposition of protective paraffin films in μm -scale dimensions has to our knowledge not yet been demonstrated. A robust coating of paraffin overtop of a primer spot was able to provide an indefinite protective barrier to primer dissolution. The paraffin could be heated to above its melting point after sample solution was loaded to disperse the primers into its reaction chamber. Table 5.1 summarizes the spotting and dissolution data for the mentioned additives.

Table 5.1: Summary of primer additive materials for reagent integration

MATERIAL	SPOTTING VARIABILITY	CONTROLLED RELEASE	DISSOLUTION TIME (DIFFUSION)	DISSOLUTION TIME (DIFFUSION + ADVECTION)
Sucrose (20%) (MW = 310 Da)	$\sigma = 5.9\%$	No	20 s	2 s
PEG (20%) (MW = 20,000 Da)	$\sigma = 1.8\%$	No	60 s	8 s
Dextran (20%) (MW = 70,000 Da)	$\sigma = 14.3\%$	No	90 s	*N/A
Gelatin (300 bloom)	$\sigma = 2.0\%$	**Yes (T > 60C)	200+ s	5 s
Paraffin Wax	$\sigma = 2.5\%$	Yes (T > 60C)	Indefinite	Indefinite

Note: *denotes that test was not attempted because spotting was too inconsistent

**denotes that controlled release was in the diffusion limited case only

5.3.3 Pin Spotting Tool Optimization

Temperature control was an integral factor in successfully spotting the paraffin wax. It was found that a sufficiently thick layer of paraffin (>30 μms) was required to completely protect the primers during flow. To achieve this thickness the temperature had to be kept above the paraffin melting temperature of 37 °C, but less than 50 °C where the paraffin would easily wet out on the surface of the COP. If the wax wet the surface too easily it would spread outside the bounds of the trap

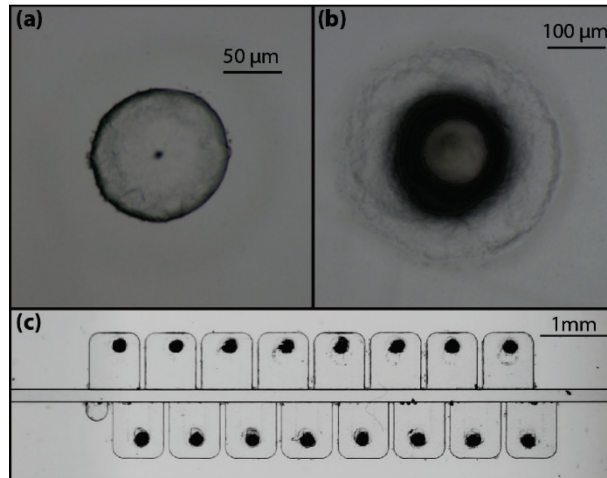


Figure 5.4: (a) Image of a dried down PEG/primer spot. (b) Image of a PEG/primer spot covered by a paraffin wax capping layer. (c) Image of primer spots capped with paraffin in the device chip.

and compromise the bonding surface. Temperature control through convective heating of the environment around the tool proved to be difficult because no direct measurements of the pin temperature could be made. The pin has to be completely free floating or damage can occur during contact with the stage. Because of the lack of temperature control, relying on the pin capillary to draw in wax, maintain the optimal temperature, and dispense it upon contact with the substrate produced poor results. The more successful approach was a “*pick and place*” technique where a solid pin would be dipped in a hot wax bath ($T = 100\text{ }^{\circ}\text{C}$) and when retracted would retain a dollop of wax slightly larger than the pins outer diameter. The pin would then make contact with the substrate held at $42\text{ }^{\circ}\text{C}$ by an integrated Peltier element in the stage, and the wax would melt with a viscosity that resulted in a sufficiently thick mound covering the primer spot.

5.3.4 Reagent Integration and Controlled Release

Polyethylene glycol (PEG) was included as an additive to the primer solution at a concentration of 20% (w/w). The PEG served to improve the long term stability of the dried down oligomers as well as increase the viscosity of the spotting solution, reducing spot variability. Additionally, when dried down the PEG additive crystallized into a solid which served as a way of visualizing the primers so that proper alignment with the subsequent wax deposition could be easily characterized. Using a $300\text{ }\mu\text{m}$ diameter pin tip PEG 20% (w/w) mixed with primer resulted in a nominal spot size of $113.5\text{ }\mu\text{m}$ ($\sigma = 2.1\text{ }\mu\text{m}$) (Fig 4a). The spot had a contact angle of 45° with the COP film resulting in an estimated deposited volume of approximately 0.2 nL.

Paraffin wax was used as a capping layer for the PEG/primer spot. Using a 200 μm diameter pin resulted in a nominal paraffin wax spot size of 249.4 μm ($\sigma = 6.3 \mu\text{m}$) (Figure 5.4b). Paraffin capped primers were spotted into the upper center of the traps because that was the center of the reaction volume that was captured during loading (Figure 5.4c). The paraffin provided a robust protective layer overtop the primers preventing rehydration during several repeated flushes with Methanol, Isopropanol and DI water through the device. To demonstrate controlled release of the incorporated primers fluorescein salt was added to the primer solution. The chip was loaded and backfilled with oil with no measureable difference in the fluorescence of the spots. Images were then taken as the chip was heated up to 70 $^{\circ}\text{C}$ (Figure 5.5) showing the fluorescence dispersing from the original spots as the temperature reaches $\sim 65^{\circ}\text{C}$. To confirm that the paraffin would not inhibit the PCR reaction it was added to the multiplex assay and tested against a reaction mixture without paraffin. It was found to have no effect on the efficiency of the reaction based on the comparison of the respective C_t values.

5.3.5 Loading Performance

Proper self-loading of the device relies on the surface interactions of the sample solution and the chip substrate. A model of surface tension driven staggered trap loading is presented in (Chapter 4). In order to integrate PCR reagents, a paraffin wax is deposited on the surface of the traps resulting in a deviation in loading percentage from the previously described model because of the added hydrophobicity. Initially, the SLD chip trap depth was 100 μm to provide better sample retention in the traps during the capillary pump induced purging. However,

after incorporating the paraffin spots, aqueous sample solution would circumvent the hydrophobic wax surface and leave behind an air bubble in the traps over the paraffin mounds. To overcome this the depth of the channels was increased such that a lesser pressure change would be required to overcome the hydrophobic wax

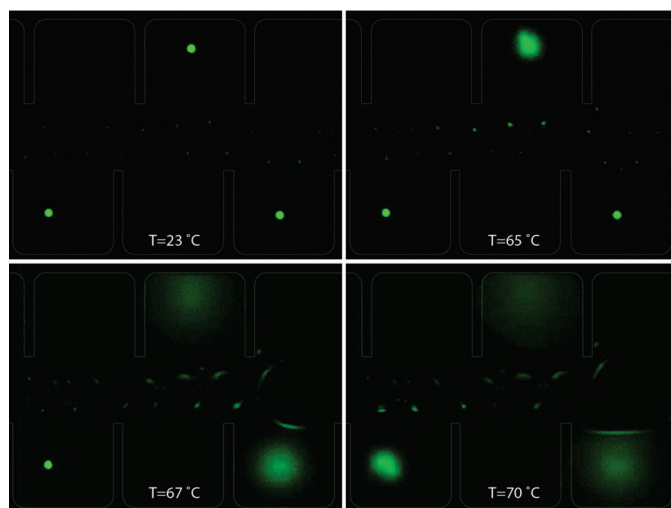


Figure 5.5: Image sequence showing temperature controlled release of fluorescein salt mixed with primer and PEG printing solution. After loading sample solution the chip was heated up to 70 °C showing original fluorescent spots dispersing throughout the wells.

mound. Trap depth had to be limited however because self-loading and sheer induced separation during purging would be negatively impacted by increasing the characteristic length of the system (depth). Ultimately a trap depth of 250 μm was found to be the optimum for reliable bubble free loading while also providing sufficient sample retention during purging. Initial loading experiments with the given trap dimensions of 900 μm (wide) x 900 μm (long) x 250 μm (deep) resulted in a mean captured volume of 92 nL (RSD = 9.2%). Digitized volume was extrapolated by using image analysis to measure the surface area of the captured sample and multiplying it by the depth of the trap.

5.3.6 Multiplex PCR

The ability to detect different template DNA based on the specific integrated primer sets was important in proving the utility of the platform for potential use in bacterial species identification and antibiotic resistance screening. Primer sets were designed to demonstrate two scenarios: 1) primer sets compatible with template would amplify while non-compatible primers would not, 2) if both primer sets would amplify with the loaded template then their respective melt temperatures (T_m) could be distinguished during an on-chip HRMA. To accomplish the first scenario we designed a primer set p19 that would amplify pUC19 template and a primer set (p322) that would not. For the second scenario we insured that p19 would also amplify with pBR322 template so when loading pBR322 template both p19 and p322 primer sets would be amplified, but yield amplicons with differing melt temperatures. Figure 5.6a shows an illustration summarizing the expected experimental outcomes. Both primer sets were designed to amplify under the same thermocycling conditions - 20 cycles of 95 °C for 15 s, 60 °C and 72 °C for 30 s. The assay was run on a Roche LC480 beforehand and HRMA confirmed that the p19 primers and pBR322 template reaction yielded amplicons that had a T_m of - 2.3°C relative to amplicons produced by p322 primers and pBR322 template.

The platform was designed to minimize workflow such that only two pipetting steps is all that is required to discretize a sample into 10s – 100s of reactions. This was realized experimentally with a 16 trap device was loaded in less than 60 s. We achieved a trap loading percentage of 75% and 100% for pUC19 template and pBR322 template loaded chips respectively. The pUC19 loaded chip

failed to load two traps filled with p19 and two traps filled with p322 due to air bubbles formed upon initial sample loading, which expanded during thermocycling and expelled the reaction volume into the main channel.

After loading the integrated primer mix was released from its wax coating during the PCR routine during the “hot start” phase when the device was heated to 95 °C. Traps loaded with p19 primers amplified as expected with a mean $C_t = 10.38$ ($\sigma = 0.55$), while traps loaded with the p322 template did not produce any discernable amplicons. HRMA showed that the traps filled with p19 produced an amplicon with a mean $T_m = 86.4$ °C ($\sigma = 0.3$ °C).

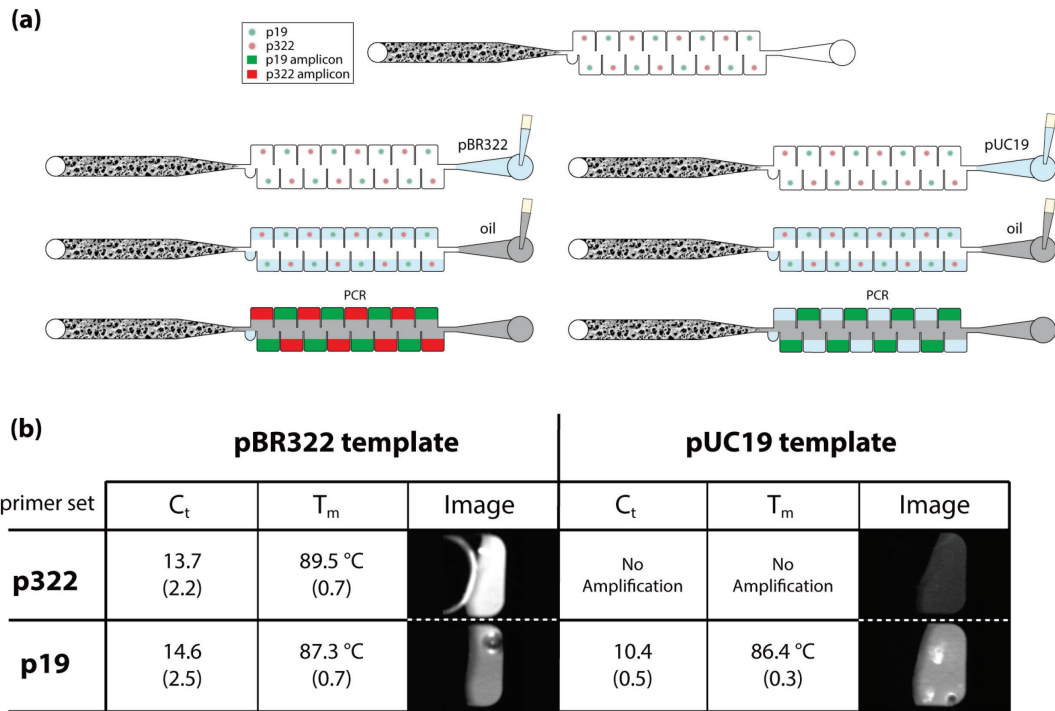


Figure 5.6: (a) Experimental design of the two step multiplex assay that was tested on the platform. (b) Table of experimental results with pUC19 template and pBR322 template loaded chips.

The chip loaded with pBR322 template loaded all traps successfully. Traps filled with the p19 primers amplified a product with a mean $T_m = 87.3$ °C ($\sigma = 0.7$ °C), and traps filled with p322 primers produced an amplicon with a mean $T_m =$

89.5 °C ($\sigma = 0.7$ °C). A ΔT_m of 2.2°C between p19/pBR322 and p322/pBR322 amplicons is in good agreement with the ΔT_m measured on the LC480. It is worth noting that two traps loaded with p19 and three traps loaded with p322 primers did not amplify even though reaction volumes remained in the traps during operation. One explanation for no amplification is that the wax layer was deposited too thinly over the primer spot which led to the primers getting washed out during sample loading. A future more comprehensive study of factors affecting wax layer quality, or ways to characterize wax quality without altering the chip, would help mitigate this issue.

5.4 Conclusion

This work demonstrates a self-loading and digitizing platform for performing multiple discrete PCR reactions requiring only a pipette for sample loading. A new strategy for pre-depositing primer sets and protecting those primer sets from rehydration during sample loading was explored using a custom designed pin spotting instrument. Several different matrices were optimized for slowing primer rehydration. Ultimately, paraffin proved to not only be the most robust in protecting the underlying primers, but primers could also be released from the protective layer by melting. Deposition of the PEG/primer solution and the paraffin wax was optimized to achieve consistent spotting, 113.5 μm ($\sigma = 2.1$ μm), and 249.4 μm ($\sigma = 6.3$ μm) mean spot sizes respectively. Taking advantage of the unique capability a multiplex assay was designed with two primer sets that amplified with the pUC19 and pBR322 plasmid vectors. When pUC19 template was loaded into the chip only p19 loaded traps amplified and produced the correct amplicon with a

$T_m = 86.4\text{ }^{\circ}\text{C}$ ($\sigma = 0.3\text{ }^{\circ}\text{C}$). When pBR322 template was loaded into the chip both p19 and p322 loaded traps showed amplification. HRMA was used to confirm that p19 amplicons had a $T_m = 87.3\text{ }^{\circ}\text{C}$ ($\sigma = 0.7\text{ }^{\circ}\text{C}$) and p322 amplicons had a $T_m = 89.5\text{ }^{\circ}\text{C}$ ($\sigma = 0.7\text{ }^{\circ}\text{C}$), a ΔT_m in good agreement with prior assay characterization using an LC480. The SLD platform's unique capability for integrating highly scalable multiplexed assays coupled with simple and instrument free workflow provides great potential for point-of-care diagnostics, particularly for bacterial species identification and resistance screening.

Chapter 6: Conclusion

6.1 Summary

The last 20 years microfluidic technology development has set the stage for a paradigm shift in medical diagnostics by enabling sample volume reduction, low reagent consumption, rapid analysis times, portability, multiplexed analysis, and assay automation. Yet, extracting value from these capabilities requires careful consideration of important practical criteria for device operation (Table 5.1). In this dissertation a suite of technologies for conducting multiplexed nucleic acid analysis were explored with a focus on ASSURED criteria to realize a microfluidic PCR platform that has the potential to advance practical POC diagnostics. In using PCR compatible thermoplastics with sufficient thermal performance, integrated heating elements, and PID control, it was demonstrated that rapid and efficient PCR could be performed on a relatively simple and low cost platform. These thermoplastics also possess favorable surface properties for self-loading operation, and when coupled with a novel sample discretizing trap technique, multiplexing was achieved with a significant reduction in supporting equipment usually required for such operation like, syringe pumps, centrifugal systems, valving, and interfacing. Integrated reagents also simplified workflow and reduced overall consumable requirements and cost. A multiplexed PCR device utilizing the presented technologies will more closely adhere to the ASSURED criteria than current strategies, and thus be better positioned to better address future healthcare challenges.

Table 6.1: Summary of ASSURED criteria with target specifications for POC HIV diagnosis outlined by Wu et al.¹, and specifications reached by the platform presented in this work. Although, target specifications were specific to HIV diagnosis they are applicable to this platform at the system level.

Criteria	Target Specifications ¹	This Platform
Affordable	< \$500 per machine, < \$10 per test	~US\$ 500 per machine, ~\$4 per chip
User-friendly	1–2 days of training, easy to use	simple pipet training, automated PCR and HRMA
Rapid and Robust	< 30 minutes for diagnosis, minimal consumables (i.e. pipettes, reagents, etc.), high throughput	15 min for diagnosis, integrated reagents, requires only pipette/oil/PCR adhesive film, high throughput (768-plex potential)
Equipment –free	compact, battery powered, on-site data analysis, easy disposal, easy sample handling, no cold chain	small footprint, low power operation/battery powered, data analysis algorithm, disposable

6.2 Contributions to the Field

This worked aimed at demonstrating a multiplex PCR platform under the ASSURED criteria resulted in several significant contributions to the field of microfluidics, which will be summarized below by section.

6.2.1 Rapid PCR in Low Conductivity Thermoplastics

A fabrication process for high resolution embossing and bonding thin film microfluidic substrates to minimize their thermal mass was developed (Figure 2.2). In addition, a process for deposition of gold heating and sensing elements on the backside of a microfluidic device without compromising their thermal performance was developed (Figure 2.2). Realizing rapid thermocycling times on a thermoplastic platform, an achievement that has come with added complexity and costs in other approaches,^{84,85,93} required significant thermal modeling and design optimization in addition to process development. COMSOL multiphysics software

was used to build a comprehensive simulation incorporating heat transfer physics and PID control. Dimensions of the bottom COP film thickness and reaction chamber depth were varied over ranges that were selected based on material and fabrication process constraints. From these results (Figure 2.5a,b), a direct correlation between each geometric parameter and the thermal rise time is observed, suggesting that smaller sealing layer thickness and chamber depth are desired. The model was also used to compare cycle times under open-loop and closed-loop control (Figure 2.5c). For closed-loop control, the input voltage was modulated using a PID control algorithm and temperature feedback from the sensor element. Proportional, integral, and derivative controller constants were varied to optimize cycling speed and control authority at each step. Optimized parameters were incorporated into the final systems and validated experimentally with a sub-14 second cycle time (Figure 2.6). Furthermore, amplification of a mutant G6PC gene sequence from hgDNA indicative of Von Gierke's disease was successfully performed under a variety of PCR conditions, with on-chip HRMA proving to be robust for identifying PCR product melting temperature within 0.6% of the known value for G6PC. Overall, this work reported key parameters for achieving high thermal performance on thermoplastic substrates using a simple integrated approach.

6.2.2 Fabrication of High Quality Expansion Valves for Stop Flow with Low Surface Tension Fluids

Fabrication high quality hydrophilic expansion valves capable of extended flow stopping using low surface tension fluids was reported in this work.

Hydrophilic capillary expansion valves have been investigated by several groups.^{111,115–117} However, their use in thermoplastic PCR chips places significant demands on the valve design due to the low surface energy of the COP surface, the low nominal surface tension of the PCR reaction mixture, and the further reduction of surface tension that occurs by heating of the mixture during amplification. To further enhance valve burst pressure for PCR operation, a fabrication process that could reproducibly generate valves with widths and depths of 60 μm and 30 μm respectively, with expansions angles of 120° was developed. When a device was loaded the fluid front would advance by capillary action through the reaction chamber and halt at the valve so as to self-meter consistent volumes (Figure 2.4). The integrity of the valve was evaluated over the course of 50 thermocycles, with no bursting of the valve observed. Compared to previous reports of large expansion angle valve designs,¹¹⁶ the demonstrated ability to maintain a long-term passive seal using low surface tension fluids is unique. This simple and robust passive valving coupled with capillary loaded serves to reduce operational error while eliminating the need for complex fluidic interfacing, valving, or pumps during the loading process.

6.2.3 Novel Staggered Trap Array for Robust Sample Discretization

A novel trap design for sample discretization in capillary loaded systems is reported. The use of selective pinning of the advancing fluid front by sequential trap elements was shown to enable efficient discretization of sample into traps with length:width aspect ratios above unity. The impact of contact angle and trap geometry on filling length was explored analytically (Figure 4.3 – 4.5), and

reliability of the filling process was investigated experimentally using 46 different design variations selected to demonstrate the value of the model as a predictive tool across a broad design space (Figure 4.7). Passive self-loading and discretization was successfully demonstrated in a thermoplastic microfluidic device, and scaled up to a high density trap array (Figure 4.8) capable of repeatable sample loading and digitization. By taking advantage of substrate surface tension during sample discretization, the need for oil initialization prior to sample introduction was eliminated, and chip operation without the need for pressure-driven flow or other external actuation was enabled. Because the discretization platform offers a simplified workflow, flexible trap design, reliable discretization, and repeatable operation using low-cost thermoplastic substrates, the technology may be of particular interest for use in multiplexed point-of-care diagnostic applications.

6.2.4 Staggered Trap Array for Multiplexed PCR with Integrated Reagents

Implementation of the staggered trap array for multiplexed PCR necessitated the integration of reagents into each trap so independent reactions could occur from one sample. A pin spotting deposition technique that allowed or high resolution spatial control over 3-axis was developed towards this end. We reported highly repeatable deposition (RSD = 1.8%) of printing solutions consisting of primers and 20% (w/w) PEG additive (Figure 5.4a). To protect the integrated reagents paraffin wax was deposited overtop of the primers using a “pick and place” strategy to produce highly repeated paraffin spots (RSD = 2.5%) with sufficient thickness (Figure 5.4b). Controlled release is also demonstrated (Figure 5.5) by

keeping spotted primers encapsulated until the paraffin melting temperature is reached. Finally, it was shown using a 2-plex PCR assay that the reagent integration process did not affect primer functionality and there was no cross contamination during sample loading (Figure 5.6b). This is the first demonstration of the deposition of pL scale volumes of different materials to form complex constructs for controlled reagent release, and with it brings the potential to reach the multiplexing levels of droplet microfluidics in a much simpler format. Moreover, the ability to integrate reagents at the manufacturing level can drastically reduce operational workflow and consumable costs. Taken together this achievement represents a significant advancement in diagnostic capability in accordance with ASSURED criteria.

6.3 Future Work

The work presented in this dissertation provides the proof-of-concept for the staggered trap multiplexed array platform. That said, there are several platform improvements and enhancements that can be made and should serve as the focus of future work.

Platform improvements in fabrication could be explored to reduce operational issues. CNC milling was used to mill the staggered trap array substrates because it was simple to incorporate precisely positioned holes for alignment with the patterned reagent films. However, direct milling left debris and flash at the bonding interface which could sometimes not be fully removed even after rigorous sonication. Flash and debris would get sandwiched between the substrates and

cause voids to form in the bonding layer between the two chips. These voids would serve as nucleation points for trapped air to expand and circulate the main channel during thermocycling. Fabricating the trap array substrate by embossing would result in a smoother surface and eliminate the ability for voids to form in the bonding layer. The 2-step embossing process outlined in Figure 2.2 already shows the merit of an embossing process as air bubbles were not observed in the rapid PCR device. Future work would involve developing a technique to pattern alignment holes during the embossing process, as well as optimizing embossing conditions to yield sharp channel features after demolding.

Trap density is also limited when using a direct milling approach because tooling under 100 μm is just too fragile for reliable use. A minimum trap volume of about 300 pL ($L=100\mu\text{m}$, $w=100\mu\text{m}$, $d=30\mu\text{m}$) is achievable using direct milling. Lithographic patterning offers the potential for much smaller minimum feature size (minimum trap volume of about of <100 pL) as well as the ability to pattern curves and angles that are just not possible with direct milling. Development of a process using SU8 photolithographic patterning to emboss the secondary mold would allow for dense arrays in addition to higher quality molds.

Higher density arrays would also require higher density reagent deposition. Reagent deposition spots can be controlled by the pin size, and pins down to 15 μm capillary diameter can be purchased commercially. However, reduction in capillary diameter requires further optimization of spotting solution components. Additives such as glycerol are used to control viscosity, leading to more consistent spots, while PEG additives were shown to work best for solidify the primer spots so that

a layer of paraffin could be deposited over top. Yet, there is a critical concentration where too much additive will result in polymer precipitates that clog the pin tip. Future work would entail optimizing the concentration of these additives for consistent spotting at this scale. Other techniques such as direct printing could also be used. Direct printing of relatively concentrated sucrose solutions has already been demonstrated by the Yager group.¹⁴¹ While printing of paraffin wax is commonly used for patterning channel features in paper microfluidics.¹⁴³ Exploration of a direct printing approach could reduce minimum deposited volume for higher density arrays, and at the same time provide a process more compatible with roll-to-roll manufacturing.

Several system level enhancements would make the multiplexed platform more impactful. A key limitation of the current platform is the lack of integrated sample preparation. Sample preparation is needed to isolate and enrich target constituent (i.e. DNA) from complex biological media (e.g. stool, sputum, blood). It is common for sample preparation to be integrated at the front end of microfluidic diagnostic platforms,^{79,90,144,145} However, due to the wide range of sample processing requirements specific to each assay, integrated sample preparation can constrain the utility of the platform and add unnecessary complexity in downstream system design. On the other hand, separating sample preparation with downstream PCR amplification and analysis results in two independent systems that are simpler and in practice do not add significantly to the overall workflow. Commercial sample preparation modules like Cepheid GeneXpert¹⁴⁶ have been proven effective for cancer and bacteria assay workflows and could be used in conjunction with the

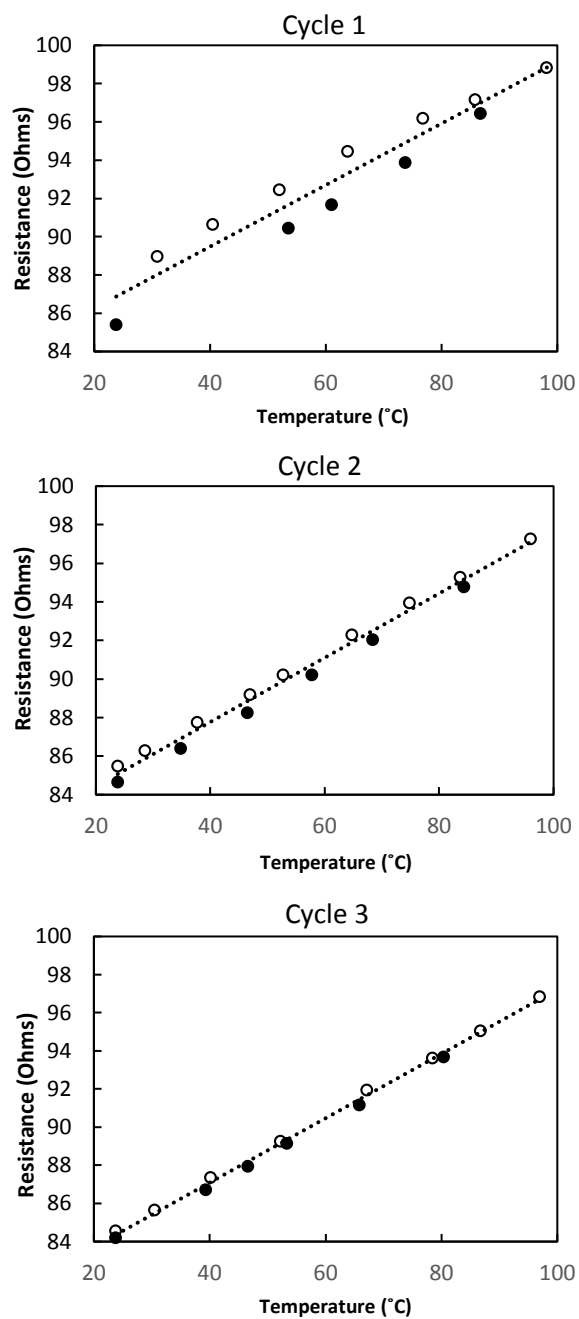
multiplex platform. Alternatively, our group has shown relatively simple fabrication and integration of porous polymer elements for DNA capture and cell lysis, two important steps in the sample preparation process.^{147,148} These capture elements could be incorporated into a pipette tip or syringe for example when extracting patient sample, and not add workflow to the downstream PCR platform. Ultimately, the sample preparation module should be developed under the same ASSURED criteria as the PCR platform.

Another potential enhancement is reduction of system footprint. The custom PCR system (Figure 2.3c) that was used to test the PCR devices was built from off-the-shelf components with little focus on footprint. Optical components (e.g. LED, camera) still prevent the system from achieving a portable size. Exploring the use of board level cameras, and custom LEDs to shrink the optical setup to a smaller size is a worthwhile direction for future work. In fact, there have already been demonstrations of commercially available board level cameras being integrated into microfluidic systems.¹⁴⁹ Focus on systems engineering could potentially shrink the system down to the size of a USB stick, as has been done by Gurralla et al. for HIV detection.¹⁵⁰

Finally, the most impactful future work could be application of the microfluidic platform to clinically relevant multiplexed assays. There are several multiplexed panels that have been cleared by the FDA for identification of pathogen strains and associated antibiotic resistance.¹³⁹ These panels could be adopted for use in the presented multiplex device by synthesizing the primers sets in high concentration and depositing them using the method outlined in Chapter 5.

Appendices

Appendix 1:



Measurements of thermistor resistance during temperature cycling between room temperature and 95 °C plots over sequential 3 cycles. Heating (hollow dots) is followed by cooling (filled dots). All chips used in this work were burned in using a minimum of 3 temperature cycles to reduce hysteresis error to below 0.5% over the full PCR temperature range.

Appendix 2:

```
#include <PID_v1.h>
#include <SPI.h>
#include "Adafruit_MAX31855.h"

//Define constant voltage thats modulated via mosFET
//Constant Voltage >= V and A where T = 95C during calibration
float V = 2.5; // @264 mA
int PWR = 5;

//Define thermocycling parameters time is in msec
int numCycles = 100;
int hotstartTime = 30000;
int denatureTime = 5000;
int annealTime = 4500;
int extensionTime = 4500;

//Initailize timers
unsigned long timeStamp = 0;
unsigned long timer = 0;

//Define parameters of chip calibration for temperature conversion
float m_M = 17.804; //slope of the calibration equation in the form of [T = m*V + b]
float b_M = 26.662; //the intercept of the calibration curve

//Define conversion factor for mismatch between sensor and reaction chamber
float m = 1.0142;
float b = -6.1781;

//Define PID variables and tuning parameters
double denatureSetpoint, annealSetpoint, extensionSetpoint, Input, Output;
double denatureKp = 20, denatureKi = 10, denatureKd = 0.5;
double annealKp = 30, annealKi = 20, annealKd = 0.5;
double extensionKp = 10, extensionKi = 5, extensionKd = 0.2;

//Specify the links and initial tuning parameters for each temperature step
PID denaturePID(&Input, &Output, &denatureSetpoint, denatureKp, denatureKi, denatureKd, DIRECT);
PID annealPID(&Input, &Output, &annealSetpoint, annealKp, annealKi, annealKd, DIRECT);
PID extensionPID(&Input, &Output, &extensionSetpoint, extensionKp, extensionKi, extensionKd, DIRECT);

//Image Capture Parameters:
int CCD = 9; //CCD trigger I/O pin 9
int LED = 11; //LED trigger I/O pin 11
int expt = 500; //CCD exposure time in milliseconds

void setup()
{
  pinMode(LED, OUTPUT); // initialize the led digital pin as an output.
  pinMode(CCD, OUTPUT); // initialize the CCD trigger digital pin as an output.
  pinMode(PWR, OUTPUT); // initialize the power PWM pins as output

  //initialize the variables we're linked to
  Input = readTemp();
  denatureSetpoint = 94;
  annealSetpoint = 66;
  extensionSetpoint = 71;

  //turn the PID on
  denaturePID.SetMode(AUTOMATIC);
  annealPID.SetMode(AUTOMATIC);
  extensionPID.SetMode(AUTOMATIC);

  //Initailize serial monitor
  Serial.begin(9600);
  Serial.println("Benchtop PCR Program");
```

```

// wait for MAX chip to stabilize
delay(500);
}

void loop()
{
  // Run all PCR cycles until done:
  for (int i = 0; i <= numCycles; i++)
  {
    Serial.println();
    Serial.print("CYCLE# ");
    Serial.println(i);
    if (i < 1) //hot start is on the first cycle
    {
      //Hot Start
      timeStamp = millis();
      while (millis() < (30000 + timeStamp))
      {
        Input = readTemp();
        denaturePID.Compute();
        analogWrite(PWR, Output);
        float CV = V * (Output / 255);
        timer = millis();
        Serial.print("HS: ");
        Serial.print(";t = ");
        Serial.print(timer);
        Serial.print(" ;T = " );
        Serial.print(Input);
        Serial.print(" ;CV = " );
        Serial.print(CV);
        Serial.println(";");
      }
      // Anneal:
      timeStamp = millis();
      while (millis() < (4500 + timeStamp))
      {
        Input = readTemp();
        annealPID.Compute();
        analogWrite(PWR, Output);
        float CV = V * (Output / 255);
        timer = millis();
        Serial.print("A: ");
        Serial.print(";t = ");
        Serial.print(timer);
        Serial.print(" ;T = " );
        Serial.print(Input);
        Serial.print(" ;CV = " );
        Serial.print(CV);
        Serial.println(";");
      }
      // Extension:
      timeStamp = millis();
      while (millis() < (4500 + timeStamp))
      {
        Input = readTemp();
        extensionPID.Compute();
        analogWrite(PWR, Output);
        float CV = V * (Output / 255);
        timer = millis();
        Serial.print("E: ");
        Serial.print(";t = ");
        Serial.print(timer);
        Serial.print(" ;T = " );
        Serial.print(Input);
        Serial.print(" ;CV = " );
        Serial.print(CV);
        Serial.println(";");
      }
    }
  }
  // Image Capture Sequence

```

```

digitalWrite(LED, HIGH); //trigger the LED on by making the voltage HIGH
digitalWrite(CCD, HIGH); //trigger the CCD on by making the voltage HIGH
delay(expt); //delay for the specified exposure time
digitalWrite(CCD, LOW); //trigger the CCD off by making the voltage LOW
digitalWrite(LED, LOW); //trigger the LED off by making the voltage LOW
Serial.print("Image Capture: Cycle ");
Serial.println(i);
}
if (i >= 1 && i < numCycles)
{
    // Denature:
    timeStamp = millis();
    while (millis() < (5000 + timeStamp))
    {
        Input = readTemp();
        denaturePID.Compute();
        analogWrite(PWR, Output);
        float CV = V * (Output / 255);
        timer = millis();
        Serial.print("D: ");
        Serial.print("t = ");
        Serial.print(timer);
        Serial.print(" ; T = " );
        Serial.print(Input);
        Serial.print(" ; CV = " );
        Serial.print(CV);
        Serial.println("");
    }
    // Anneal:
    timeStamp = millis();
    while (millis() < (4500 + timeStamp))
    {
        Input = readTemp();
        annealPID.Compute();
        analogWrite(PWR, Output);
        float CV = V * (Output / 255);
        timer = millis();
        Serial.print("A: ");
        Serial.print("t = ");
        Serial.print(timer);
        Serial.print(" ; T = " );
        Serial.print(Input);
        Serial.print(" ; CV = " );
        Serial.print(CV);
        Serial.println("");
    }
    // Extension:
    timeStamp = millis();
    while (millis() < (4500 + timeStamp))
    {
        Input = readTemp();
        extensionPID.Compute();
        analogWrite(PWR, Output);
        float CV = V * (Output / 255);
        timer = millis();
        Serial.print("E: ");
        Serial.print("t = ");
        Serial.print(timer);
        Serial.print(" ; T = " );
        Serial.print(Input);
        Serial.print(" ; CV = " );
        Serial.print(CV);
        Serial.println("");
    }
    // Image Capture Sequence
    digitalWrite(LED, HIGH); //trigger the LED on by making the voltage HIGH
    digitalWrite(CCD, HIGH); //trigger the CCD on by making the voltage HIGH
    delay(expt); //delay for the specified exposure time
    digitalWrite(CCD, LOW); //trigger the CCD off by making the voltage LOW

```

```

digitalWrite(LED, LOW); //trigger the LED off by making the voltage LOW
Serial.print("Image Capture: ");
Serial.println(i + 1);
}
if (i == numCycles)
{
    //Final Extension:
    timeStamp = millis();
    while (millis() < (30000 + timeStamp))
    {
        Input = readTemp();
        extensionPID.Compute();
        analogWrite(PWR, Output);
        float CV = V * (Output / 255);
        timer = millis();
        Serial.print("FE: ");
        Serial.print("t = ");
        Serial.print(timer);
        Serial.print(" ;T = ");
        Serial.print(Input);
        Serial.print(" ;CV = ");
        Serial.print(CV);
        Serial.println("");
    }
    break;
}
}
}

float readTemp() //readTemp function performs a mode filter
{
    int NUM_READS = 100; //number of samples
    int sensorpin = A1; //temperature sensor input

    // read multiple values and sort them to take the mode
    int sortedValues[NUM_READS];
    for (int i = 0; i < NUM_READS; i++) {
        int value = analogRead(sensorpin);
        int j;
        if (value < sortedValues[0] || i == 0) {
            j = 0; //insert at first position
        }
        else {
            for (j = 1; j < i; j++) {
                if (sortedValues[j - 1] <= value && sortedValues[j] >= value) {
                    // j is insert position
                    break;
                }
            }
        }
        for (int k = i; k > j; k--) {
            // move all values higher than current reading up one position
            sortedValues[k] = sortedValues[k - 1];
        }
        sortedValues[j] = value; //insert current reading
    }
    //return scaled mode of 10 values
    float returnval = 0;
    for (int i = NUM_READS / 2 - 5; i < (NUM_READS / 2 + 5); i++)
    {
        returnval += sortedValues[i];
    }
    returnval = returnval / 10;
    float V = returnval * (5.0 / 1023);
    float T_M = m_M * V + b_M; //temperature conversion to model
    float T = m * T_M + b; //temperature transformation based on mismatch between sensor reading and chamber temp
    return T;
}

```

Appendix 3:

```
#include <PID_v1.h>
#include <SPI.h>
#include "Adafruit_MAX31855.h"

//Voltage supply set to 3.0V constant voltage
int PWR = 5;

//Initailize timers
unsigned long timeStamp = 0;
unsigned long timer = 0;

double Temp;

//Define parameters of chip calibration for temperature conversion
float m_M = 17.804; //slope of the calibration equation in the form of [T = m*V + b]
float b_M = 26.662; //the intercept of the calibration curve

//Define conversion factor for mismatch between sensor and reaction chamber
float m = 1.014;
float b = -6.178;

//Image Capture Parameters:
int CCD = 9; //CCD trigger I/O pin 9
int LED = 11; //LED trigger I/O pin 11
int expt = 1000; //CCD exposure time in milliseconds

int pwm = 115.0;
int tempdata = 0;

void setup()
{
  pinMode(LED, OUTPUT); // initialize the led digital pin as an output.
  pinMode(CCD, OUTPUT); // initialize the CCD trigger digital pin as an output.
  pinMode(PWR, OUTPUT); // initialize the power PWM pins as output

  //Initailize serial monitor
  Serial.begin(9600);
  Serial.println("Benchtop HRMA Program");

  // wait for MAX chip to stabilize
  delay(1000);
}

void loop()
{
  while (tempdata < 71) //limits the loop to the last melt setpoint
  {
    timeStamp = millis();
    while (millis() < (timeStamp + 10000)); //takes timestamp and then for 10 seconds stays on one PWM output value
    {
      float Temp = readTemp();
      analogWrite(PWR, pwm);
      timer = millis();
      if (timer > 10000) //looks for a range for the melt temperature due to float point decimals
      {
        // Image Capture Sequence
        digitalWrite(LED, HIGH); //trigger the CCD on by making the voltage HIGH
        digitalWrite(CCD, HIGH); //trigger the CCD on by making the voltage HIGH
        delay(expt); //delay for the specified exposure time
        digitalWrite(CCD, LOW); //trigger the CCD off by making the voltage LOW
        digitalWrite(LED, LOW); //trigger the CCD off by making the voltage LOW
        Serial.println(Temp);
        tempdata = tempdata + 1; //adds increment value to the melt set point
        pwm = pwm + 2; //add to the output to try and drive the temperature up
        break;
      }
    }
  }
}
```

```

    }
  }
}

float readTemp() //readTemp function performs a mode filter
{
  int NUM_READS = 100; //number of samples
  int sensorpin = A1; //temperature sensor input

  // read multiple values and sort them to take the mode
  int sortedValues[NUM_READS];
  for (int i = 0; i < NUM_READS; i++) {
    int value = analogRead(sensorpin);
    int j;
    if (value < sortedValues[0] || i == 0) {
      j = 0; //insert at first position
    }
    else {
      for (j = 1; j < i; j++) {
        if (sortedValues[j - 1] <= value && sortedValues[j] >= value) {
          // j is insert position
          break;
        }
      }
    }
    for (int k = i; k > j; k--) {
      // move all values higher than current reading up one position
      sortedValues[k] = sortedValues[k - 1];
    }
    sortedValues[j] = value; //insert current reading
  }
  //return scaled mode of 10 values
  float returnval = 0;
  for (int i = NUM_READS / 2 - 5; i < (NUM_READS / 2 + 5); i++)
  {
    returnval += sortedValues[i];
  }
  returnval = returnval / 10;
  float V = returnval * (5.0 / 1023);
  float T_M = m_M * V + b_M; //temperature conversion to model
  float T = m * T_M + b; //temperature transformation based on mismatch between sensor reading and chamber temp
  return T;
}

```

Appendix 4:

```
function [f, gof] = HRMA(Temperature, MeanIntensity)
%CREATEFIT(VARNAME1,VARNAME2)
% Create a fit.
%
% Data for 'HRMA' fit:
%   X Input : VarName1
%   Y Output: VarName2
% Output:
%   f : a fit object representing the fit.
%   gof : structure with goodness-of fit info.
%% Fit: 'HRMA'.
[xData, yData] = prepareCurveData(Temperature, MeanIntensity);

% Set up fittype and options.
ft = fittype( 'smoothingspline' );
opts = fitoptions( 'Method', 'SmoothingSpline' );
opts.SmoothingParam = 0.4126620833002733;

% Fit model to data.
f = fit(xData, yData, ft);
[f, gof] = fit(xData, yData, ft, opts);

%Output the derivative of the spline fit at the x data point
d_dT = differentiate(f, xData);
neg_d_dT = d_dT*(-1);

%Find melt peak
[M,I] = max(neg_d_dT);
T_m = xData(I);

% Plot Melt Curve Data with fit.
figure( 'Name', 'Melt Curve' );
h = plot( f, xData, yData );
legend( h, 'Melt Data', 'spline fit', 'Location', 'NorthEast' );
% Label axes
title('Melt Curve' );
xlabel ('Temperature (degC)');
ylabel ('Fluorescence (470 – 520 nm)');
grid off;

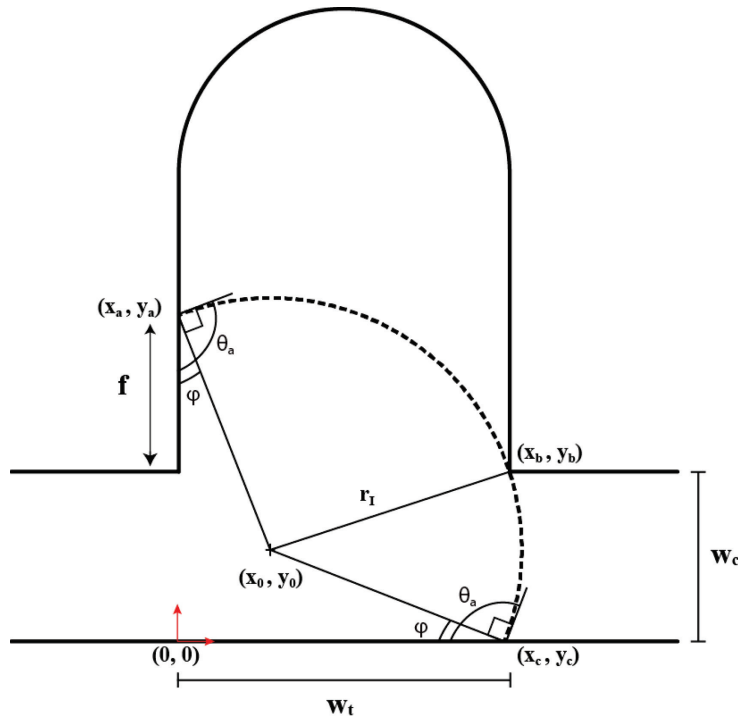
% Plot HRMA.
figure( 'Name', 'HRMA' );
h = plot( xData, neg_d_dT );
z = line([T_m,T_m],[0,M],'Color',[1 0 0],'LineStyle','-');
legend(z, ['T_m = ', num2str(T_m)], 'Location', 'NorthEast' );

% Label axes
title('HRMA' );
xlabel ('Temperature (degC)');
ylabel ('-(d/dT) Fluorescence (470 – 520 nm)');
grid off;
```

Appendix 5:

Appendix 5 present the geometric models used to establish the relationships between physical system parameters, including contact angle (θ_a) and channel width ratio (CR), and the resulting filling ratio (FR) that defines the degree of intrusion of fluid into a given trap. For each model, the non-linear system of equations with associated constraints were solved in Mathematica to determine the fluid intrusion length (f) for each design.

Geometric model for a single-sided trap design.



Assumptions: Constant interface curvature

Unknowns: x_0, y_0, y_a, r

Knowns: $x_a = 0, x_b = w_t, x_c = y_a, y_b = w_c, y_c = 0, \theta, \varphi$

Constraints: $y_a \geq w_c, r_I \geq 0$

Equation 1: $x_0^2 + (y_a - y_0)^2 = r_I^2$

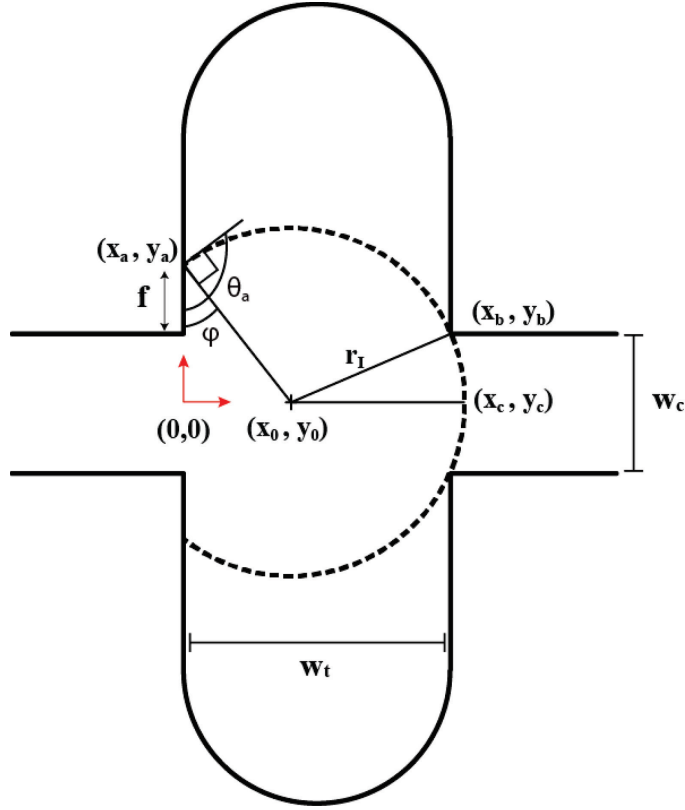
Equation 2: $(w_t - x_0)^2 + (w_c - y_0)^2 = r_I^2$

Equation 3: $(y_a - x_0)^2 + y_0^2 = r_I^2$

Equation 4: $\tan(\varphi) = \frac{x_0}{y_a - y_0}$

Solve: $f = y_a - w_c$

Geometric model for the double-sided trap design.



Assumptions: Constant interface curvature, symmetric advancement of interfaces along both trap walls

Unknowns: x_0, y_a, r

Knowns: $x_a = 0, x_b = w_t, y_0 = 0, y_b = \frac{w_c}{2}, y_c = 0, \theta, \varphi$

Constraints: $y_a \geq \frac{w_c}{2}, r_l \geq 0, \theta_{lim}(CR)$

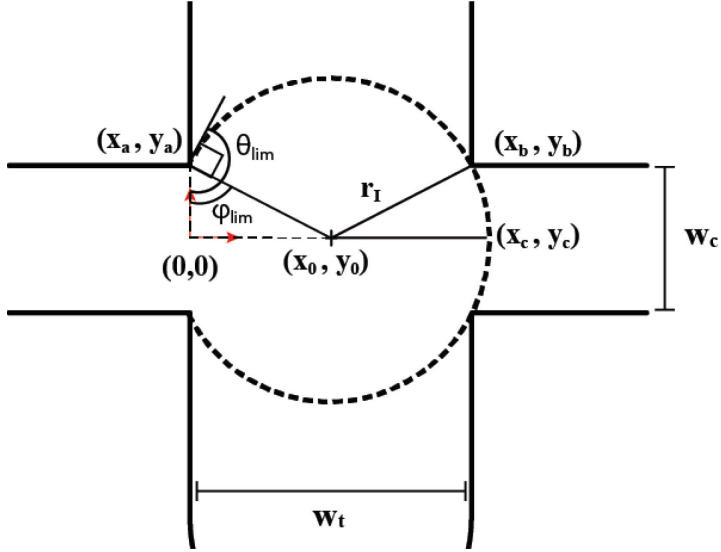
Equation 1: $x_0^2 + y_a^2 = r_l^2$

Equation 2: $(w_t - x_0)^2 + \left(\frac{w_c}{2}\right)^2 = r_l^2$

Equation 4: $\tan(\varphi) = \frac{x_0}{y_a}$

Solve: $f = y_a - \frac{w_c}{2}$

Model for determining θ_{lim} , defined as the upper limit of θ_a above which fluid will not advance into the trap. Note that θ_{lim} is a function of the channel width ratio.

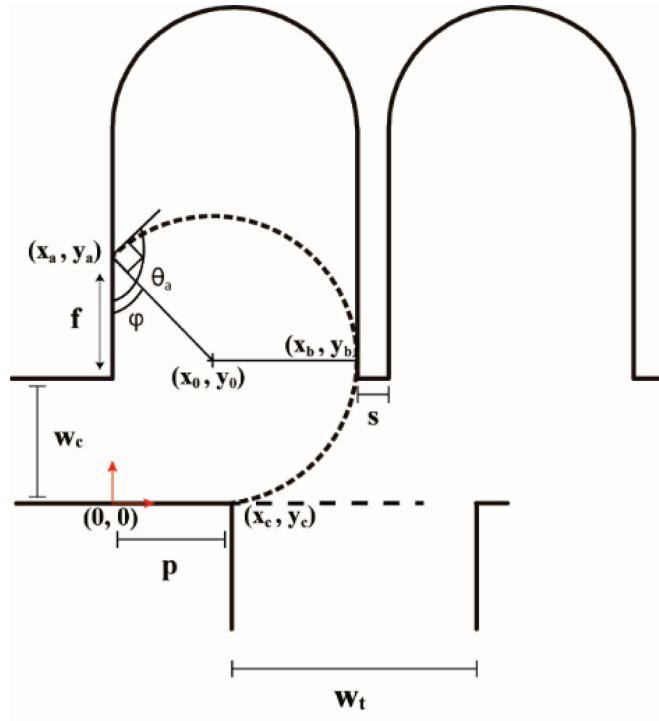


Constant curvature $\rightarrow x_0 = \frac{w_t}{2}$ and $y_a = \frac{w_c}{2}$

$$\tan(\phi_{lim}) = \frac{w_t}{w_c}$$

$$\theta_{lim} = \phi_{lim} + \frac{\pi}{2}$$

Geometric model for the staggered-sided trap design.



Assumptions: Constant interface curvature

Unknowns: x_0, y_0, y_a, r

Knowns: $x_a = 0, x_b = w_t, x_c = p, y_b = y_0, y_c = 0, \theta, \phi$

Constraints: $y_a \geq w_c, r_l \geq 0, y_0 \geq w_c$

Equation 1: $x_0^2 + (y_a^2 - y_0^2) = r_l^2$

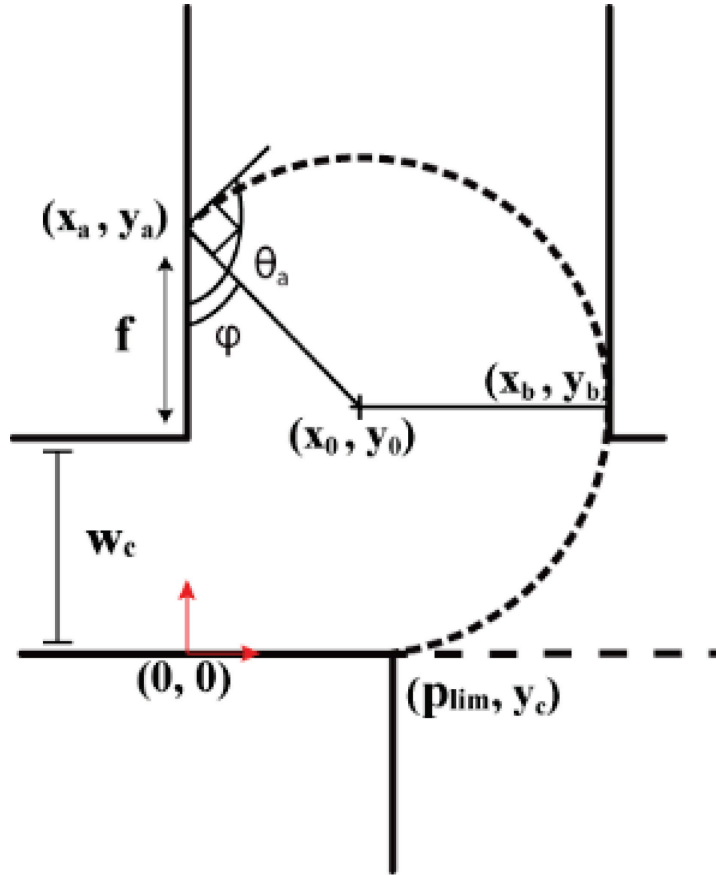
Equation 2: $(w_t - x_0)^2 = r_l^2$

Equation 3: $(p - x_0)^2 + y_0^2 = r_l^2$

Equation 4: $\tan(\phi) = \frac{x_0}{y_a - y_0}$

Solve: $f = y_a - w_c$

Derivation for the p_{lim} which determines at what p the staggered configuration will act as a single sided configuration because the pinning point is not reached before the interface contacts the opposite wall. Note that p_{lim} is a function of the filling ratio and advancing contact angle.



Assumptions: Constant interface curvature

Unknowns: x_0, y_0, y_a, r

Knowns: $x_a = 0, x_b = w_t, y_a = p_{lim}, y_c = 0, \theta, \varphi$

Constraints: $y_a \geq w_c, r_l \geq 0$

Equation 1: $x_0^2 + (p_{lim} - y_0)^2 = r_l^2$

Equation 2: $(w_t - x_0)^2 + (w_c - y_0)^2 = r_l^2$

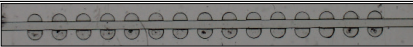
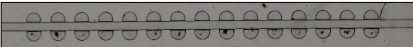
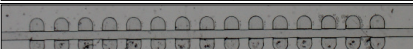
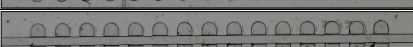
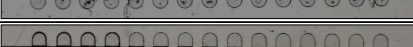
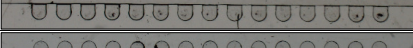
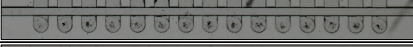
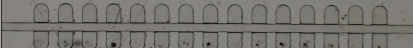
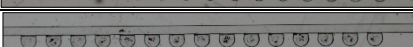
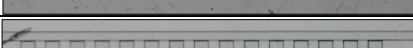
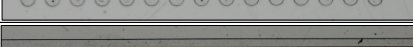
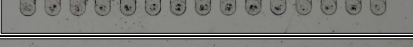
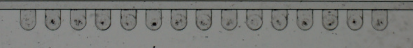
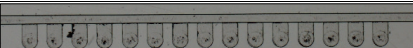
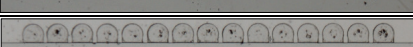
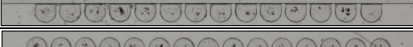
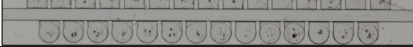
Equation 3: $(p_{lim} - x_0)^2 + y_0^2 = r_l^2$

Equation 4: $\tan(\varphi) = \frac{x_0}{p_{lim} - y_0}$

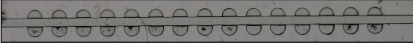
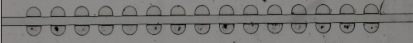
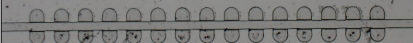
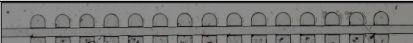
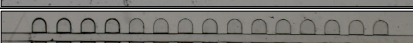
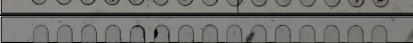
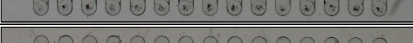
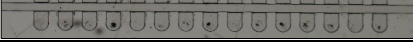
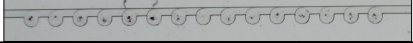
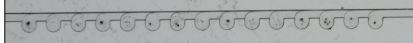
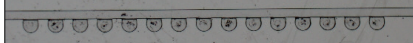
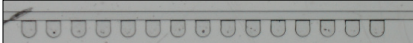
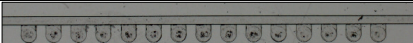
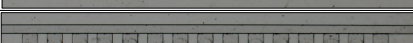
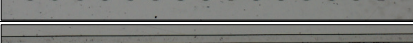
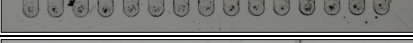
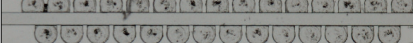


Solve for p_{lim} (FR, θ_a) using the single sided model. If $p > p_{lim}$ then pinning does not occur for that configuration.

Appendix 6a:

Loading data set for the self-loading and self-digitizing devices with trap depth less than main channel depth. Mean and standard deviation reported for each set of measurements.


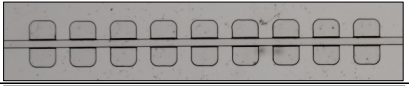


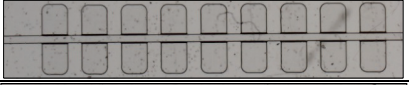
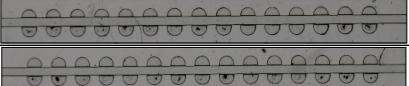
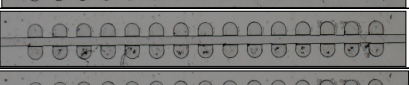
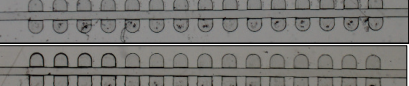

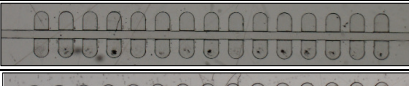
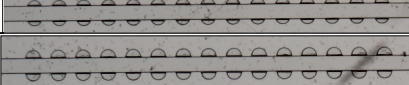
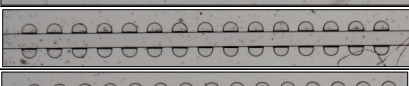
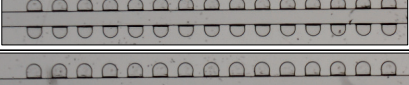
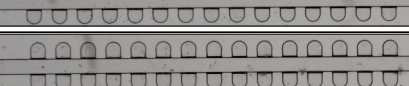
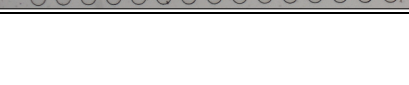



Image	FR (f/w_t)	CR (w_c/w_t)	Config	Filling % for each experiment					Mean	σ
				1	2	3	4	5		
	0.49	0.55	Double	1.00	0.93	1.00	1.00	1.00	98.7%	0.03
	0.64	0.55	Double	1.00	1.00	1.00	1.00	1.00	100.0%	0.00
	0.73	0.55	Double	1.00	1.00	1.00	0.90	1.00	98.0%	0.04
	0.88	0.55	Double	0.97	1.00	0.97	1.00	0.90	96.7%	0.04
	1.06	0.55	Double	0.53	0.57	0.53	0.87	0.83	66.7%	0.15
	1.17	0.55	Double	0.53	0.40	0.53	0.57	0.53	51.3%	0.06
	1.31	0.55	Double	0.53	0.33	0.37	0.53	0.40	43.3%	0.08
	0.88	0.55	Single	1.00	0.93	0.93	0.87	1.00	94.7%	0.05
	1.06	0.55	Single	0.40	0.33	0.53	0.53	0.33	42.7%	0.09
	1.17	0.55	Single	0.20	0.60	0.53	0.13	0.20	33.3%	0.19
	1.31	0.55	Single	0.07	0.13	0.20	0.20	0.20	16.0%	0.05
	1.59	0.55	Single	0.40	0.00	0.00	0.27	0.07	14.7%	0.16
	0.88	0.55	Staggered	1.00	1.00	1.00	1.00	1.00	100.0%	0.00
	1.06	0.55	Staggered	1.00	1.00	0.90	1.00	1.00	97.9%	0.04
	1.17	0.55	Staggered	0.90	0.86	1.00	1.00	1.00	95.2%	0.06
	1.31	0.55	Staggered	1.00	1.00	1.00	1.00	1.00	100.0%	0.00
	1.59	0.55	Staggered	0.90	1.00	0.66	1.00	0.93	89.7%	0.13



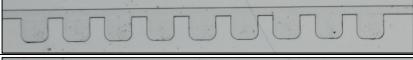
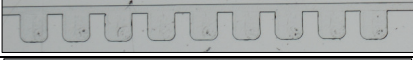
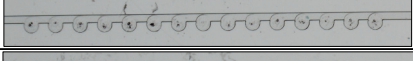
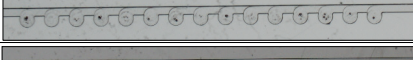
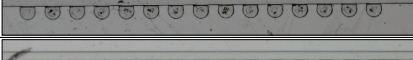
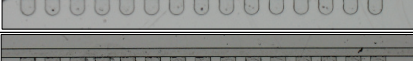
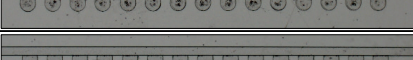
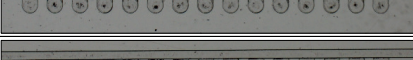
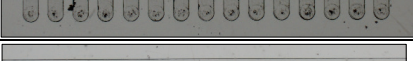
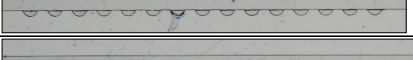
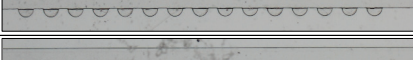
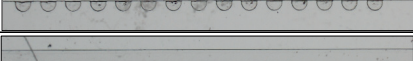
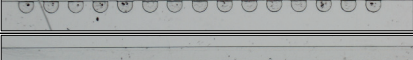
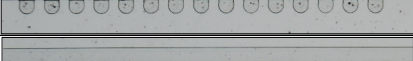
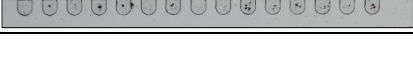
Loading data set for the self-loading and self-digitizing device with trap depth equal to the main channel depth. Mean and standard deviation reported for each set of measurements.





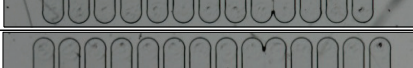
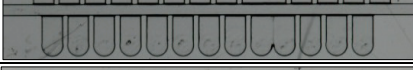
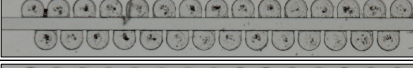




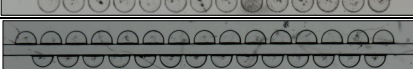


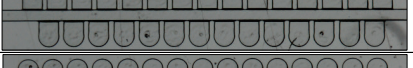
Image	FR (f/w_t)	CR (w_c/w_t)	Config	Filling % for each experiment					Mean	σ
				1	2	3	4	5		
	0.49	0.55	Double	1.00	1.00	1.00	1.00	1.00	100.0%	0.00
	0.64	0.55	Double	0.97	1.00	1.00	1.00	0.97	98.7%	0.02
	0.73	0.55	Double	0.93	1.00	0.90	0.90	0.97	94.0%	0.04
	0.88	0.55	Double	0.97	1.00	0.97	1.00	0.90	96.7%	0.04
	1.06	0.55	Double	0.50	0.47	0.57	0.77	0.67	59.3%	0.11
	1.17	0.55	Double	0.47	0.63	0.60	0.57	0.63	58.0%	0.06
	1.31	0.55	Double	0.33	0.41	0.40	0.53	0.27	38.8%	0.09
	0.65	0.55	Single	1.00	1.00	1.00	1.00	1.00	100.0%	0.00
	0.76	0.55	Single	1.00	1.00	1.00	1.00	1.00	100.0%	0.00
	0.88	0.55	Single	0.93	0.93	1.00	0.80	0.73	88.0%	0.10
	1.06	0.55	Single	0.27	0.00	0.00	0.07	0.00	6.7%	0.10
	1.17	0.55	Single	0.00	0.47	0.47	0.33	0.33	32.0%	0.17
	1.31	0.55	Single	0.00	0.00	0.00	0.00	0.00	0.0%	0.00
	1.59	0.55	Single	0.00	0.00	0.00	0.00	0.00	0.0%	0.00
	0.88	0.59	Staggered	1.00	1.00	1.00	1.00	1.00	100.0%	0.00
	1.06	0.59	Staggered	1.00	1.00	1.00	1.00	1.00	100.0%	0.00
	1.17	0.59	Staggered	0.97	1.00	0.97	0.97	1.00	97.9%	0.02
	1.31	0.59	Staggered	0.97	0.97	0.97	1.00	0.97	97.2%	0.01
	1.59	0.59	Staggered	0.55	0.48	0.28	0.31	0.31	38.6%	0.11

Appendix 6b

Parametric data set the self-loading and self-digitizing chip loading experiments. Mean and standard deviation reported for each set of measurements.

Image	FR (f/w_t)	CR (w_c/w_t)	Config	Filling % for each experiment					Mean	σ
				1	2	3	4	5		
	0.60	0.31	Double	1.00	1.00	1.00	1.00	1.00	100.0%	0.00
	0.73	0.31	Double	0.94	1.00	1.00	0.94	1.00	97.8%	0.03
	0.88	0.31	Double	0.78	0.56	0.83	0.83	0.83	76.7%	0.11
	1.02	0.31	Double	0.50	0.50	0.50	0.61	0.50	52.2%	0.04
	1.18	0.31	Double	0.50	0.50	0.33	0.22	0.56	42.2%	0.12
	0.49	0.55	Double	1.00	1.00	1.00	1.00	1.00	100.0%	0.00
	0.64	0.55	Double	0.97	1.00	1.00	1.00	0.97	98.7%	0.02
	0.73	0.55	Double	0.93	1.00	0.90	0.90	0.97	94.0%	0.04
	0.88	0.55	Double	0.97	1.00	0.97	1.00	0.90	96.7%	0.04
	1.06	0.55	Double	0.50	0.47	0.57	0.77	0.67	59.3%	0.11
	1.17	0.55	Double	0.47	0.63	0.60	0.57	0.63	58.0%	0.06
	1.31	0.55	Double	0.33	0.41	0.40	0.53	0.27	38.8%	0.09
	0.40	1.00	Double	1.00	1.00	1.00	1.00	1.00	100.0%	0.00
	0.57	1.00	Double	0.97	1.00	0.97	1.00	1.00	98.7%	0.02
	0.67	1.00	Double	0.87	0.93	0.90	0.80	0.93	88.7%	0.05
	0.83	1.00	Double	0.75	0.77	0.90	0.53	0.83	75.7%	0.12
	0.95	1.00	Double	0.64	0.80	0.60	0.50	0.77	66.2%	0.11
	1.08	1.00	Double	0.33	0.40	0.37	0.30	0.30	34.0%	0.04

	0.56	0.31	Single	1.00	1.00	1.00	1.00	1.00	100.0%	0.00
	0.70	0.31	Single	1.00	1.00	1.00	1.00	1.00	100.0%	0.00
	0.85	0.31	Single	1.00	0.89	0.78	0.89	1.00	91.1%	0.08
	1.01	0.31	Single	0.44	0.56	0.67	0.22	0.44	46.7%	0.15
	0.65	0.55	Single	1.00	1.00	1.00	1.00	1.00	100.0%	0.00
	0.76	0.55	Single	1.00	1.00	1.00	1.00	1.00	100.0%	0.00
	0.88	0.55	Single	0.93	0.93	1.00	0.80	0.73	88.0%	0.10
	1.06	0.55	Single	0.27	0.00	0.00	0.07	0.00	6.7%	0.10
	1.17	0.55	Single	0.00	0.47	0.47	0.33	0.33	32.0%	0.17
	1.31	0.55	Single	0.00	0.00	0.00	0.00	0.00	0.0%	0.00
	1.59	0.55	Single	0.00	0.00	0.00	0.00	0.00	0.0%	0.00
	0.38	1.00	Single	1.00	1.00	1.00	1.00	1.00	100.0%	0.00
	0.51	1.00	Single	1.00	1.00	1.00	1.00	1.00	100.0%	0.00
	0.65	1.00	Single	1.00	1.00	1.00	1.00	1.00	100.0%	0.00
	0.78	1.00	Single	0.60	0.20	0.27	0.20	0.27	30.7%	0.15
	0.94	1.00	Single	0.20	0.47	0.27	0.07	0.13	22.7%	0.14
	1.10	1.00	Single	0.00	0.00	0.00	0.00	0.00	0.0%	0.00

	1.02	0.41	Staggered	1.00	1.00	1.00	1.00	1.00	100.0%	0.00
	1.18	0.41	Staggered	1.00	1.00	1.00	1.00	1.00	100.0%	0.00
	1.34	0.41	Staggered	1.00	1.00	1.00	1.00	1.00	100.0%	0.00
	1.64	0.41	Staggered	0.73	0.73	0.82	0.73	0.73	74.5%	0.04
	1.92	0.41	Staggered	0.09	0.00	0.00	0.27	0.00	7.3%	0.11
	0.88	0.59	Staggered	1.00	1.00	1.00	1.00	1.00	100.0%	0.00
	1.06	0.59	Staggered	1.00	1.00	1.00	1.00	1.00	100.0%	0.00
	1.17	0.59	Staggered	0.97	1.00	0.97	0.97	1.00	97.9%	0.02
	1.31	0.59	Staggered	0.97	0.97	0.97	1.00	0.97	97.2%	0.01
	1.59	0.59	Staggered	0.55	0.48	0.28	0.31	0.31	38.6%	0.11
	0.59	0.81	Staggered	1.00	1.00	1.00	1.00	1.00	100.0%	0.00
	0.88	0.81	Staggered	0.92	1.00	1.00	1.00	1.00	98.5%	0.03
	1.04	0.81	Staggered	0.92	0.92	1.00	1.00	1.00	96.9%	0.04
	1.15	0.81	Staggered	0.93	0.93	0.71	0.86	0.93	87.1%	0.08
	1.28	0.81	Staggered	0.21	0.14	0.07	0.14	0.14	14.3%	0.05

Appendix 7:

```
clc
clear all

%open image for volume analysis (make sure file is in Matlab folder)
I = imread('SLDChip_768_composite_thresh.jpg');

%calculate background profile
background = imopen(I,strel('disk',15));

%background correction
I2 = I - background;

%increase the image contrast
I3 = imadjust(I2,[0.2 0.7],[]);

%threshold the image
level = graythresh(I3);
bw = im2bw(I3,level);
bw2 = bwareaopen(bw, 50);

%identify objects in the image (4 is the connectivity parameter)
cc = bwconncomp(bw, 4);

%create data structure for each trap with (area, centroid, bounding box)
%fields
trapdata = regionprops(cc,'basic');

%establish baseline area for completely filled well (row 3 trap 8 (1 = top row, 1 =
%left row)
traparea_baseline_pix = 437; %(counted in photoshop)

%baseline volume conversion for completely filled well in nano liters
vol_conversion_nL = 11;

%filter image so that small connected pixels not representing traps are
%ignored
filter_low = arrayfun(@(trapdata) trapdata.Area > 20, trapdata);
trapdata = trapdata(filter_low);

%filter image so that large connected pixels are ignored
%( anything 20% larger than a full trap)
filter_high = arrayfun(@(trapdata) trapdata.Area < 1.2*traparea_baseline_pix ,
trapdata);
trapdata = trapdata(filter_high);
```

```

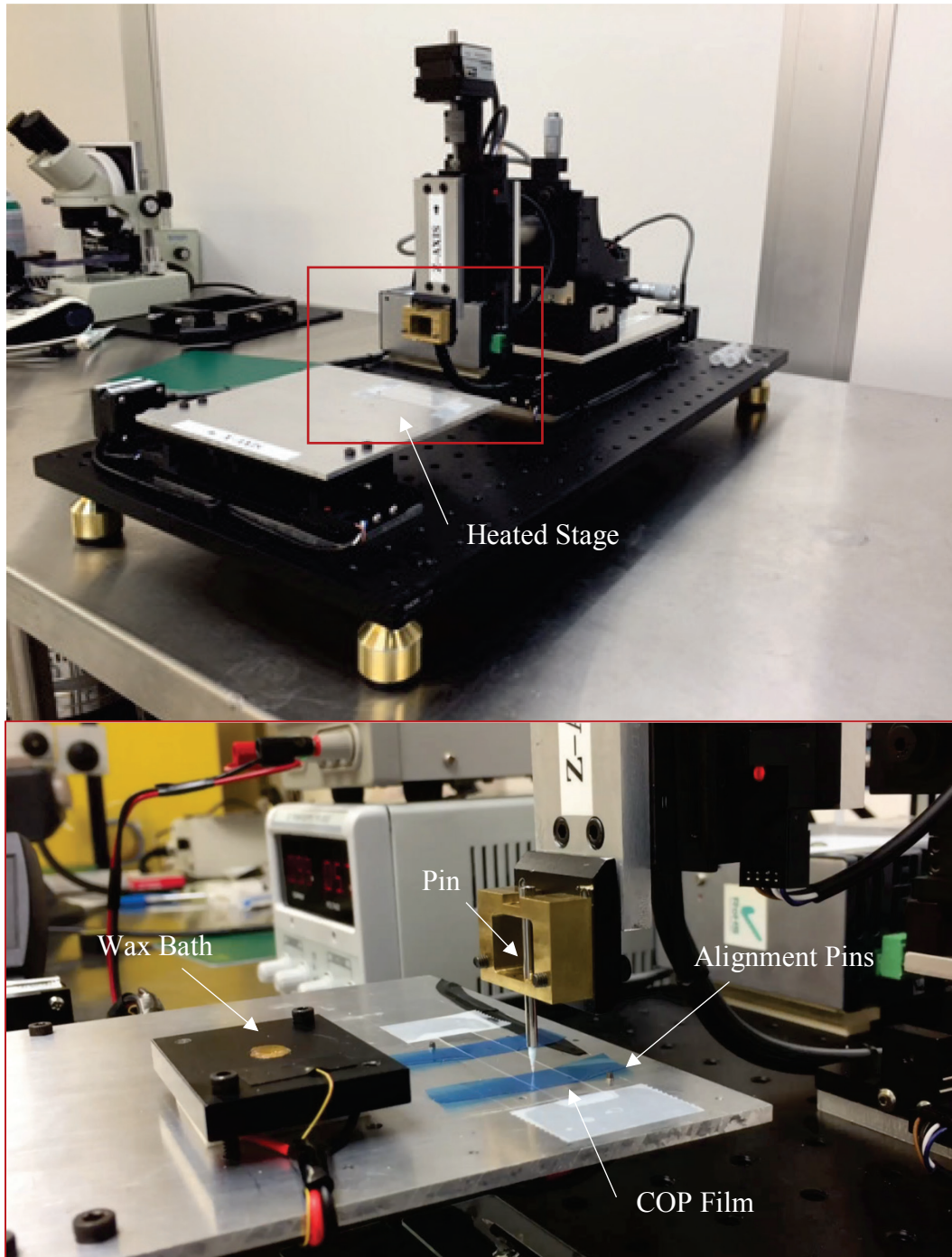
%trap area in pix divided by the baseline area for full well times volume
%conversion
trap_vols = ([trapdata.Area]/traparea_baseline_pix)*vol_conversion_nL;

%find mean and standard deviation of filtered data trap data (converted to
%volume
mu = mean(trap_vols)
sigma = std(trap_vols)

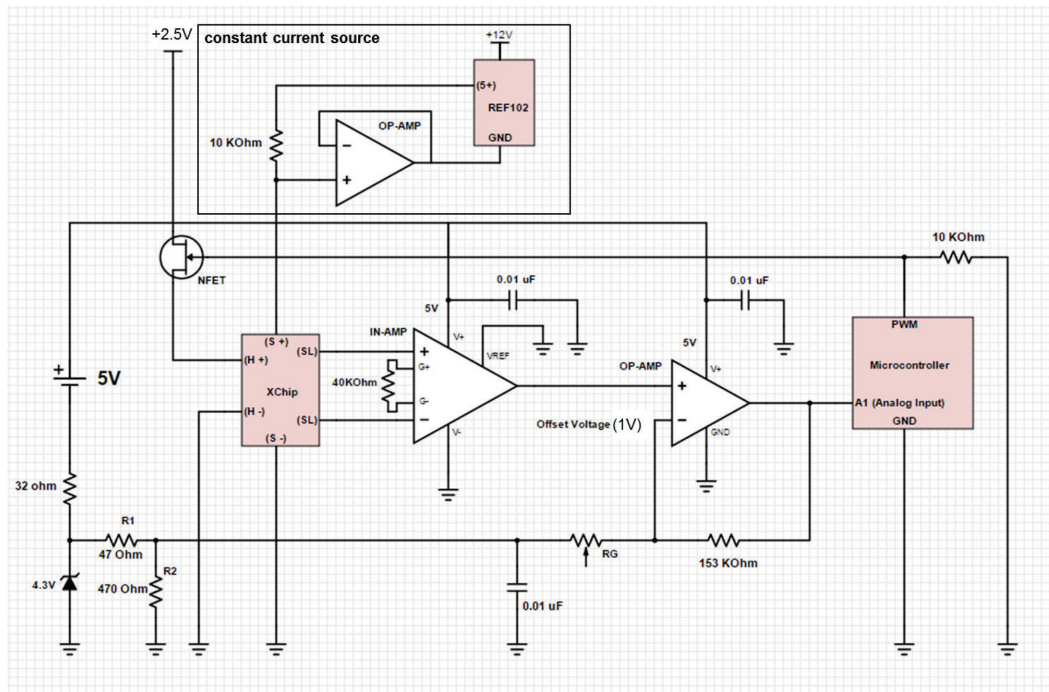
%subplot of trap volume histogram
figure
%subplot(2,2,[3,4])
histogram(trap_vols,14)
axis([0,16,0,220])
xlabel('Trap Volume (nL)') % x-axis label
ylabel('Trap Count') % y-axis label

```

Appendix 8:



Appendix 9



Circuit diagram for the rapid PCR device supporting system:

Constant Current Source – In order to probe resistance of the sensor a constant current source was used to apply a constant 1 mA load across the sensor ($S^+ \rightarrow S^-$). A 10V reference voltage (REF102CP) with a high precision 10kOhm resistor (Y006910K0000J0L) in series with the sensor element was used to accomplish this. An OP-AMP (OPA277P) was incorporated in series with the ground pin of the REF102CP to maintain the 10V across the circuit.

Power Modulation – 2.5V was applied to the heating elements (H^+ and H^-) was setup to be modulated by the sensor feedback. The sensor output would be fed into a PID algorithm that would output a duty cycle for a n-type mosfet (FQP30N06L). 12V was applied to the 10V voltage reference. 5V was applied to the LED and to power all of the circuit components.

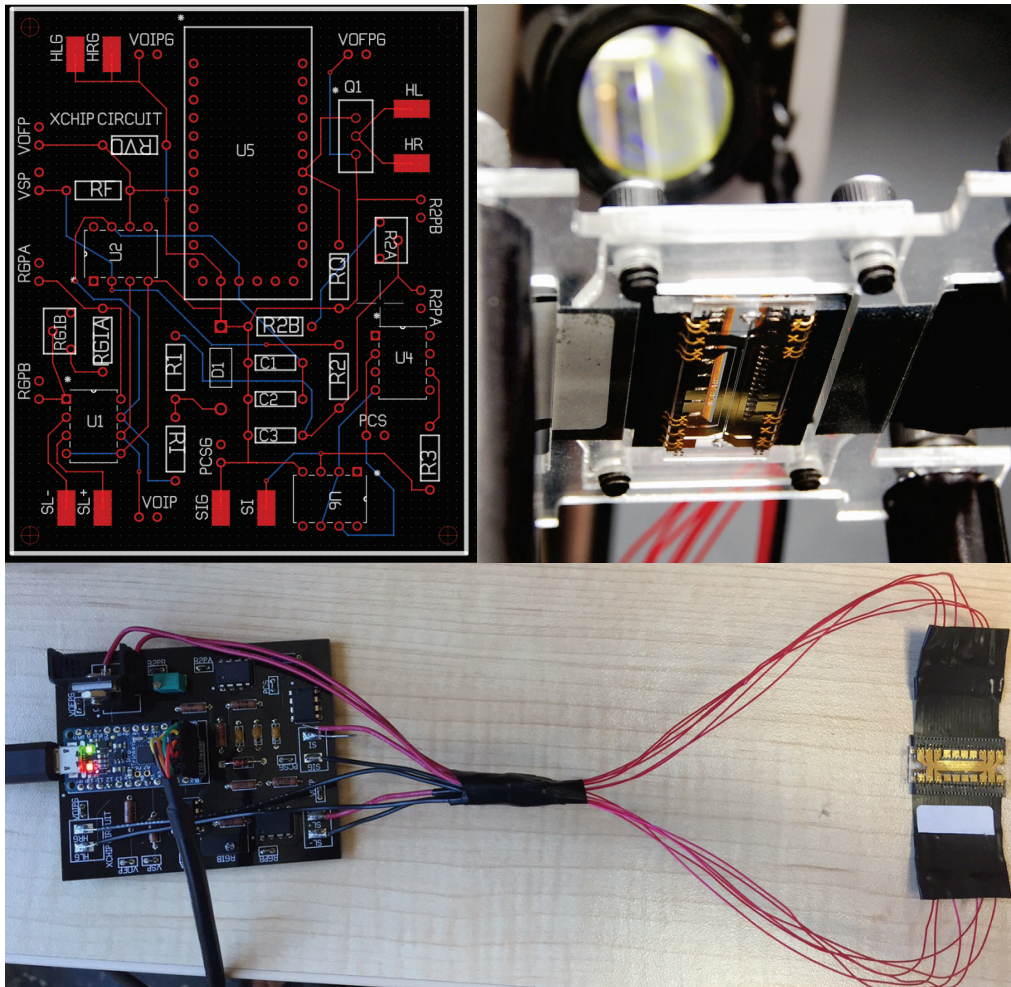
Sensor Output – Sensor leads on the device were connected to an IN-AMP (INA122P) in order to probe the voltage drop across the sensor lead. The voltage drop was on the mV scale across the temperature range so a 10-40kOhm potentiometer was connected in series to define the gain such that approximately 1V was the voltage drop across the sensor for room temperature.

Level Shift and Amplifier Circuit – An OP-AMP (TLV2471IP) was used to level shift and amplify the raw voltage drop coming off the IN-AMP to span the entire analog input range of the Arduino microcontroller ($0V \rightarrow 5V$). Resistors in series with potentiometers were used to adjust the offset voltage to approximately equal the voltage drop coming off the

IN-AMP (~1V) so that RT would be approximately 0V drop and 100C would correspond to approximately 5V drop.

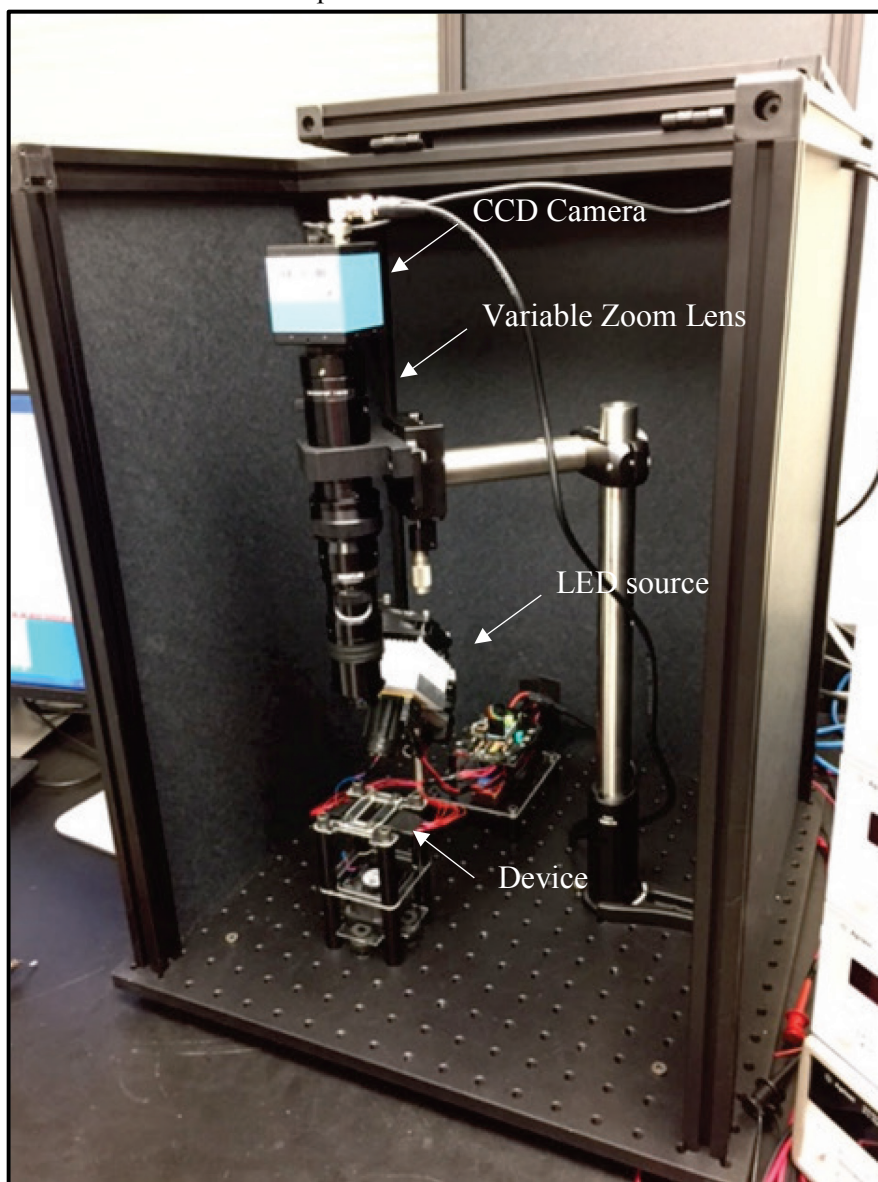
Microcontroller Temperature Sensing and Control – The microcontroller read the voltage output from the level shift amplifier and with a known 1mA constant current determined the resistance (Ohms Law) of the sensor element. The resistance was correlated to temperature using a calibration process to find the TCR. The Arduino used that temperature to determine the power output to the heating elements through a PID algorithm. The Arduino would define the temperature set points based on time keeping within the loop structure (see Appendix 3). Images were taken at the end of the extension step.

Interfacing – A custom PCB was designed for the circuit and the PCB connected to the chip using spring loaded contact arms.



(Top Left) Custom PCB design for rapid PCR device supporting system. (Top Right) Device interfacing. (Bottom) Complete electrical assembly.

Optics – The optical system for the PCR benchtop consisted of a CCD camera (DMK41BU02, Imaging Source, Charlotte, NC, US) attached to a 2-5X variable zoom lens (ZOOM 6000, Navitar, Rochester, New York) with a 488 nm emission filter (EM01-R488-25, Semrock, Rochester, NY). The optics were positioned directly above the device reaction chamber and connected to a micro positioner stage for fine tune focusing. Also above the reaction chamber positioned at a 45 degree angle was an LED light source (2600N-701-14-C2, Innovations in Optics, Woburn, MA) for with a 452 nm excitation filter (FF01-452/45-20-D, Semrock, Rochester, NY). The CCD camera was triggered by a 5V pulse sent from the Arduino during the extension step and control over the shutter was defined by the length of the pulse. Additionally, the Arduino could actuate a relay switch connected to an LED light source (2600N-701-14-C2, Innovations in Optics, Woburn, MA, US) to illuminate when the shutter was open.

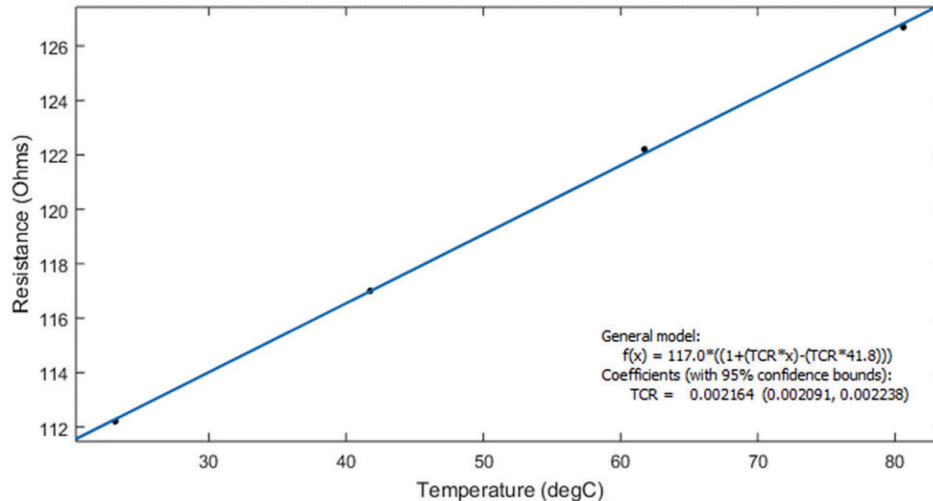


Appendix 10

The calibration process for each device consisted of 3 steps:

Burn in – This step consisted of applying varying levels of current across the heating elements that corresponded to the temperature steps during thermocycling. Current cycling was done to current anneal the elements instead of temperature annealing them, which was not possible due to the temperature constraints of the thermoplastic substrate. Current annealing was judged successful when the resistance at 50C would be equal whether it was heated to that temperature or cooled to that temperature, in other words without hysteresis (Appendix 1).

TCR Calculation – During this step the temperature coefficient of resistance for each chip was determined. The device was placed in a temperature controlled oven and multimeter leads were attached to the sensor elements. A thermocouple was placed in the oven to measure temperature. The resistance was recorded at 4-5 temperature points and plotted (see figure below).



The data was fitted to the following equation:

$$R = R_0[1 + \alpha(T-T_0)]$$

With α , initial resistance (R_0), and initial temperature (T_0) a temperature model can be formulated to correlate any resistance to temperature.

Calibration – During this step the sensor output (voltage drop) was equated to a temperature using the α and this equation was used in the software to convert the analog input to temperature. The temperature sensor needed to be calibrated further to achieve the temperature accuracy required for HRMA. A temperature sensitive dye was loaded into the chamber that would see a drop off in fluorescence at 2 temperatures. A melting routine was run on the device loaded with the calibration dye and the melt peaks were recorded. The recorded melting peaks were plotted against the reported melting temperatures of the dye and fitted to a conversion equation that accounted for any temperature offset.

Bibliography

- [1] G. Wu and M. H. Zaman, “Low-cost tools for diagnosing and monitoring HIV infection in low-resource settings,” *Bull. World Health Organ.*, vol. 90, no. 12, pp. 914–920, 2012.
- [2] National Institutes of Health, “Point-of-Care Diagnostic Testing,” *Res. Portf. Online Report. Tools*, no. October, pp. 1–2, 2010.
- [3] P. Yager, T. Edwards, E. Fu, K. Helton, K. Nelson, M. R. Tam, and B. H. Weigl, “Microfluidic diagnostic technologies for global public health,” *Nature*, vol. 442, no. 7101, pp. 412–418, 2006.
- [4] O. M. Koriech, “Breast Cancer and Early Detection,” *J. Family Community Med.*, vol. 3, no. 1, pp. 7–9, 1996.
- [5] J. E. Golub, S. Bur, W. A. Cronin, S. Gange, N. Baruch, G. W. Comstock, and R. E. Chaisson, “Delayed tuberculosis diagnosis and tuberculosis transmission,” *Int J Tuberc Lung Dis*, vol. 10, no. 1, pp. 24–30, 2000.
- [6] W. Stevens, N. Gous, N. Ford, and L. E. Scott, “Feasibility of HIV point-of-care tests for resource-limited settings: challenges and solutions,” *BMC Med.*, vol. 12, no. 1, p. 173, 2014.
- [7] WHO, “Antimicrobial Resistance: Global Report on Surveillance,” *World Heal. Organ.*, 2014.
- [8] A. Van Belkum, G. Durand, M. Peyret, S. Chatellier, G. Zambardi, J. Schrenzel, D. Shortridge, A. Engelhardt, and W. M. Dunne, “Rapid clinical bacteriology and its future impact,” *Annals of Laboratory Medicine*, vol.

- 33, no. 1. pp. 14–27, Jan-2013.
- [9] A. Manz, N. Graber, and H. Widmer, “Miniaturized total chemical analysis systems: a novel concept for chemical sensing,” *Sensors actuators B Chem.*, 1990.
 - [10] G. M. Whitesides, “The origins and the future of microfluidics,” *Nature*, vol. 442, no. 7101, pp. 368–373, 2006.
 - [11] M. A. Northrup, M. T. Ching, R. M. White, and R. T. Watson, “DNA Amplification in a Microfabricated Reaction Chamber,” in *Proc. Transducers '93, 7th International Conference on Solid State Sensors and Actuators*, 1993, pp. 924–927.
 - [12] M. A. Northrup, C. Gonzalez, D. Hadley, R. F. Hills, P. Landre, S. Lehw, R. Saw, J. J. Sninsky, and R. Watson, “A MEMS-based DNA Analysis System,” in *Transducers '95, 8th International Conference on Solid State Sensors and Actuators*, 1995, pp. 764–767.
 - [13] D. C. Duffy, J. C. McDonald, O. J. A. Schueller, and G. M. Whitesides, “Rapid prototyping of microfluidic systems in poly(dimethylsiloxane),” *Anal. Chem.*, vol. 70, no. 23, pp. 4974–4984, 1998.
 - [14] X. Li, D. R. Ballerini, and W. Shen, “A perspective on paper-based microfluidics: Current status and future trends,” *Biomicrofluidics*, vol. 6, no. 1, pp. 11301–11313, Mar. 2012.
 - [15] O. R??tting, W. R??pke, H. Becker, and C. G??rtner, “Polymer microfabrication technologies,” *Microsystem Technologies*, vol. 8, no. 1. Springer Berlin / Heidelberg, pp. 32–36, 2002.

- [16] S. H. Ng and Z. F. Wang, "Hot roller embossing for the creation of microfluidic devices," in *DTIP of MEMS and MOEMS - Symposium on Design, Test, Integration and Packaging of MEMS/MOEMS*, 2008, pp. 262–266.
- [17] M. Focke, D. Kosse, C. Müller, H. Reinecke, R. Zengerle, and F. von Stetten, "Lab-on-a-Foil: microfluidics on thin and flexible films.," *Lab Chip*, vol. 10, no. 11, pp. 1365–86, Jun. 2010.
- [18] C.-W. Tsao and D. L. Devoe, "Bonding of thermoplastic polymer microfluidics," *Microfluid. Nanofluidics*, vol. 6, no. 1, pp. 1–16, 2008.
- [19] O. D. Rahmanian and D. L. DeVoe, "Single-use thermoplastic microfluidic burst valves enabling on-chip reagent storage," *Microfluid. Nanofluidics*, vol. 18, no. 5–6, pp. 1045–1053, May 2015.
- [20] T. I. Wallow, A. M. Morales, B. a Simmons, M. C. Hunter, K. L. Krafcik, L. a Domeier, S. M. Sickafoose, K. D. Patel, and A. Gardea, "Low-distortion, high-strength bonding of thermoplastic microfluidic devices employing case-II diffusion-mediated permeant activation," *Lab Chip*, vol. 7, no. 12, pp. 1825–1831, Dec. 2007.
- [21] F. Dang, S. Shinohara, O. Tabata, Y. Yamaoka, M. Kurokawa, Y. Shinohara, M. Ishikawa, and Y. Baba, "Replica multichannel polymer chips with a network of sacrificial channels sealed by adhesive printing method," *Lab Chip*, vol. 5, no. 4, pp. 472–478, 2005.
- [22] C. Lu, L. J. Lee, and Y.-J. Juang, "Packaging of microfluidic chips via interstitial bonding technique," *Electrophoresis*, vol. 29, no. 7, pp. 1407–

1414, 2008.

- [23] M. A. Roberts, J. S. Rossier, P. Bercier, and H. Girault, “UV Laser Machined Polymer Substrates for the Development of Microdiagnostic Systems,” *Anal. Chem.*, vol. 69, no. 11, pp. 2035–2042, Jun. 1997.
- [24] F.-C. Huang, Y.-F. Chen, and G.-B. Lee, “CE chips fabricated by injection molding and polyethylene/thermoplastic elastomer film packaging methods,” *Electrophoresis*, vol. 28, no. 7, pp. 1130–1137, 2007.
- [25] Y. Li, J. S. Buch, F. Rosenberger, D. L. DeVoe, and C. S. Lee, “Integration of Isoelectric Focusing with Parallel Sodium Dodecyl Sulfate Gel Electrophoresis for Multidimensional Protein Separations in a Plastic Microfluidic Network,” *Anal. Chem.*, vol. 76, no. 3, pp. 742–748, Feb. 2004.
- [26] C. W. Tsao, L. Hromada, J. Liu, P. Kumar, and D. L. DeVoe, “Low temperature bonding of PMMA and COC microfluidic substrates using UV/ozone surface treatment,” *Lab Chip*, vol. 7, no. 4, pp. 499–505, 2007.
- [27] O. Rahmanian, C.-F. Chen, and D. L. DeVoe, “Microscale Patterning of Thermoplastic Polymer Surfaces by Selective Solvent Swelling,” *Langmuir*, vol. 28, no. 35, pp. 12923–12929, Sep. 2012.
- [28] J. . Bryson, *Plastic Materials*, Seventh. Oxford, 1999.
- [29] A. Griebel, S. Rund, F. Schonfeld, W. Dorner, R. Konrad, and S. Hardt, “Integrated polymer chip for two-dimensional capillary gel electrophoresis,” *Lab Chip*, vol. 4, no. 1, pp. 18–23, 2004.
- [30] R. T. Kelly, T. Pan, and A. T. Woolley, “Phase-Changing Sacrificial

- Materials for Solvent Bonding of High-Performance Polymeric Capillary Electrophoresis Microchips,” *Anal. Chem.*, vol. 77, no. 11, pp. 3536–3541, Jun. 2005.
- [31] M. T. Koesdjojo, Y. H. Tennico, and V. T. Remcho, “Fabrication of a Microfluidic System for Capillary Electrophoresis Using a Two-Stage Embossing Technique and Solvent Welding on Poly(methyl methacrylate) with Water as a Sacrificial Layer,” *Anal. Chem.*, vol. 80, no. 7, pp. 2311–2318, Apr. 2008.
- [32] K. Mullis, F. Faloona, S. Scharf, R. Saiki, G. Horn, and H. Erlich, “Specific enzymatic amplification of DNA in vitro: The polymerase chain reaction,” *Cold Spring Harb. Symp. Quant. Biol.*, vol. 51, no. 1, pp. 263–273, Jan. 1986.
- [33] M. S. Rajeevan, D. G. Ranamukhaarachchi, S. D. Vernon, and E. R. Unger, “Use of real-time quantitative PCR to validate the results of cDNA array and differential display PCR technologies,” *Methods*, vol. 25, no. 4, pp. 443–51, Dec. 2001.
- [34] K. J. Livak and T. D. Schmittgen, “Analysis of relative gene expression data using real-time quantitative PCR and the 2(-Delta Delta C(T)) Method,” *Methods*, vol. 25, no. 4, pp. 402–8, Dec. 2001.
- [35] W. Koch, W. Latz, and M. Eichinger, “Genotyping of the common haptoglobin Hp 1/2 polymorphism based on PCR,” *Clin. ...*, vol. 1382, pp. 1377–1382, 2002.
- [36] L. Hamann, A. Hamprecht, A. Gomma, and R. R. Schumann, “Rapid and

- inexpensive real-time PCR for genotyping functional polymorphisms within the Toll-like receptor -2, -4, and -9 genes,” *J. Immunol. Methods*, vol. 285, no. 2, pp. 281–91, Feb. 2004.
- [37] S. J. Clark, A. Statham, C. Stirzaker, P. L. Molloy, and M. Frommer, “DNA methylation: bisulphite modification and analysis,” *Nat. Protoc.*, vol. 1, no. 5, pp. 2353–64, Jan. 2006.
- [38] A. Alonso, P. Martín, C. Albarrán, P. García, O. García, L. F. de Simón, J. García-Hirschfeld, M. Sancho, C. de La Rúa, and J. Fernández-Piqueras, “Real-time PCR designs to estimate nuclear and mitochondrial DNA copy number in forensic and ancient DNA studies,” *Forensic Sci. Int.*, vol. 139, no. 2–3, pp. 141–9, Jan. 2004.
- [39] H. Andréasson, M. Nilsson, B. Budowle, H. Lundberg, and M. Allen, “Nuclear and mitochondrial DNA quantification of various forensic materials,” *Forensic Sci. Int.*, vol. 164, no. 1, pp. 56–64, Dec. 2006.
- [40] I. M. Mackay, “Real-time PCR in the microbiology laboratory,” *Clin. Microbiol. Infect.*, vol. 10, no. 3, pp. 190–212, Mar. 2004.
- [41] M. Espy and J. Uhl, “Real-time PCR in clinical microbiology: applications for routine laboratory testing,” *Clin. Microbiol. ...*, vol. 19, no. 1, pp. 165–256, 2006.
- [42] C. Zhang, J. Xu, W. Ma, and W. Zheng, “PCR microfluidic devices for DNA amplification,” *Biotechnol. Adv.*, vol. 24, no. 3, pp. 243–284, 2006.
- [43] S. Yang, P. Ramachandran, R. Rothman, Y.-H. Hsieh, A. Hardick, H. Won, A. Kecojevic, J. Jackman, and C. Gaydos, “Rapid identification of

- biothreat and other clinically relevant bacterial species by use of universal PCR coupled with high-resolution melting analysis,” *J. Clin. Microbiol.*, vol. 47, no. 7, pp. 2252–5, Jul. 2009.
- [44] M. Maurin, “Real-time PCR as a diagnostic tool for bacterial diseases,” *Expert Rev. Mol. Diagn.*, vol. 12, no. 7, pp. 731–754, Sep. 2012.
- [45] K. Nagamine, T. Hase, and T. Notomi, “Accelerated reaction by loop-mediated isothermal amplification using loop primers,” *Mol. Cell. Probes*, vol. 16, no. 3, pp. 223–229, 2002.
- [46] K. A. Curtis, D. L. Rudolph, and S. M. Owen, “Rapid detection of HIV-1 by reverse-transcription, loop-mediated isothermal amplification (RT-LAMP),” *J. Virol. Methods*, vol. 151, no. 2, pp. 264–270, 2008.
- [47] X. Fang, Y. Liu, J. Kong, and X. Jiang, “Loop-mediated isothermal amplification integrated on microfluidic chips for point-of-care quantitative detection of pathogens,” *Anal. Chem.*, vol. 82, no. 7, pp. 3002–3006, 2010.
- [48] S. Y. Lee, C. N. Lee, H. Mark, D. R. Meldrum, and C. W. Lin, “Efficient, specific, compact hepatitis B diagnostic device: Optical detection of the hepatitis B virus by isothermal amplification,” *Sensors Actuators, B Chem.*, vol. 127, no. 2, pp. 598–605, 2007.
- [49] K. Ohtsuka, K. Ohtsuka, K. Yanagawa, K. Yanagawa, K. Takatori, K. Takatori, Y. Hara-kudo, and Y. Hara-kudo, “Detection of *Salmonella enterica* in Naturally Contaminated Liquid Eggs by Loop-Mediated Isothermal Amplification, and Characterization of *Salmonella* Isolates,” *Appl. Environ. Microbiol.*, vol. 71, no. 11, pp. 6730–6735, 2005.

- [50] M. Safavieh, M. U. Ahmed, M. Tolba, and M. Zourob, "Microfluidic electrochemical assay for rapid detection and quantification of *Escherichia coli*," *Biosens. Bioelectron.*, vol. 31, no. 1, pp. 523–528, 2012.
- [51] N. Tomita, Y. Mori, H. Kanda, and T. Notomi, "Loop-mediated isothermal amplification (LAMP) of gene sequences and simple visual detection of products," *Nat. Protoc.*, vol. 3, no. 5, pp. 877–882, 2008.
- [52] M. B. Kermekchiev, L. I. Kirilova, E. E. Vail, and W. M. Barnes, "Mutants of Taq DNA polymerase resistant to PCR inhibitors allow DNA amplification from whole blood and crude soil samples," *Nucleic Acids Res.*, vol. 37, no. 5, pp. 1–14, 2009.
- [53] X. Wang, D. J. Seo, M. H. Lee, and C. Choi, "Comparison of conventional PCR, multiplex PCR, and loop-mediated isothermal amplification assays for rapid detection of *Arcobacter* species," *J. Clin. Microbiol.*, vol. 52, no. 2, pp. 557–563, 2014.
- [54] P. Poltronieri, B. Sun, and M. Mallardo, "RNA Viruses: RNA Roles in Pathogenesis, Coreplication and Viral Load.," *Curr. Genomics*, vol. 16, no. 5, pp. 327–35, 2015.
- [55] S. Yaron and K. R. Matthews, "A reverse transcriptase-polymerase chain reaction assay for detection of viable *Escherichia coli* O157:H7: investigation of specific target genes," *J. Appl. Microbiol.*, vol. 92, no. 4, pp. 633–640, 2002.
- [56] R. W. Peeling and D. Mabey, "Point-of-care tests for diagnosing infections in the developing world.," *Clin. Microbiol. Infect.*, vol. 16, no. 8, pp. 1062–

9, Aug. 2010.

- [57] J. S. Chamberlain, R. A. Gibbs, J. E. Rainer, P. N. Nguyen, and C. Thomas, "Deletion screening of the duchenne muscular dystrophy locus via multiplex DNA amplification," *Nucleic Acids Res.*, vol. 16, no. 23, pp. 11141–11156, 1988.
- [58] J. Perkel, "Overcoming the Challenges of Multiplex PCR," *Biocompare*, 2012. [Online]. Available: <http://www.biocompare.com/Editorial-Articles/117895-Multiplex-PCR/>. [Accessed: 06-May-2017].
- [59] C. Dierkes, B. Ehrenstein, S. Siebig, H.-J. Linde, U. Reischl, and B. Salzberger, "Clinical impact of a commercially available multiplex PCR system for rapid detection of pathogens in patients with presumed sepsis," *BMC Infect. Dis.*, vol. 9, p. 126, Aug. 2009.
- [60] P. a. Rachwal, H. L. Rose, V. Cox, R. a. Lukaszewski, A. L. Murch, and S. a. Weller, "The potential of TaqMan array cards for detection of multiple biological agents by real-time PCR," *PLoS One*, vol. 7, no. 4, 2012.
- [61] M. Koziel, R. Kiely, L. Blake, I. O'Callaghan, G. D. Corcoran, B. Lucey, and R. D. Sleator, "Improved Detection of Bacterial Pathogens in Patients Presenting with Gastroenteritis by Use of the EntericBio Real-Time Gastro Panel I Assay," *J. Clin. Microbiol.*, vol. 51, no. 8, pp. 2679–2685, Aug. 2013.
- [62] Y. Schaerli, R. Wootton, and T. Robinson, "Continuous-flow polymerase chain reaction of single-copy DNA in microfluidic microdroplets," *Anal. Chem.*, vol. 81, no. 1, pp. 302–306, 2008.

- [63] D. Pekin, Y. Skhiri, J.-C. Baret, D. Le Corre, L. Mazutis, C. Ben Salem, F. Millot, A. El Harrak, J. B. Hutchison, J. W. Larson, D. R. Link, P. Laurent-Puig, A. D. Griffiths, and V. Taly, “Quantitative and sensitive detection of rare mutations using droplet-based microfluidics,” *Lab Chip*, vol. 11, no. 13, pp. 2156–2166, 2011.
- [64] M. M. Kiss, L. Ortoleva-donnelly, N. R. Beer, J. Warner, C. G. Bailey, B. W. Colston, J. M. Rothberg, D. R. Link, H. Leamon, R. Technologies, and H. Ave, “High-Throughput Quantitative PCR in Picoliter Droplets,” *Anal. Chem.*, vol. 80, no. 23, pp. 8975–8981, 2009.
- [65] A. C. Hatch, J. S. Fisher, A. R. Tovar, A. T. Hsieh, R. Lin, S. L. Pentoney, D. L. Yang, and A. P. Lee, “1-Million droplet array with wide-field fluorescence imaging for digital PCR,” *Lab Chip*, vol. 11, no. 22, pp. 3838–3845, 2011.
- [66] H. Zec, T. D. Rane, and T.-H. Wang, “Microfluidic platform for on-demand generation of spatially indexed combinatorial droplets,” *Lab Chip*, vol. 12, no. 17, pp. 3055–62, Sep. 2012.
- [67] K. Hsieh, H. C. Zec, P. C. Ma, T. D. Rane, and T. H. Wang, “Enhancing throughput of combinatorial droplet devices via droplet bifurcation, parallelized droplet fusion, and parallelized detection,” *Micromachines*, vol. 6, no. 10, pp. 1490–1504, 2015.
- [68] J. Chen, G. Zhou, Y. Liu, T. Ye, X. Xiang, X. Ji, and Z. He, “Assembly-line manipulation of droplets in microfluidic platform for fluorescence encoding and simultaneous multiplexed DNA detection,” *Talanta*, vol. 134,

pp. 271–277, 2015.

- [69] E. Ueda, F. L. Geyer, V. Nedashkivska, and P. A. Levkin, “DropletMicroarray: facile formation of arrays of microdroplets and hydrogel micropads for cell screening applications,” *Lab Chip*, vol. 12, no. 24, pp. 5218–5224, 2012.
- [70] W. Feng, L. Li, X. Du, A. Welle, and P. A. Levkin, “Single-Step Fabrication of High-Density Microdroplet Arrays of Low-Surface-Tension Liquids,” *Adv. Mater.*, vol. 28, no. 16, pp. 3202–3208, 2016.
- [71] O. Strohmeier, N. Marquart, D. Mark, G. Roth, R. Zengerle, and F. von Stetten, “Real-time PCR based detection of a panel of food-borne pathogens on a centrifugal microfluidic ‘LabDisk’ with on-disk quality controls and standards for quantification,” *Anal. Methods*, vol. 6, no. 7, p. 2038, 2014.
- [72] Y. Xu, H. Yan, Y. Zhang, K. Jiang, Y. Lu, Y. Ren, H. Wang, S. Wang, and W. Xing, “A fully sealed plastic chip for multiplex PCR and its application in bacteria identification,” *Lab Chip*, vol. 15, pp. 2826–2834, 2015.
- [73] S. O. Sundberg, C. T. Wittwer, C. Gao, and B. K. Gale, “Spinning disk platform for microfluidic digital polymerase chain reaction,” *Anal. Chem.*, vol. 82, no. 4, pp. 1546–1550, 2010.
- [74] H. Kettler, K. White, and S. Hawkes, “Mapping the landscape of diagnostics for sexually transmitted infections,” *TDR Publ.*, 2004.
- [75] P. Neuzil, J. Pipper, and T. M. Hsieh, “Disposable real-time microPCR device: lab-on-a-chip at a low cost.,” *Mol. Biosyst.*, vol. 2, no. 6–7, pp.

292–298, 2006.

- [76] H. Becker, “It’s the economy...,” *Lab Chip*, vol. 9, no. 19, pp. 2759–2762, 2009.
- [77] C. W. Tsao, L. Hromada, J. Liu, P. Kumar, and D. L. DeVoe, “Low temperature bonding of PMMA and COC microfluidic substrates using UV/ozone surface treatment,” *Lab Chip*, vol. 7, no. 4, p. 499, 2007.
- [78] C. G. Koh, W. Tan, M. Zhao, A. J. Ricco, and Z. H. Fan, “Integrating Polymerase Chain Reaction, Valving, and Electrophoresis in a Plastic Device for Bacterial Detection,” *Anal. Chem.*, vol. 75, no. 17, pp. 4591–4598, Sep. 2003.
- [79] R. H. Liu, J. Yang, R. Lenigk, J. Bonanno, and P. Grodzinski, “Self-Contained, Fully Integrated Biochip for Sample Preparation, Polymerase Chain Reaction Amplification, and DNA Microarray Detection,” *Anal. Chem.*, vol. 76, no. 7, pp. 1824–1831, Apr. 2004.
- [80] Y. Liu, C. B. Rauch, R. L. Stevens, R. Lenigk, J. Yang, D. B. Rhine, and P. Grodzinski, “DNA Amplification and Hybridization Assays in Integrated Plastic Monolithic Devices,” *Anal. Chem.*, vol. 74, no. 13, pp. 3063–3070, Jul. 2002.
- [81] G. Jia, J. Siegrist, C. Deng, J. V Zoval, G. Stewart, R. Peytavi, A. Huletsky, M. G. Bergeron, and M. J. Madou, “A low-cost, disposable card for rapid polymerase chain reaction,” *Colloids Surf. B. Biointerfaces*, vol. 58, no. 1, pp. 52–60, Jul. 2007.
- [82] A. F. Sauer-Budge, P. Mirer, A. Chatterjee, C. M. Klapperich, D. Chargin,

- and A. Sharon, “Low cost and manufacturable complete microTAS for detecting bacteria,” *Lab Chip*, vol. 9, no. 19, pp. 2803–10, Oct. 2009.
- [83] H.-O. Song, J.-H. Kim, H.-S. Ryu, D.-H. Lee, S.-J. Kim, D.-J. Kim, I. B. Suh, D. Y. Choi, K.-H. In, S.-W. Kim, and H. Park, “Polymeric LabChip real-time PCR as a point-of-care-potential diagnostic tool for rapid detection of influenza A/H1N1 virus in human clinical specimens,” *PLoS One*, vol. 7, no. 12, p. e53325, Jan. 2012.
- [84] R. Muddu, Y. a Hassan, and V. M. Ugaz, “Rapid PCR thermocycling using microscale thermal convection,” *J. Vis. Exp.*, no. 49, pp. 1–5, Jan. 2011.
- [85] J. H. Son, B. Cho, S. Hong, S. H. Lee, O. Hoxha, A. J. Haack, and L. P. Lee, “Ultrafast photonic PCR,” *Light Sci. Appl.*, vol. 4, no. 7, p. e280, 2015.
- [86] Q. Cao, M. Mahalanabis, J. Chang, B. Carey, C. Hsieh, A. Stanley, C. a Odell, P. Mitchell, J. Feldman, N. R. Pollock, and C. M. Klapperich, “Microfluidic chip for molecular amplification of influenza A RNA in human respiratory specimens,” *PLoS One*, vol. 7, no. 3, p. e33176, Jan. 2012.
- [87] E. K. Wheeler, C. a Hara, J. Frank, J. Deotte, S. B. Hall, W. Benett, C. Spadaccini, and N. R. Beer, “Under-three minute PCR: probing the limits of fast amplification,” *Analyst*, vol. 136, no. 18, pp. 3707–12, Sep. 2011.
- [88] Y. Zeng, R. Novak, and J. Shuga, “High-performance single cell genetic analysis using microfluidic emulsion generator arrays,” *Anal. ...*, vol. 82, no. 8, pp. 3183–3190, 2010.

- [89] K. A. Heyries, C. Tropini, M. VanInsberghe, C. Doolin, O. I. Petriv, A. Singhal, K. Leung, C. B. Hughesman, and C. L. Hansen, “Megapixel digital PCR,” *Nat. Methods*, vol. 8, no. 8, pp. 649–651, 2011.
- [90] D. Chen, M. Mauk, X. Qiu, C. Liu, J. Kim, S. Ramprasad, S. Ongagna, W. R. Abrams, D. Malamud, P. L. a M. Corstjens, and H. H. Bau, “An integrated, self-contained microfluidic cassette for isolation, amplification, and detection of nucleic acids,” *Biomed. Microdevices*, vol. 12, no. 4, pp. 705–19, Aug. 2010.
- [91] M. Focke, F. Stumpf, G. Roth, R. Zengerle, and F. von Stetten, “Centrifugal microfluidic system for primary amplification and secondary real-time PCR,” *Lab Chip*, vol. 10, no. 23, pp. 3210–2, Dec. 2010.
- [92] C. D. Ahrberg, B. R. Ilic, A. Manz, and P. Neuzil, “Handheld real-time PCR device,” *Lab Chip*, vol. 16, no. 3, pp. 586–592, 2016.
- [93] B. C. Giordano, J. Ferrance, S. Swedberg, a F. Hühmer, and J. P. Landers, “Polymerase chain reaction in polymeric microchips: DNA amplification in less than 240 seconds,” *Anal. Biochem.*, vol. 291, no. 1, pp. 124–32, Apr. 2001.
- [94] J. H. Jung, S. J. Choi, B. H. Park, Y. K. Choi, and T. S. Seo, “Ultrafast rotary PCR system for multiple influenza viral RNA detection,” *Lab Chip*, vol. 12, no. 9, pp. 1598–1600, May 2012.
- [95] G. M. Whitesides, “Cool, or simple and cheap? Why not both?,” *Lab Chip*, vol. 13, no. 1, pp. 11–3, Jan. 2013.
- [96] D. Mark, S. Haeberle, G. Roth, F. von Stetten, and R. Zengerle,

- “Microfluidic lab-on-a-chip platforms: requirements, characteristics and applications,” *Chem. Soc. Rev.*, vol. 39, no. 3, pp. 1153–82, Mar. 2010.
- [97] E. Lagally, P. Simpson, and R. Mathies, “Monolithic integrated microfluidic DNA amplification and capillary electrophoresis analysis system,” *Sensors Actuators B Chem.*, pp. 138–146, 2000.
- [98] P. Neuzil, C. Zhang, J. Pipper, S. Oh, and L. Zhuo, “Ultra fast miniaturized real-time PCR: 40 cycles in less than six minutes,” *Nucleic Acids Res.*, vol. 34, no. 11, p. e77, Jan. 2006.
- [99] Q. Zhu, Y. Gao, B. Yu, H. Ren, L. Qiu, S. Han, W. Jin, Q. Jin, and Y. Mu, “Self-priming compartmentalization digital LAMP for point-of-care,” *Lab Chip*, vol. 12, no. 22, pp. 4755–63, 2012.
- [100] A. Sposito, V. Hoang, and D. L. DeVoe, “Rapid real-time PCR and high resolution melt analysis in a self-filling thermoplastic chip,” *Lab Chip*, vol. 16, no. 18, pp. 3524–3531, 2016.
- [101] S. Park, Y. Zhang, S. Lin, T. Wang, and S. Yang, “Advances in microfluidic PCR for point-of-care infectious disease diagnostics,” *Biotechnol. Adv.*, vol. 29, no. 6, pp. 830–839, 2011.
- [102] Y. Zhang and P. Ozdemir, “Microfluidic DNA amplification—a review,” *Anal. Chim. Acta*, vol. 638, no. 2, pp. 115–25, Apr. 2009.
- [103] J. Wu, R. Kodzius, W. Cao, and W. Wen, “Extraction, amplification and detection of DNA in microfluidic chip-based assays,” *Microchim. Acta*, vol. 181, no. 13–14, pp. 1611–1631, Dec. 2014.
- [104] M. Bu, T. Melvin, and G. Ensell, “Design and theoretical evaluation of a

- novel microfluidic device to be used for PCR,” *J. Micromechanics Microengineering*, vol. 13, 2003.
- [105] T. Fukuba, T. Yamamoto, T. Naganuma, and T. Fujii, “Microfabricated flow-through device for DNA amplification—towards in situ gene analysis,” *Chem. Eng. J.*, vol. 101, no. 1–3, pp. 151–156, Aug. 2004.
- [106] C.-S. Liao, G.-B. Lee, J.-J. Wu, C.-C. Chang, T.-M. Hsieh, F.-C. Huang, and C.-H. Luo, “Micromachined polymerase chain reaction system for multiple DNA amplification of upper respiratory tract infectious diseases,” *Biosens. Bioelectron.*, vol. 20, no. 7, pp. 1341–8, Jan. 2005.
- [107] Z. Guttenberg, H. Muller, H. Habermüller, A. Geisbauer, J. Pipper, J. Felbel, M. Kielpinski, J. Scriba, and A. Wixforth, “Planar chip device for PCR and hybridization with surface acoustic wave pump,” *Lab Chip*, vol. 5, no. 3, pp. 308–17, Mar. 2005.
- [108] Z. Q. Niu, W. Y. Chen, S. Y. Shao, X. Y. Jia, and W. P. Zhang, “DNA amplification on a PDMS–glass hybrid microchip,” *J. Micromechanics Microengineering*, vol. 16, no. 2, pp. 425–433, Feb. 2006.
- [109] C. Liu, N. Toriello, and R. Mathies, “Multichannel PCR-CE microdevice for genetic analysis,” *Anal. Chem.*, vol. 78, no. 15, pp. 5474–5479, 2006.
- [110] C. Ke, A.-M. Kelleher, H. Berney, M. Sheehan, and A. Mathewson, “Single step cell lysis/PCR detection of *Escherichia coli* in an independently controllable silicon microreactor,” *Sensors Actuators B Chem.*, vol. 120, no. 2, pp. 538–544, Jan. 2007.
- [111] P. Man and C. Mastrangelo, “Microfabricated capillarity-driven stop valve

- and sample injector,” ... *Syst. 1998. MEMS ...*, pp. 45–50, 1998.
- [112] Y. Feng, Z. Zhou, X. Ye, and J. Xiong, “Passive valves based on hydrophobic microfluidics,” *Sensors Actuators A Phys.*, vol. 108, no. 1–3, pp. 138–143, Nov. 2003.
- [113] T. H. G. Thio, S. Soroori, F. Ibrahim, W. Al-Faqheri, N. Soin, L. Kulinsky, and M. Madou, “Theoretical development and critical analysis of burst frequency equations for passive valves on centrifugal microfluidic platforms,” *Med. Biol. Eng. Comput.*, vol. 51, no. 5, pp. 525–35, May 2013.
- [114] J. Y. Chou and B. C. Mansfield, “Mutations in the glucose-6-phosphatase-alpha (G6PC) gene that cause type Ia glycogen storage disease,” *Hum. Mutat.*, vol. 29, no. 7, pp. 921–30, Jul. 2008.
- [115] H. Cho, H.-Y. Kim, J. Y. Kang, and T. S. Kim, “How the capillary burst microvalve works,” *J. Colloid Interface Sci.*, vol. 306, no. 2, pp. 379–85, Feb. 2007.
- [116] M. Zimmermann, P. Hunziker, and E. Delamarche, “Valves for autonomous capillary systems,” *Microfluid. Nanofluidics*, vol. 5, no. 3, pp. 395–402, Jan. 2008.
- [117] O. Ymbern, E. Soria, V. Catalan, and J. Alonso, “Design and Fabrication of Centrifugal Microfluidic Platforms Based on Capillary Force Valves for Analytical Applications,” no. November, pp. 9–11, 2010.
- [118] C. T. Wittwer, “High-Resolution Genotyping by Amplicon Melting Analysis Using LCGreen,” *Clin. Chem.*, vol. 49, no. 6, pp. 853–860, Jun.

2003.

- [119] J. Melin and S. R. Quake, “Microfluidic large-scale integration: the evolution of design rules for biological automation.,” *Annu. Rev. Biophys. Biomol. Struct.*, vol. 36, pp. 213–231, 2007.
- [120] J. Liu, C. Hansen, and S. R. Quake, “Solving the ‘world-to-chip’ interface problem with a microfluidic matrix,” *Anal. Chem.*, vol. 75, no. 18, pp. 4718–4723, 2003.
- [121] R. R. Pompano, W. Liu, W. Du, and R. F. Ismagilov, “Microfluidics using spatially defined arrays of droplets in one, two, and three dimensions,” *Annu. Rev. Anal. Chem. (Palo Alto. Calif.)*, vol. 4, pp. 59–81, 2011.
- [122] H. Boukellal, S. Selimović, Y. Jia, G. Cristobal, and S. Fraden, “Simple, robust storage of drops and fluids in a microfluidic device.,” *Lab Chip*, vol. 9, no. 2, pp. 331–8, Jan. 2009.
- [123] A. Huebner, D. Bratton, G. Whyte, M. Yang, A. J. DeMello, C. Abell, and F. Hollfelder, “Static microdroplet arrays: a microfluidic device for droplet trapping, incubation and release for enzymatic and cell-based assays,” *Lab Chip*, vol. 9, no. 5, pp. 692–698, 2009.
- [124] S. S. Bithi and S. a Vanapalli, “Behavior of a train of droplets in a fluidic network with hydrodynamic traps,” *Biomicrofluidics*, vol. 4, no. 4, p. 44110, Jan. 2010.
- [125] C. N. Baroud, M. Robert de Saint Vincent, and J.-P. Delville, “An optical toolbox for total control of droplet microfluidics,” *Lab Chip*, vol. 7, no. 8, p. 1029, 2007.

- [126] M. Evander and J. Nilsson, "Acoustofluidics 20: applications in acoustic trapping.," *Lab Chip*, vol. 12, no. 22, pp. 4667–76, Nov. 2012.
- [127] R. Sista, Z. Hua, P. Thwar, A. Sudarsan, V. Srinivasan, A. Eckhardt, M. Pollack, and V. Pamula, "Development of a digital microfluidic platform for point of care testing," *Lab Chip*, vol. 8, no. 12, pp. 2091–104, 2008.
- [128] I. Barbulovic-Nad, H. Yang, P. S. Park, and A. R. Wheeler, "Digital microfluidics for cell-based assays," *Lab Chip*, vol. 8, no. 4, pp. 519–26, 2008.
- [129] S. K. Cho, H. Moon, and C. J. Kim, "Creating, transporting, cutting, and merging liquid droplets by electrowetting-based actuation for digital microfluidic circuits," *J. Microelectromechanical Syst.*, vol. 12, no. 1, pp. 70–80, 2003.
- [130] R. J. Jackman, D. C. Duffy, E. Ostuni, N. D. Willmore, and G. M. Whitesides, "Fabricating large arrays of microwells with arbitrary dimensions and filling them using discontinuous dewetting," *Anal. Chem.*, vol. 70, no. 11, pp. 2280–2287, 1998.
- [131] Y. Wang, C. E. Sims, and N. L. Allbritton, "Dissolution-guided wetting for microarray and microfluidic devices," *Lab Chip*, vol. 12, no. 17, pp. 3036–9, 2012.
- [132] Y. Wang, K. M. Southard, and Y. Zeng, "Digital PCR using micropatterned superporous absorbent array chips," *Analyst*, vol. 141, no. 12, pp. 3821–31, Jun. 2016.
- [133] A. Gansen, A. M. Herrick, I. K. Dimov, L. P. Lee, and D. T. Chiu, "Digital

- LAMP in a sample self-digitization (SD) chip,” *Lab Chip*, vol. 12, no. 12, pp. 2247–54, Jun. 2012.
- [134] T. Schneider, G. S. Yen, A. M. Thompson, D. R. Burnham, and D. T. Chiu, “Self-digitization of samples into a high-density microfluidic bottom-well array,” *Anal. Chem.*, vol. 85, no. 21, pp. 10417–10423, 2013.
- [135] A. K. White, K. A. Heyries, C. Doolin, M. VanInsberghe, and C. L. Hansen, “High-Throughput Microfluidic Single-Cell Digital Polymerase Chain Reaction,” *Anal. Chem.*, vol. 85, no. 15, pp. 7182–7190, 2013.
- [136] D. E. Cohen, T. Schneider, M. Wang, and D. T. Chiu, “Self-digitization of sample volumes,” *Anal. Chem.*, vol. 82, no. 13, pp. 5707–5717, 2010.
- [137] A. M. Thompson, A. Gansen, A. L. Paguirigan, J. E. Kreutz, J. P. Radich, and D. T. Chiu, “Self-Digitization Microfluidic Chip for Absolute Quantification of mRNA in Single Cells,” *Anal. Chem.*, vol. 86, p. 12308–12314, 2014.
- [138] Q. Tian, Y. Mu, Y. Xu, Q. Song, B. Yu, C. Ma, W. Jin, and Q. Jin, “An integrated microfluidic system for bovine DNA purification and digital PCR detection,” *Anal. Biochem.*, vol. 491, pp. 55–57, 2015.
- [139] A. M. Caliendo, D. N. Gilbert, C. C. Ginocchio, K. E. Hanson, L. May, T. C. Quinn, F. C. Tenover, D. Alland, A. J. Blaschke, R. A. Bonomo, K. C. Carroll, M. J. Ferraro, L. R. Hirschhorn, W. P. Joseph, T. Karchmer, A. T. MacIntyre, L. B. Reller, A. F. Jackson, and for the I. D. S. of A. (IDSA), “Better Tests, Better Care: Improved Diagnostics for Infectious Diseases,” *Clin. Infect. Dis. An Off. Publ. Infect. Dis. Soc. Am.*, vol. 57, no. Suppl 3,

pp. S139–S170, Dec. 2013.

- [140] F. Shen, W. Du, E. Davydova, A. Mikhail, J. Pandey, and R. Ismagilov, “Nanoliter multiplex PCR arrays on a SlipChip,” *Anal. Chem.*, vol. 82, no. 11, pp. 4606–4612, 2010.
- [141] G. Fridley, H. Le, E. Fu, and P. Yager, “Controlled release of dry reagents in porous media for tunable temporal and spatial distribution upon rehydration,” *Lab Chip*, vol. 12, no. 21, pp. 4321–7, Nov. 2012.
- [142] J. Kim, D. Byun, M. G. Mauk, and H. H. Bau, “A disposable, self-contained PCR chip,” *Lab Chip*, vol. 9, no. 4, pp. 606–612, 2009.
- [143] E. Carrilho, A. W. Martinez, and G. M. Whitesides, “Understanding Wax Printing: A Simple Micropatterning Process for Paper-Based Microfluidics,” *Anal. Chem.*, vol. 81, no. 16, pp. 7091–7095, Aug. 2009.
- [144] H. Wang, H. Chen, and M. Hupert, “Fully Integrated Thermoplastic Genosensor for the Highly Sensitive Detection and Identification of Multi-Drug-Resistant Tuberculosis,” *Angew. ...*, vol. 51, no. 18, pp. 4349–4353, 2012.
- [145] C. J. Easley, J. M. Karlinsey, J. M. Bienvenue, L. a Legendre, M. G. Roper, S. H. Feldman, M. a Hughes, E. L. Hewlett, T. J. Merkel, J. P. Ferrance, and J. P. Landers, “A fully integrated microfluidic genetic analysis system with sample-in-answer-out capability,” *Proc. Natl. Acad. Sci. U. S. A.*, vol. 103, no. 51, pp. 19272–7, Dec. 2006.
- [146] Z. Jobbagy, R. van Atta, K. M. Murphy, J. R. Eshleman, and C. D. Gocke, “Evaluation of the Cepheid GeneXpert BCR-ABL Assay,” *J. Mol. Diagn.*,

- vol. 9, no. 2, pp. 220–227, Apr. 2007.
- [147] E. L. Kendall, E. Wienhold, and D. L. DeVoe, “A chitosan coated monolith for nucleic acid capture in a thermoplastic microfluidic chip,” *Biomicrofluidics*, vol. 8, no. 4, p. 44109, Jul. 2014.
- [148] E. L. Kendall, E. Wienhold, O. D. Rahmanian, and D. L. DeVoe, “Ex situ integration of multifunctional porous polymer monoliths into thermoplastic microfluidic chips,” *Sensors Actuators B Chem.*, vol. 202, pp. 866–872, Oct. 2014.
- [149] T. Datta-Chaudhuri, P. Abshire, and E. Smela, “Packaging commercial CMOS chips for lab on a chip integration,” *Lab Chip*, vol. 14, no. 10, p. 1753, 2014.
- [150] R. Gurralla, Z. Lang, L. Shepherd, D. Davidson, E. Harrison, M. McClure, S. Kaye, C. Toumazou, and G. S. Cooke, “Novel pH sensing semiconductor for point-of-care detection of HIV-1 viremia,” *Sci. Rep.*, vol. 6, no. 1, p. 36000, 2016.